Aerocapture at Jupiter

A Feasibility Assessment

Edoardo Viero

Delft University of Technology

TU Delft

Aerocapture at Jupiter

A Feasibility Assessment

by

Edoardo Viero

to obtain the degree of Master of Science
at Delft University of Technology,
to be defended publicly on Friday September 22nd, 2023 at 10:00 AM.

Student number:	5615607	
Project duration:	September 8, 2022 – May 30, 2023	
Thesis committee:	Prof. R. Noomen,	TU Delft, supervisor
	Prof. E. Mooij,	TU Delft
	Prof. I. U. Balbin,	External (TU Delft)

Cover: Jupiter image taken by Juno (NASA)

TU Delft

Abstract

The current project investigated the feasibility of aerocapture at Jupiter, and the benefits in terms of payload mass fraction that could be achieved compared to traditional orbital insertion burns. A numerical simulation model has been set up, as well as an analytical formulation of the problem. The numerical verification of the analytical model showed that the analytical model still needs to be refined to produce accurate and useful results. Thermal fluxes, a driving aspect of aerocapture, have been implemented by using correlation laws, as well as corrective terms, all retrieved from literature. The aerocapture problem was numerically modeled and has been then optimized. However, the best trajectories provided a negative mass fraction benefit of -0.37 when compared to a traditional insertion burn. The best available mass fraction for the spacecraft's entry-unrelated subsystems was 0.44. Therefore, apart from some niche applications, aerocapture at Jupiter can be considered unappealing at best in the near future.

Contents

Nomenclature

Abbreviations

Abbreviation	Definition
AA	Aerodynamic reference frame, Airspeed based
B-frame	Body frame
CoM	Centre of Mass
ECEF	Earth-Centered Earth-Fixed
ECI	Earth-Centered Inertial
EFPA	Entry Flight-Path Angle
ESA	European Space Agency
ESS	Entry Support System
GNC	Guidance, Navigation, and Control
GTOP	Global Trajectory Optimisation Problem
GTOPX	Global Trajectory Optimisation Problem with eXtension
HEEET	Heatshield for Extreme Entry Environment Technology
I-frame	Inertial planetocentric reference frame
LVLH-frame	Local-Vertical Local-Horizontal frame
MHACO	Multi-objective Hypervolume-based Ant Colony Optimization
MJD	Modified Julian Day
NASA	National Aeronautics & Space Administration
ODE	Ordinary Differential Equation
PDS	Planetary Data System
R-frame	Rotating planetocentric reference frame
RKF	Runge-Kutta-Fehlberg
RSW-frame	Radial (R), along-track (S), cross-track (W) frame
SoI	Sphere of Influence
SPICE	NASA's data system. Its modules compose the acronym
SRP	Solar Radiation Pressure
TA-frame	Trajectory reference frame, Airspeed based
TCW	Theoretical Corridor Width
ToF	Time of Flight
TPS	Thermal Protection System
TUDAT	TU Delft Astrodynamics Toolbox
USM	Unified State Model
V-frame	Vertical frame (analogue to RSW-frame)
V&V	Verification & Validation

Symbols

Symbol	Definition	Unit
a	Semi-major axis	[m]
$\boldsymbol{a}$	Acceleration vector	[m/s^2]
B	Flyby impact parameter	[m]
c	Speed of light	[m/s]
C_D	Drag coefficient	[-]
C_L	Lift coefficient	[-]

Symbol	Definition	Unit
c_p	Specific heat capacity	[J/kg K]
D	Drag force	[N]
Δv	Delta-v	[m/s]
Δv_{OI}	Delta-v for orbital insertion at Jupiter	[m/s]
$\Delta \mathcal{E}_{\text{max}}$	Maximum delta orbital specific energy	[J/kg]
e	Eccentricity	[-]
f_{payload}	Payload mass fraction objective	[-]
f_{TPS}	TPS mass fraction	[-]
g_0	Standard acceleration of free fall	[m/s^2]
H_s	Scale height	[m]
i	Inclination	[°]
I_{sp}	Specific impulse	[s]
J_s	Solar constant at 1 AU	[W/m^2]
$J_2,\ J_3,\ J_4 \ldots$	Coefficients of the spherical harmonics expansion	[-]
Kn	Knudsen number	[-]
LD	Lift-to-drag ratio	[-]
$\dot{m}$	Mass injection rate	[kg/s]
p	Semi-latus rectum	[m]
q_C	Convective heat flux	[W/m^2]
$q_{C_{B=0}}$	Zero-ablation convective heat flux	[W/m^2]
q_R	Radiative heat flux	[W/m^2]
$q_{R_{\text{AD},\,B=0}}$	Zero-ablation radiative heat flux adiabatic wall	[W/m^2]
$q_{R_{B=0}}$	Zero-ablation radiative heat flux	[W/m^2]
q_w	Total wall heat flux	[W/m^2]
Q_w	Total heat load	[J/m^2]
R	Gas constant	[J/kg K]
Re	Reynolds number	[-]
R_N	Nose radius	[m]
t_{flyby}	Flyby epoch	[s]
T	Temperature	[K]
T_w	Wall temperature	[K]
$T_{w,ad}$	Adiabatic wall temperature	[K]
u	Argument of latitude	[°]
U	Gravitational potential	[m^2/s^2]
$\boldsymbol{v}$	Velocity vector	[m/s]
V_∞	Hyperbolic excess velocity	[m/s]
V_E	Entry velocity	[m/s]
α	Angle of attack	[°]
β	Angle of sideslip	[°]
Γ	Goulard Number	[-]
γ_g	Flight-path angle	[°]
γ_E	Entry fight-path angle	[°]
γ_F	Exit flight-path angle	[°]
δ	Latitude	[°]
ϵ_0	Permittivity of vacuum	[F/m]
θ	True anomaly	[°]
θ_{attitude}	Pitch angle	[°]
μ	Gravitational parameter	[m^3/s^2]
ρ	Density	[kg/m^3]
σ	Bank angle	[°]
τ	Longitude	[°]
ϕ	Roll angle	[°]
χ_g	Heading	[°]

Symbol	Definition	Unit
ψ	Yaw angle	[°]
ψ_{C_T}	Convective blockage factor	[-]
ω	Argument of pericentre	[°]
$\tilde{\omega}$	Longitude of pericentre	[°]
Ω	Longitude of the ascending node	[°]

1

Introduction

1.1. An Opening

Venturing into the furthest boundaries of the Solar System has been, and still is, a deed that often required many generations of passionate humans to be accomplished. Indeed, the clock of solar system traveling ticks way too slowly for a mission to be conceived, tested, manufactured, assembled, and flown in a human lifetime. And when the contingencies of the journey make it possible, the time we need to understand all the new discoveries a probe just made, that time asks the help of fresh, new minds. That time needs new humans ready to stand on the shoulders of the giants that preceded them, to take on their legacy, and hear what that probe had told us since the beginning.

Now, with the help of new technologies, that gap can be merged. Now, that Solar System clock can be hijacked to tick faster.

But, how?

By using what has always been there: the atmospheres of planets.

It has by now become common knowledge that, in order for a mission to arrive quicker, it has to travel faster. On this, scientific consensus has been reached long ago. Once arrived at the destination, however, that consensus quickly fades away. Until recently, there has not been an effective solution to slow the spacecraft down, to make it stay at its intended destination, and not escape and fly away, and be lost in the deepest parts of space. Now, a promising technique has been found and tried already: *aerocapture*. A simple, yet tricky, concept that promises powerful maneuvers, at the cost of equally powerful thermal and aerodynamic loads generated by those same operations.

The costs that aerocapture asks are the reason that motivated this project. A mission that wants to make use of its powerful benefits must also be able to sustain the harsh price of a severe atmospheric entry environment, one that would rip the probe apart if not for the countermeasures that are to be taken. A shield to protect the spacecraft from the heat, and a structure capable of sustaining the accelerations of an atmospheric entry, are the bare minimum a probe needs to exit that environment unharmed.

What needs to be addressed is whether those costs motivate the power that aerocapture can give, or not. This is clearly not a black-and-white picture. This is a picture with a multitude of shades, but some patterns to navigate this picture exist. There are planets for which those costs can be blindly paid. Mighty is the power that can be gained here. It is the case for Saturn, Uranus, and Neptune. For those planets, new mission concepts and faster travel times can finally be conceived, all thanks to the power of atmospheres. Missions developed with traditional techniques would not be even conceivable. Inner planets, such as Mars or Venus, do not promise the same gains outer planets guarantee. However, the costs they ask for are so little they can be easily paid, given a proper mission design is carried out.

There is one planet, however, one planet, that evades this logic. That one planet whose gravitational well is so powerful that the price for the power of aerocapture can rapidly become unaffordable. A spacecraft entering its atmosphere would do so with such high velocities that the thermal fluxes would quickly become unbearable. That planet is Jupiter, second to none, but the Sun, in the entire solar

system. Jupiter sits exactly on that thin grey line that discerns patterns where the power of aerocapture is convenient to those where it is simply too expensive.

The current project wants to investigate that grey line. This project aims at assessing the true costs of aerocapture at Jupiter. Whether or not the power of atmospheric braking can be worth the costs is the burning question this project starts with.

1.2. Research Question

This thesis project aims at answering what is the magnitude of the true costs, and the available options, of performing aerocapture at Jupiter. The research questions it starts with, are the following:

How can a Jupiter insertion trajectory be performed with the sole use of gravity assists and atmospheric drag?
How, if so, can an unpropelled trajectory to Jupiter deliver more payload than a traditional trajectory featuring impulsive insertion maneuvers?

These questions open the discussion, and the project itself. How this research will be carried out is explained in the following section.

1.3. Structure

Part I of the project comprehends all the background information, mainly retrieved from the literature study. It comprehends:

- Chapter 2, which introduces the techniques that will be investigated in the project;
- Chapter 3, which describes the main features of the Jupiter environment;
- Chapter 4, which presents the past missions that flew at Jupiter;
- Chapter 5, which talks about the dynamics relevant to the project.

Part II incorporates all the tools and the material needed for the project:

- Chapter 6, which describes the available tools;
- Chapter 7, which talks about the numerical methods in use;
- Chapter 8, which presents the available verification and validation material.

Part III combines the definition of the problem and its mathematical modeling:

- Chapter 9, which focuses on the definition of the problem, its boundaries, and its features;
- Chapter 10, which investigates the thermal environment at Jupiter and derives ways to calculate the thermal loads;
- Chapter 11, which addresses the problem of flybys, whether to incorporate them or not;
- Chapter 12, which is on the modeling of the problem in a mathematical sense;
- Chapter 13, which shows the tuning process for the integration scheme and the environment model;
- Chapter 14, which carries out the verification and validation of the model by using the available material.

Part IV is the main core of the project: it is the actual research performed, and it comprehends:

- Chapter 15, the optimization chapter, where the most promising trajectories are drawn and analyzed;
- Chapter 16, which eventually analyzes the pros and cons of the aerocapture technique.

Part V:

- Chapter 17, the conclusions and recommendations chapter.

Then, a list of references used in the project is present, followed by appendices:

- Appendix A, which contains some additional figures the project refers to;
- Appendix B, which contains tabulated data the project uses in some of its parts;
- Appendix C, which shows the time planning of the thesis.

Part I

Background

2

On the Use of Natural Forces

In designing a space mission, it is attractive to benefit from forces offered by nature. In this chapter, the gravity assist and the aerocapture maneuvers will be presented.

2.1. Natural Perturbations

Natural perturbations comprehend all the natural forces that can divert a spacecraft from its trajectory calculated with the 2-body model.

Clearly, natural perturbations have benefits that can be harnessed to perform unpropelled maneuvers, thus potentially increasing the payload mass of a spacecraft. Such benefits can be used by including these forces in the design of the trajectory.

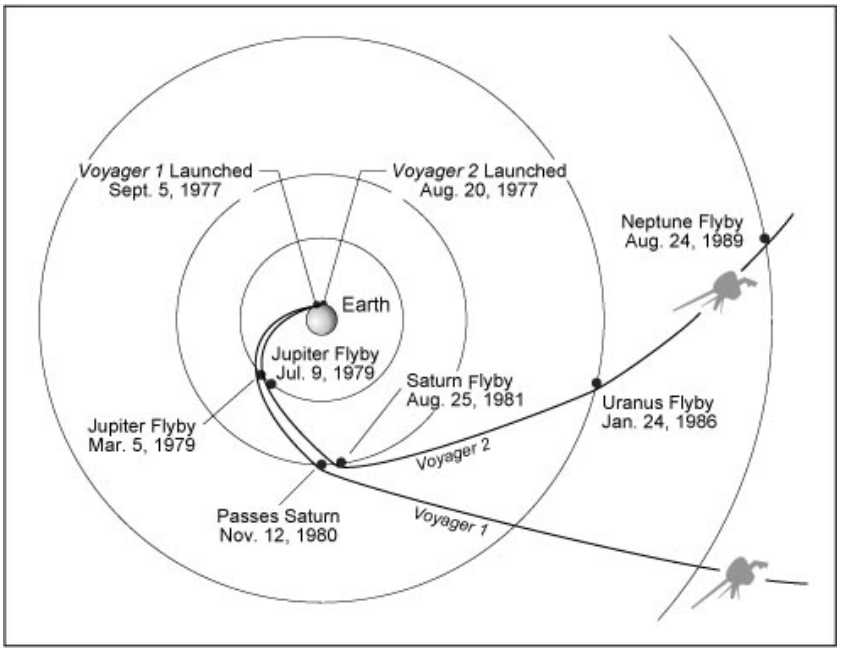

Figure 2.1: Trajectories of the two probes Voyager 1 and 2. They both performed multiple gravity assists to leave the Solar System with relatively low use of propellant. [1, Figure 1]

The impact of said natural perturbations has extensively been studied in the field of astrodynamics. One of the main benefits of this research is the decrease of the required propellant mass or Time of Flight (ToF) to follow space transfer trajectories. Many breakthrough discoveries enabled deep-space trajectories that would have been unfeasible otherwise (e.g. Figure 2.1). Many techniques that harness these perturbations have been developed but there is still room for many improvements and new discoveries.

The literature review that preceded this thesis started with a general aim: finding new ways to use natural orbital perturbations or improve existing techniques for space transfer trajectory design.

From this large scope, the research narrowed down to a more specific problem focused on the aerocapture and gravity assist techniques. As a science case, a multi-gravity-assist approach and aerocapture trajectory at Jupiter has been selected.

2.2. Gravity Assist

Gravity assists have been extensively used throughout the years of the space age to achieve goals otherwise impossible to reach. From missions outside the Solar System to missions directed towards the outermost or innermost planets orbiting the Sun, this technique has proven to be effective in reducing the amount of propellant to be carried on board, lowering the costs of several missions and enabling new perspectives.

Working principle

To explain the principle behind the gravity assist, the patched-conics approximation can be used to make it more straightforward. The following description comes from Wakker [2, Chapter 18].

It is assumed that the spacecraft is subject to the force of only one body at a time, which is the Sun while in interplanetary space, and is the planet when inside its sphere of influence (SoI). Within the planet SoI, the hyperbolic trajectory of the spacecraft is described relative to a planetocentric non-rotating reference frame, thus coordinate and velocity transformations are applied when passing from the heliocentric frame to a planetocentric one.

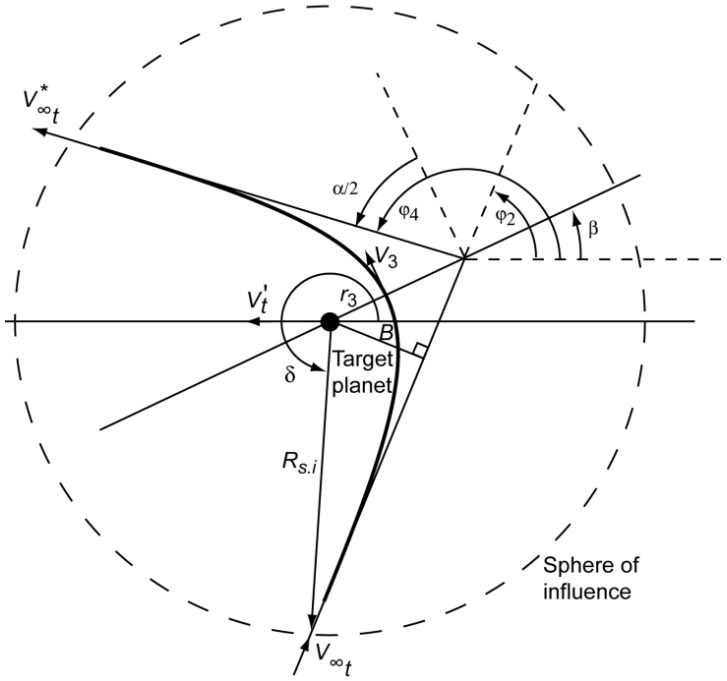

Figure 2.2: The in-plane geometry of hyperbolic encounter trajectories, which result in a gravity assist that changes the spacecraft velocity vector in the heliocentric frame [2, Figure 18.19].

Figure 2.2 shows the geometry of a hyperbolic flyby trajectory of the spacecraft relative to a planet. It can be seen that the direction of the arrival velocity $V_{\infty t}$ differs from that of the departure velocity $V^*_{\infty t}$. This results in a difference in heliocentric velocity before and after the flyby, all accomplished without any aid of impulsive maneuvers. It is not a transformation between kinetic and potential energy, since the latter remains almost unchanged. The spacecraft position in the heliocentric frame in fact barely changes during the entire flyby phase. It can then be concluded that ”passing close to a planet produces a discontinuous change in the total energy of the spacecraft’s heliocentric trajectory” [2]. This is, in essence, the *swingby effect*, as Wakker [2] calls it, also regarded as the *gravity assist*.

Such a technique is capable of greatly reducing the amount of propellant required for an interplanetary mission, thus increasing the amount of payload the probe can carry.

This approach works well in the simplified patched-conics approximation, which is useful for preliminary studies. For spacecraft applications, transfers from one planet to another are usually computed by using Lambert's theorem. This is done before running the actual simulations with an accurate physical model. Such transfers can be from Earth to the swingby planet or from the swingby planet to the target planet.

This approach can then be verified by Tisserand's criterion, which takes also three-body dynamics into account. Tisserand's criterion has been formulated by Tisserand and states that the Tisserand parameter, a value calculated from several Keplerian elements of an orbit, should remain constant between the orbits before and after a gravity assist.

The transfers to and from the swingby planet are then matched by using this criterion, which has to be satisfied in order to obtain viable launch and encounter opportunities [2].

Usage

This technique has been selected in this study for reducing the orbital energy of an approaching spacecraft at Jupiter so that the aerocapture phase could be less demanding in terms of aerothermal loads and potentially even more effective overall.

It has also been considered for a post-aerocapture flyby, which scope would be that of raising the orbital pericenter. In particular, both options would consider a gravity assist around one of the Galilean moons of Jupiter. More on this aspect in the next section.

2.3. Aero-capture

Aerocapture is a technique that consists of harnessing a planet's atmosphere to slow the spacecraft down and insert it into a closed orbit around the main body. It can be used alone, or combined with other techniques, such as gravity assists.

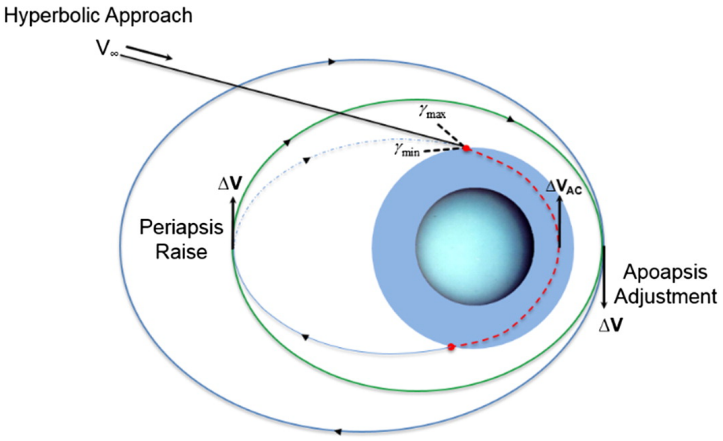

Figure 2.3: Aerocapture geometry with following pericenter raise and orbit adjustment maneuvers. [3, Figure 1]

This technique requires some critical post-aerocapture maneuvers to be conducted, such as the pericenter raise. A delta-v has to be applied to raise the pericenter above the capture planet's atmosphere; otherwise, the spacecraft would undergo a second atmospheric entry, with potentially catastrophic results for the mission.

3

Jupiter Environment

Jupiter offers a chaotic environment, where many objects play different roles and influence each other in many unpredictable ways. The scope of the current chapter is to present the natural forces at play in this environment, the characteristics of the atmosphere and radiation environments, and to highlight the major bodies orbiting Jupiter.

3.1. Natural Forces

Jupiter's environment is characterized by a variety of powerful and complex forces. The planet's strong magnetic field, which is one of the largest in the Solar System, interacts with the high-energy particles that are constantly bombarding the planet to create intense radiation belts. These radiation belts can be hazardous to spacecraft and even pose a threat to human exploration.

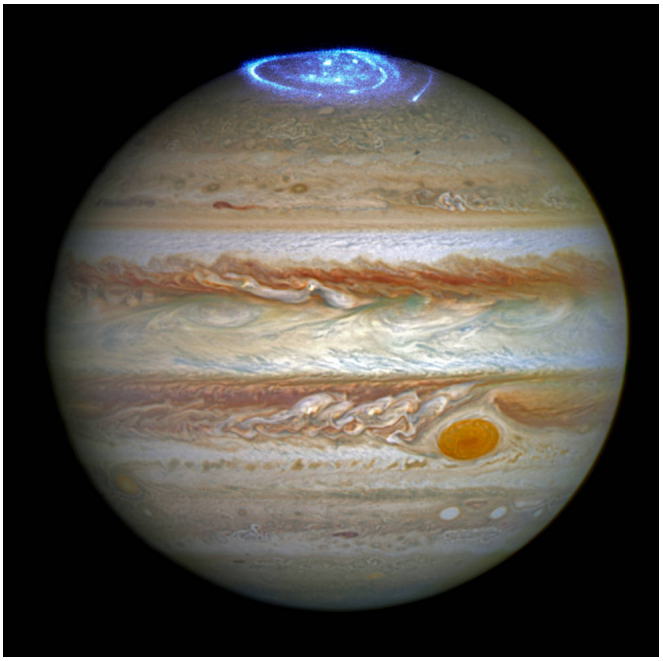

Figure 3.1: Auroras in Jupiter's atmosphere captured by Hubble Space Telescope [4].

In addition to the magnetic field, Jupiter's rotation also creates powerful atmospheric forces, driving the planet's distinctive cloud bands, storms, and jet streams. These atmospheric systems are further influenced by the planet's massive size and strong gravitational pull, which can affect the behavior of nearby moons and other objects in the vicinity. Finally, external forces, such as the gravitational influence of the Sun and other planets, can also shape Jupiter's environment, affecting its orbit and

even contributing to the formation and evolution of its moons and ring system. Understanding these complex and interrelated forces is crucial for studying Jupiter's environment and the role it plays in the larger Solar System.

3.2. Atmosphere

Jupiter, the largest planet in our Solar System, is a gas giant with a thick and complex atmosphere that has intrigued astronomers and space enthusiasts for centuries. Jupiter is more than 11 times the size of Earth and is mostly composed of hydrogen and helium. Its atmosphere is characterized by powerful winds, massive storms, and a range of atmospheric phenomena that make it one of the most complex and fascinating objects to study in our Solar System.

Jupiter's atmosphere is modeled using mainly data from the Galileo probe, which flew into Jupiter's atmosphere and collected various information about its characteristics. Three models are considered: interpolation of Galileo data, layered, and exponential models.

3.2.1. Interpolation

Interpolating data from the Galileo probe retrieves the most accurate density model for the atmosphere of Jupiter that can be achieved. Reconstructed in-flight data (Table B.1) from the Galileo descent contains density and pressure data related to altitude, thus a Lagrangian interpolation (explanation in Chapter 7) of this data returns highly accurate profiles for such quantities. Figure 3.2 shows the density profile with respect to altitude reconstructed by Seiff et al. [5]. From their data, the same profile could be retrieved and used for this study.

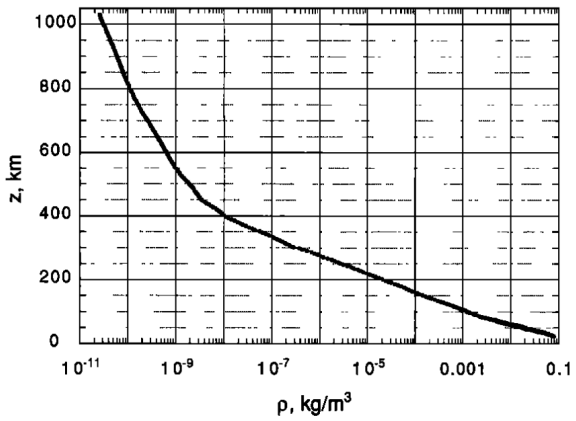

Figure 3.2: Density of the upper jovian atmosphere as a function of altitude, derived from measured probe decelerations. The steeper slope above 550 km indicates a major warming of the upper atmosphere [5, Figure 26].

3.2.2. Layered

A simpler approach to modeling the atmosphere of Jupiter is that of approximating it by dividing it into different layers per altitude, each of them with different properties. Each layer can have a constant temperature or a temperature linearly varying with altitude, as Figure 3.3 shows. For constant-temperature layers, the exponential model can be applied to them and is valid within the bounds of the layer. For linear-temperature-variation layers, the analytical model is more complex and can take into account the variation of the gravity force as well. This formulation has been taken from Mooij [6][1].

[1]The referred source, in its 2019 version, has a typo on this specific formula

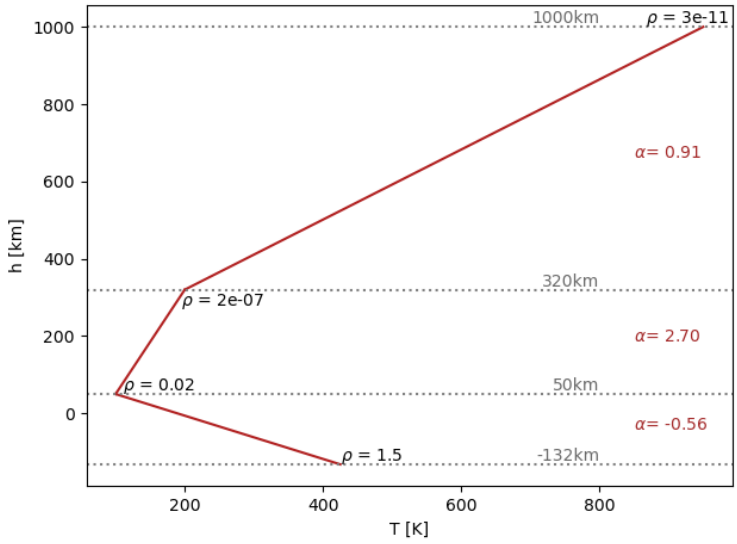

Figure 3.3: Jupiter atmosphere linearized temperature-altitude profile. Data has been taken from the descent of the Galileo probe, presented by Seiff et al. [5]. The temperature above 1000 km has been considered constant with the value it has at 1000 km. α represents the slope of the lines [km/K]. ρ is the density [kg/m^3].

By taking into account the varying temperature and the variation of the gravity force, and by assuming the atmosphere to be in hydrostatic equilibrium, the formulation for a linear-temperature-variation layer can be derived:

$$\frac{\rho}{\rho_0} = \left(\frac{h-h_0}{\alpha T_0}+1\right)^{-\frac{g_0\alpha}{R}(\alpha b T_0 - b h_0 + 1)} \cdot e^{\frac{g_0\alpha}{R} b (h-h_0)} \tag{3.1}$$

where T_0, h_0 are the temperature and altitude taken at the lower boundary of the layer; α is the temperature gradient of the layer; R is the gas constant for the Jupiter atmosphere (3614.92 J/ kg K [5]); *b* accounts for the variation of the gravity force with altitude ($b = \frac{2}{R_J}$).

3.2.3. Exponential

The exponential model describes the atmosphere of Jupiter by assuming a constant temperature at all altitudes and approximating the density profile with an exponential function. The formula for the density profile with altitude is

$$\frac{\rho}{\rho_0} = e^{-\left(\frac{h}{H_s}\right)} \tag{3.2}$$

where $\rho_0 = 0.16$ kg m^{-3} and $H_s = 27$ km [7].

3.3. Radiation environment

Jupiter is known for having a very intense radiation environment, due to its strong magnetic field and its position in the outer Solar System, where it is bombarded by high-energy particles from the Sun and other sources, such as Io's volcanic activity.

The magnetic field of Jupiter traps these particles in belts around the planet, creating a hazardous environment for spacecraft and potential human exploration. In fact, the radiation levels around Jupiter are so high that they can damage electronics and affect the performance of instruments on spacecraft. Understanding and mitigating the effects of this radiation is a major challenge for the success of a mission to Jupiter.

Figure 3.4 shows the equatorial profiles of radiation doses inside aluminum shells of different thicknesses. The radiation environment starts becoming severe when venturing closer than the orbit of Ganymede, and critically increases in severity when getting closer than Io's orbit. Then, closer than the orbit of Metis (the dot closest to Jupiter among the moons shown in the disposition of Figure 3.4), the radiation levels drop in intensity such that the profile of radiation dose does not pose a risk for the spacecraft anymore.

In conclusion, the equatorial radiation levels in Jupiter's environment are those of interest for the trajectory of an aerocapture mission. To achieve the lowest airspeed with respect to Jupiter's winds, a counter-clockwise equatorial trajectory is the optimal geometry.

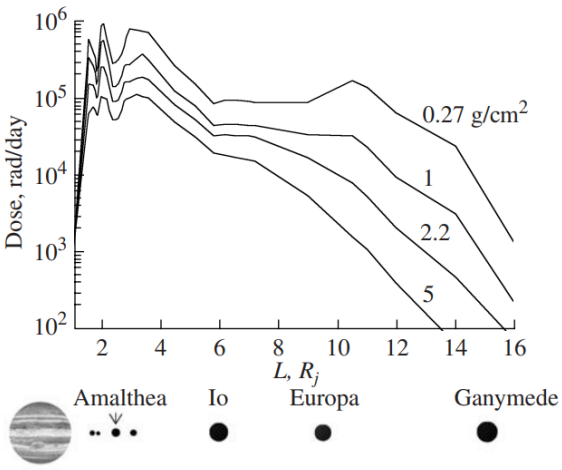

Figure 3.4: Equatorial profiles of radiation doses inside 0.27, 1, 2.2 and 5 g/cm^2 Al shells in Jupiter's environment. Below, the disposition of Jupiter's satellite is presented [8, Figure 2].

3.4. Galilean moons

The Galilean moons of Jupiter have always attracted great interest from researchers due to their dynamical complexity and the peculiar resonance pattern present between the inner three of them. The four Galilean moons are, from the closest to the furthest, Io, Europa, Ganymede, Callisto, and, as said before, the three moons in resonance are Io, Europa, and Ganymede, with a pattern 1:2:4 for their orbital periods.

Since these three moons present this peculiar pattern for their orbital periods, their configuration repeats itself after a set amount of time, that is after every four orbits of Io, the innermost of the three. Table 3.1 shows how this time span corresponds to approximately 7 days.

Table 3.1: Absolute orbital periods and relative values w.r.t. Io. [9]

Jupiter Moon	Orbital Period (days)	Orbital Period relative to Io
Io	1.769	1
Europa	3.551	2.0
Ganymede	7.155	4.0
Callisto	16.689	9.4

For what concerns all four moons, the time span after which the same configuration for all of them reoccurs is about 188 Io orbits, that is 332.572 days. The number of 188 orbits corresponds to the minimum common integer multiple between the relative orbital periods of the four moons (Table 3.1). It corresponds to 20 orbits of Callisto, 47 orbits of Ganymede, 94 orbits of Europa, and, as said, 188 orbits of Io. This result can be used when selecting the time span for the study to be conducted, see Chapter 15.

3.5. Rings

Jupiter is well-known for its system of rings, although they are not as prominent as those around Saturn. The rings of Jupiter were first discovered by the Voyager 1 spacecraft in 1979 and have since been studied in greater detail by subsequent missions. The rings are composed primarily of dust and small particles, with some larger rocks and boulders mixed in.

Jupiter's ring system is divided into four main components: the halo, main ring, Amalthea gossamer ring, and Thebe gossamer ring. The halo is a diffuse ring that surrounds the planet and is thought to be composed of small dust particles. The main ring is the most prominent and well-studied component,

consisting of four narrow bands of material. The Amalthea and Thebe gossamer rings are fainter and more diffuse, and are believed to be formed by dust ejected from the moons Amalthea and Thebe.

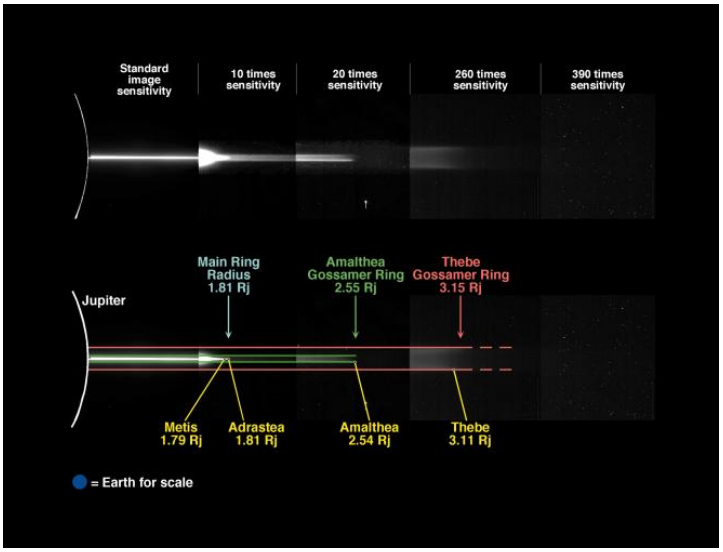

Figure 3.5: Rings of Jupiter [10]. The equatorial radius of Jupiter, R_j, is 71,398 km.

The rings of Jupiter extend in the vicinity of the planet, closer than Io's orbit. Figure 3.5 shows their structure. They are approximately comprised within Metis and Thebe orbits, thus they range from 92000 km to 226000 km in orbital radius from the center of Jupiter.

As said, such rings are mainly composed of dust, thus particles of diameters comprised between 0.1 and 10 μm [11]. There are no records of potential hazards posed by such rings, as the few large rocks and boulders are unlikely to collide with a spacecraft flying through those regions, thus it can be assumed that a mission to Jupiter should not consider Jupiter's rings as a primary risk for the mission.

A risk assessment is surely recommendable, however it goes beyond the scope of the current work.

4

Past Missions

This chapter summarizes the past missions of interest that had Jupiter as their destination. Such missions are the Galileo and the Juno mission.

4.1. Galileo

The Galileo mission has been devised to explore the Jupiter system in the 1990s. It consisted of an orbiter and a probe, the latter of which entered the atmosphere. When referring to the Galileo mission, the subject will just be the Galileo probe, unless explicitly stated otherwise. This is because the probe entry is the subject of interest in this study.

The work related to the Galileo mission includes the pre-flight studies performed prior to the entry, but much of the literature has sparked after the mission when many attempts to reconstruct its trajectory, the atmospheric properties, and the heat loads have been conducted.

In this section, the Galileo probe and its atmospheric descent will be presented. The reconstruction of thermal loads will be addressed in Chapter 10.

Probe characteristics

The Galileo Probe was a sphere-cone spacecraft with a 22.2 cm nose radius and 44.86 deg cone-half-angle, as Figure 4.1 shows [12]. The mass of the atmospheric probe was 338.93 kg for a diameter of 126.49 cm. Carbon phenolic and phenolic nylon were chosen for the ablative thermal protection system [13].

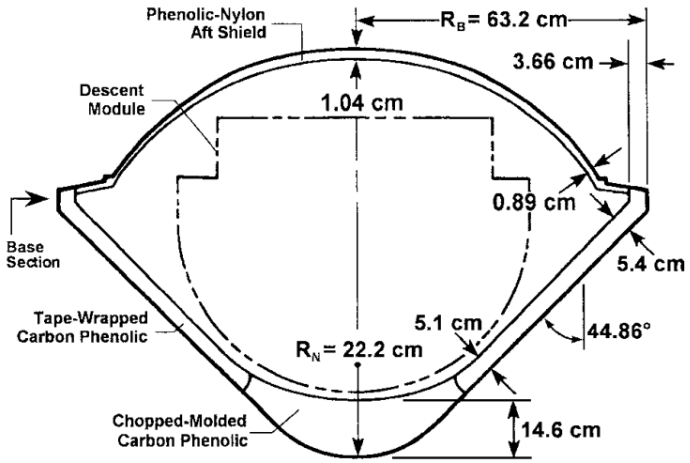

Figure 4.1: Cross-section of the Galileo probe deceleration module [14, Figure 1].

The entry conditions of the probe are set at an altitude of 450 km above the 1-bar-pressure level of Jupiter. They are presented in both inertial and body-fixed coordinates in Table 4.1.

Parameter	Inertial	Jupiter Body fixed
Entry velocity, km/s	59.92	47.4054
Entry angle, deg	- 6.64	- 8.4104
Entry latitude, deg	/	6.5303
Entry longitude, deg	/	4.9403
Entry heading, clockwise from east, deg	/	2.6111
Entry angle of attack, deg	0.0	5.7
He abundancy, mol %	/	13.6

Table 4.1: Galileo probe entry conditions [13, Table 3], [15]. Empty values are assumed to be equal to the other column counterpart.

Atmospheric entry

The Galileo probe followed a steep quasi-ballistic entry when entering Jupiter's atmosphere; a configuration that resulted in the highest aerothermodynamical loads a spacecraft can undergo during an atmospheric entry. Such trajectory differs substantially from that one of an aerocapture mission. However, the results of the Galileo mission can as well be applicable to a shallower entry, such as an aerocapture trajectory.

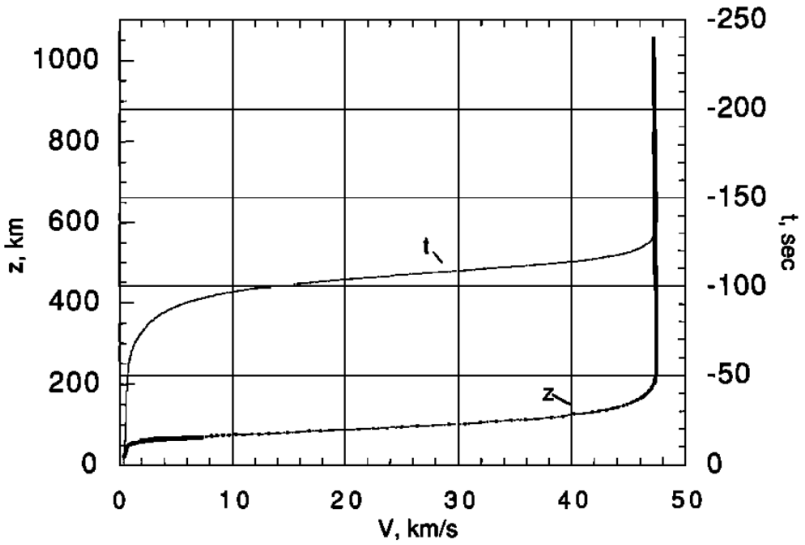

Figure 4.2: Probe velocity during entry as a function of time and altitude. Velocity started to decrease significantly at about -120 s (155 km), simultaneous with the onset of ablative mass loss [5, Figure 20].

The flight data of the Galileo probe entry, as well as data on Jupiter's atmosphere, is available thanks to Seiff et al. [13], which reconstructed the probe's trajectory and the atmospheric properties based on the probe's measurements. Values such as velocity, altitude, flight path angle, Mach number, drag coefficient, and Reynolds and Knudsen numbers for the probe descent are given at intervals of 5 seconds. The atmosphere properties are also tabulated. Atmospheric pressure and density, specific heat ratios, and temperature, among other values, are given with respect to the altitude.

Reynier, D'Ammando, and Bruno [12] collects the studies conducted to better model the chemical kinetics and convective heating thanks to the Galileo mission data. They also mention the thermal and mechanical loads experienced by the vehicle during re-entry. They state that: the peak heating rate and heat load exerted on the heatshield amounted to 300 MW/m^2 and 3000 MJ/m^2, respectively; the maximum deceleration was as large as 250 g. Moreover, the probe's 152 kg heat shield made up almost half of the probe's total mass and lost 80 kg during the entry. They also provide some flight data and physical characteristics of the Galileo probe.

4.2. Juno

The Juno mission was launched in 2011 to study Jupiter, and after a five-year journey, the spacecraft entered orbit around the planet on July 5, 2016, by means of a carefully planned orbital insertion burn. Juno's close flybys, passing within a few thousand kilometers of Jupiter's cloud tops, allowed its scientific instruments to make detailed measurements of the planet's gravitational and magnetic fields, as well as its atmospheric composition, temperature, and other important parameters [16]. Juno has completed over 30 orbits of Jupiter and has already provided researchers with a wealth of new data and insights into this fascinating planet, with many more exciting discoveries expected in the future.

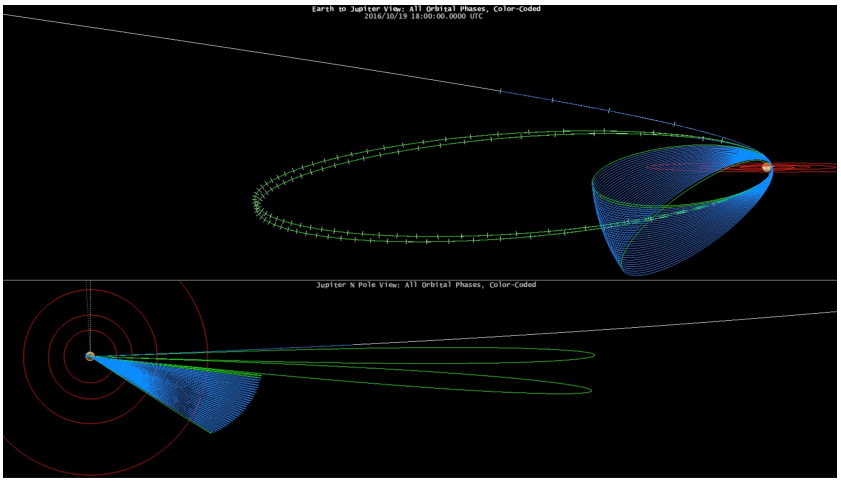

Figure 4.3: Nominal approach, bound orbit, and reduced period orbit of the Juno mission at Jupiter. The period-reduction maneuver was actually not performed in the real mission, resulting in the spacecraft remaining in the long-period orbits [17].

Flight data

Reconstruction of Juno navigation during the approach phase at Jupiter has been done by Bradley et al. [18].

Real orbital data about the Juno probe can be found at NASA SPICE Kernels [19]; data that can be used to verify the accuracy of the physical model, at least partially, by simulating the trajectory of Juno with the given model and comparing the trajectory with Juno orbital data.

5

Flight dynamics

The aim of the current chapter is to give an overview of the tools required for computing the flight dynamics of the problem, such as the reference frames and coordinate systems. The forces acting in the Jupiter environment are also compared.

5.1. Reference Frames

Choosing the appropriate reference frame(s) is essential to conduct a proper study, simplifying the process, and reducing the risk of introducing both logical and numerical errors. The following reference frames are taken from Mooij [6].

Inertial planetocentric reference frame (*I*-frame)

The origin of the inertial reference frame is located at the Centre of Mass (CoM) of the central body. The plane formed by the axes X_I and Y_I coincides with the equatorial plane of the central body. The Z_I-axis is pointing north and the reference meridian which determines the direction of the X_I-axis, is defined by the zero-longitude or prime meridian at zero time.

For Earth, in particular, the X_I-axis is fixed in inertial space at a specified time, and the reference frame is named after the chosen time. For example, J2000 is the name of the Earth inertial frame with X_I-axis pointing at the Vernal Equinox, a point in the constellation Aries, at 12h on 1 January 2000.

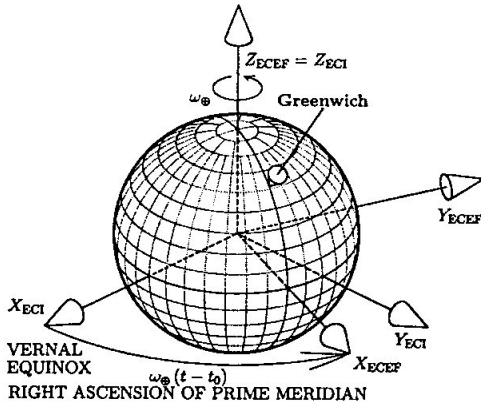

Figure 5.1: ECI and ECEF frames. ECI stands for Earth Centered Inertial, a planetocentric inertial frame, while ECEF stands for Earth-Centered Earth-Fixed frame, a planetocentric rotating frame. Their relationship is illustrated in the picture. For Earth, the prime meridian is represented by the Greenwich meridian. [20, Figure C.5]

Rotating planetocentric reference frame (*R*-frame)

This frame is fixed to the central body and coincides with the inertial planetocentric frame at the specified time (and once every full rotation of the central body after that). Again, the Z_R-axis is pointing north,

whereas the X_R-axis intersects the equator at zero degrees longitude and the Y_R-axis completes the right-handed system. The relation between this frame and the *I*-frame is shown in Figure 5.1.

Body reference frame (*B*-frame)
The body frame is fixed to the vehicle, with the origin set at its CoM. The X_B-axis lies in the longitudinal plane of symmetry and is positive in the forward direction. The Z_B-axis also lies in the plane of symmetry and is positive in the downward direction. The Y_B-axis completes the right-handed system.

Vertical reference frame (*V*-frame)
The Z_V-axis is pointing towards the CoM of the central body, along the radial component of the gravitational acceleration of a perfectly spherical body. The X_V-axis lies in a meridian plane, perpendicular to Z_V, and points to the northern hemisphere. The Y_V-axis completes the system. The $X_V\,Y_V$-plane is referred to as the local horizontal plane.

This frame is often regarded as the Local-Vertical Local-Horizontal (LVLH-frame), or as the Radial (R), along-track (S) and cross-track (W) frame (RSW-frame) (See Figure 5.2).

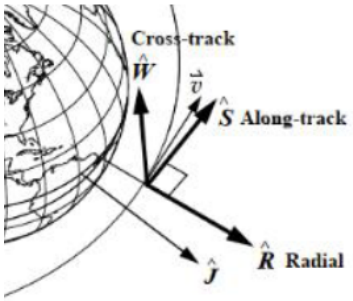

Figure 5.2: RSW reference system shown for an Earth-orbiting satellite: radial ($\hat{R}$), along-track ($\hat{S}$) and cross-track ($\hat{W}$) [21].

Trajectory reference frame, airspeed based (*TA*-frame)
The three axes of the *TG*-frame are defined as follows. The X_{TA}-axis is positive along the velocity vector relative to the atmosphere, the Z_{TA}-axis lies in the vertical plane, pointing downwards, and the Y_{TA}-axis completes right-handed system.

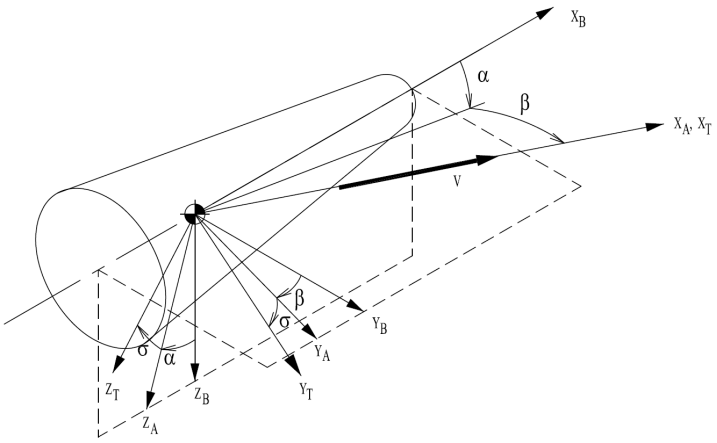

Figure 5.3: Definition of the aerodynamic attitude angles α, β and σ, positively oriented. It must be noted that σ is the bank angle. The three related reference frames are the body frame (index *B*), the aerodynamic frame (index *A*), and the trajectory frame (index *T*). [6, Figure 3-6]

Aerodynamic reference frame, airspeed based (*AA*-frame)
The X_{AA}-axis is defined along the velocity vector of the vehicle relative to the atmosphere, which implies that the X_{AA}-axis is collinear with the X_{TA}-axis. The Z_{AA}-axis is collinear with the aerodynamic lift

force (based on airspeed variables), but again opposite in direction. The Y_{AA}-axis completes the right-handed system. When the vehicle is not banking, the *AA*- and *TA*-frames are coincident. See Figure 5.3 for a visual depiction.

5.2. Coordinate systems

Choosing the appropriate coordinate system for a problem is a crucial matter; it permits to simplify the calculations and can reduce the magnitude of numerical errors. The following list of coordinate systems, except for the Modified Equinoctial Elements and the Unified State Model, is taken from Mooij [6].

Cartesian

Being the most common coordinates, cartesian elements allow the expression of the position, velocity and acceleration of the spacecraft with respect to either the *I*- or the *R*-frame.
Position and velocity are defined as:

Position: $x,\ y,\ z$
Velocity: $\dot{x},\ \dot{y},\ \dot{z}$ (labeled $u,\ v,\ w$ in the *R*-frame)

Spherical

Cartesian elements may at times result in complicated formulations for the Equations of Motion, which is why spherical components are used in these cases to simplify calculations. In spherical components, position and velocity (in the current context, we will only define them w.r.t. the *R*-frame) can be expressed by (Figure 5.4):

Position: distance R, longitude τ and latitude δ
Velocity: groundspeed V_g, flight-path angle γ_g and heading χ_g.

Longitude varies between $0° \leq \tau < 360°$, while latitude varies between $-90° \leq \delta \leq 90°$. γ_g varies between $-90° \leq \gamma_g \leq 90°$and χ_g varies between $-180° \leq \chi_g < 180°$.

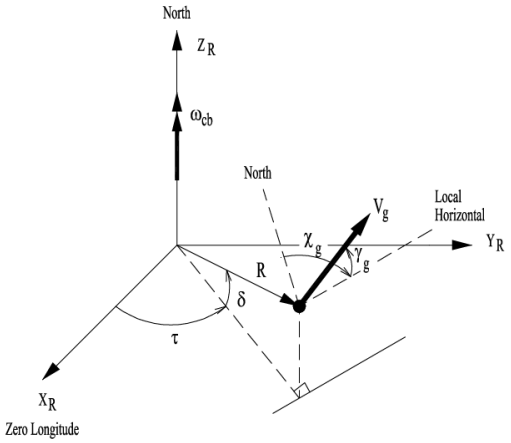

Figure 5.4: Definition in the *R*-frame of the six spherical flight parameters, the position ($R,\ \tau,\ \delta$) and velocity ($V_g,\ \gamma_g,\ \chi_g$). All angles are positively oriented. [6, Figure 3-4]

Keplerian

The six Keplerian elements defining the orbit shape and position of a spacecraft are:

a : semi-major axis ($a > R_p$[1])
e : eccentricity ($0 \leq e$)
i : inclination ($0° \leq i \leq 180°$)
ω : argument of pericentre ($0° \leq \omega < 360°$)
Ω : longitude of the ascending node ($0° \leq \Omega < 360°$)

[1] Radius of the central body

θ : true anomaly ($0° \leq \theta < 360°$)[2]
Their definition comes from Figure 5.5 for a, e, θ and Figure 5.6 for i, ω, Ω.

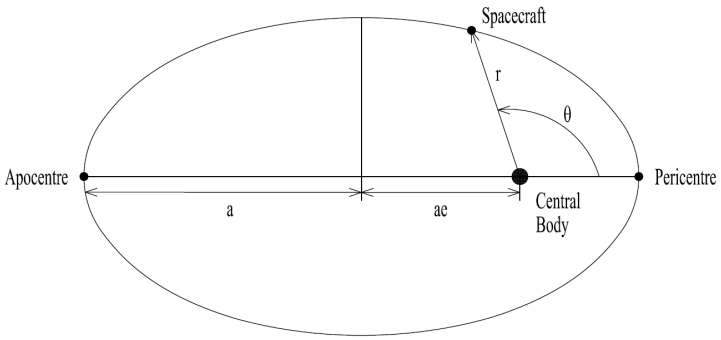

Figure 5.5: Definition of semi-major axis a and eccentricity e. The spacecraft is at a distance r from the main body, and the true anomaly is indicated by θ.[6, Figure 3-1]

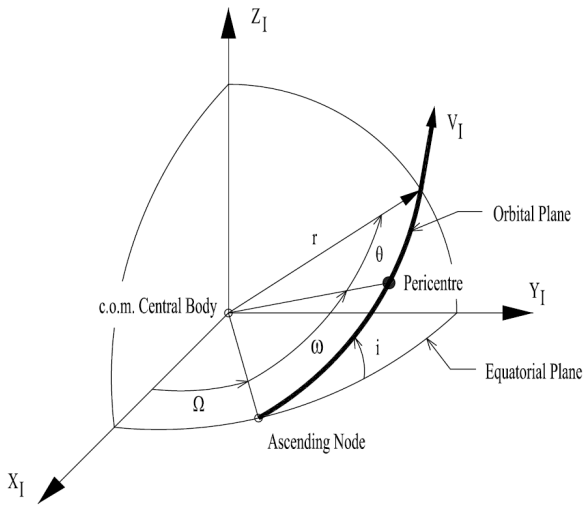

Figure 5.6: Definition of the three orbital parameters Ω, ω and i. The spacecraft is moving at a distance r with a velocity V_I w.r.t. the *I*-frame. [6, Figure 3-2] For low eccentricities, the *argument of latitude* $u = \omega + \theta$ is used instead of the two other separate variables, to avoid singularities. The same reasoning applies for low inclinations, where the longitude of pericentre $\tilde{\omega} = \Omega + \omega$ combines the two other separate variables [2].

Classical Attitude Angles

Classical attitude angles are the roll angle ϕ, the pitch angle θ_{attitude}, and the yaw angle ψ. For re-entry applications, these angles usually define the attitude of the body frame w.r.t. the inertial space, but it is also possible to have them define the attitude of the body w.r.t. the local horizontal plane.

Aerodynamic Angles

Aerodynamic angles, are the angle of attack α ($-180° \leq \alpha < 180°$, for a 'nose-up' attitude $\alpha > 0°$), the angle of sideslip β ($-90° \leq \beta \leq 90°$, β is positive for a 'nose-left' attitude) and the bank angle σ ($-180° \leq \sigma < 180°$, σ is positive when banking to the right). Their definition is shown in Figure 5.3.

Quaternions

Quaternions, or the four parameters of Euler, are $Q1$, $Q2$, $Q3$, and $Q4$. A quaternion is a four-dimensional hyper-complex number and consists of one real and three imaginary numbers. Since the quaternions form a set of four coordinates, every rotation happens to be over-determined, there are no singularities present for any rotation.

[2] In the original source [6] the mean anomaly (M), instead of the true anomaly (θ), had been regarded. For practical reasons, the latter has instead been preferred. θ allows for a more direct hence convenient representation of the spacecraft position in Keplerian coordinates.

Unified State Model

The Unified State Model (USM) is a method for expressing orbits using a set of seven elements, which consist of a quaternion and three parameters based on the velocity hodograph [22]. Such a coordinate system comes in different varieties, each of them comprising a different set of elements.

The traditional USM, or USM7, uses, as already said, the quaternions and the velocity hodograph. A variation of the USM7, the USM6, uses Modified Rodrigues Parameters (MRP) instead of a quaternion, and, finally, the USMEM is another variation that uses the exponential map instead of a quaternion.

The major benefit of this coordinate system is the total absence of singularities, as it has one more variable than the six degrees of freedom of a spacecraft.

For a more detailed description of how the parameter sets are derived, refer to Vittaldev, Mooij, and Naeije [22].

5.3. Natural Forces Assessment

The scope of the present paragraph is to give a first-order estimate of the acceleration magnitudes within this environment. The result of such a comparison is shown in Figure 5.7 and 5.8. Multiple assumptions have been made to give an estimation of such forces, thus it can only be used to have an order of magnitude ide on the importance of a force. The models for the forces are later presented.

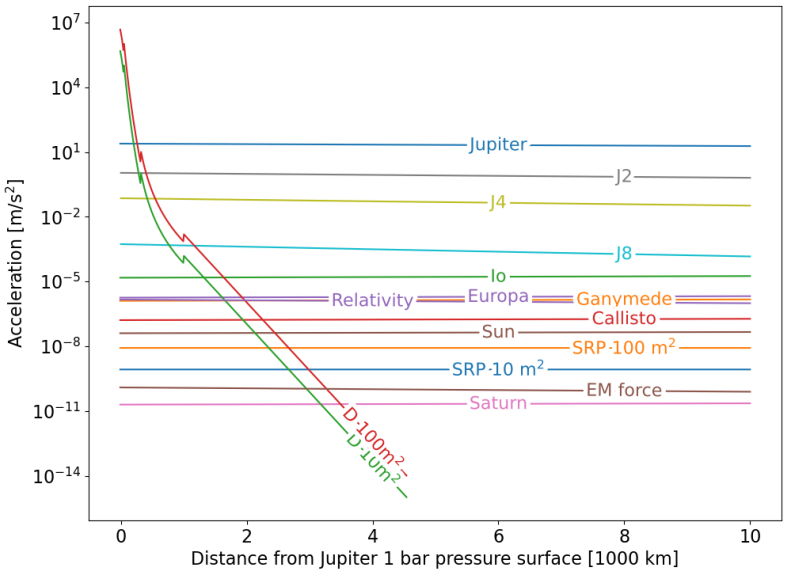

Figure 5.7: Order of magnitude of various accelerations acting on a body in the vicinity of Jupiter. *D* stands for Drag and *SRP* for Solar Radiation Pressure, and for them the spacecraft cross-sectional area used for computing these forces has also been noted. The influence of individual spherical-harmonics terms is of planet Jupiter.

By looking at Figure 5.7 it is immediately clear how the drag force has the capability of steering the spacecraft far more than any other force, provided that such spacecraft is flying at altitudes lower than 500 km. Other remarkable notes can be made about the importance of irregularities in the Jupiter gravity field.

Such irregularities must always be regarded, especially when the spacecraft is flying in the vicinity of Jupiter. Also, a comparison with other models for the gravity field has to be done, since the spherical-harmonics formulation can diverge when flying closer than the reference radius. It could lead to errors so big that a better accuracy can be reached by removing the entire spherical-harmonics formulation, or just some high-order terms, from the model.

Peculiar are the magnitudes of the Lorentz force (labeled as EM force) and the Relativistic terms, which are likely to be included in the model for reaching sufficient accuracy.

From Figure 5.8, other important insights can be obtained, such as the importance of the Galilean

moons. Their gravity appears to be powerful enough to make the gravity-assist maneuver a useful tool for changing the spacecraft orbit, before or after the aerocapture.

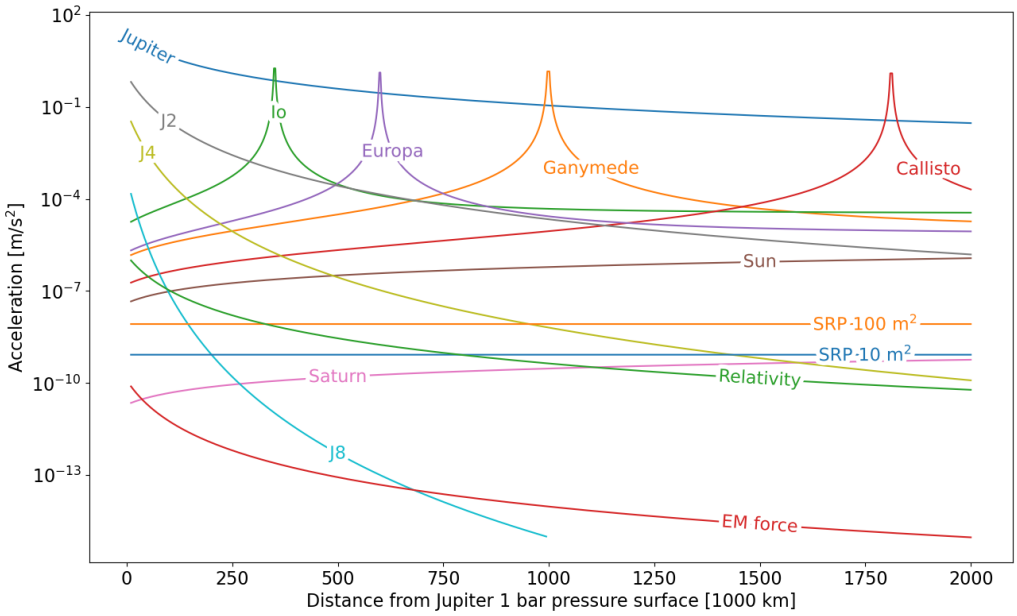

Figure 5.8: Order of magnitude of various accelerations acting on a body for high altitudes at Jupiter. SRP stands for Solar Radiation Pressure, and the spacecraft cross-sectional area used for computing it has also been noted. Individual spherical-harmonics terms are of the planet Jupiter.

Third-body Gravity

For the gravitational forces, the regarded body has been assumed to be at the closest distance possible to the spacecraft, so that its magnitude would have been assessed at the worst case.

The distances between celestial bodies have been taken from De Pater and Lissauer [9]. The gravitational parameters have been retrieved from the SPICE kernels provided by NASA [23].

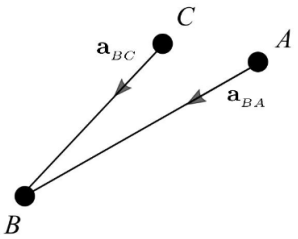

Figure 5.9: Scheme of the acceleration exerted by a third body. *A* is the spacecraft, *C* is Jupiter (the central body), and *B* is the third body exerting gravity.

For any body other than Jupiter, the gravity has been calculated by following the scheme presented in Figure 5.9, which translates into

$$(\boldsymbol{a}_{BA})_C = \boldsymbol{a}_{BA} - \boldsymbol{a}_{BC} \qquad (\boldsymbol{a}_{BA} = \nabla U_B(\boldsymbol{r}_{BA})) \tag{5.1}$$

For each of the four Galilean Moons, the gravity force has been computed up to their surface value, which corresponds to the peaks that can be seen in Figure 5.8. Any value of the force computed within the surface radius of the moons has been truncated at the surface acceleration magnitude.

Spherical-Harmonics Terms

The same reasoning applies for the spherical-harmonics terms evaluated, which have been taken at their highest magnitude possible, that is at Jupiter's poles [3], and that decrease in magnitude with increasing distance from Jupiter.

It must be noted though that such terms, despite being quite powerful, almost cancel each other out during each orbit. Usually, only a small fraction of such force remains unbalanced, and that is the fraction that continuously perturbs the orbit of the spacecraft.

The formulas have been derived from the spherical-harmonics expansion of the gravitational field (Equation 5.2), for $l = 2, 4, 8$ and $m = 0$, and all the required coefficients (normalized) have been retrieved from TUDAT [24]. It follows that the longitude θ does not play any role in these cases, and that the latitude ϕ that results in the highest magnitude is 90°.

B is the body exerting gravity (Jupiter) and *A* is the spacecraft.

$$\left(\frac{\delta U_B}{\delta r}\left(\boldsymbol{r}_A\right)\right)_{l,\,m} = -\left(l+1\right)\frac{\mu}{r^2}\left(\frac{R}{r}\right)^l \bar{P}_{lm}(\sin\phi)\left(\bar{C}_{lm}\cos m\theta + \bar{S}_{lm}\sin m\theta\right) \tag{5.2}$$

Solar Radiation Pressure

Solar Radiation Pressure is a small but potentially powerful force, which can result in rather high perturbations in a satellite orbit if not taken into consideration. This fact comes from the direction from which the force comes, that is radially expanding from the Sun. Especially for relatively small trajectories it can be considered to always point the same direction; a geometry that leads to great perturbations in a relatively small amount of time.

The force has been calculated with the following formula:

$$a_{SRP} = 2\frac{I}{c}\frac{A}{m} \qquad I = (J_s)_J = (J_s)_E\left(\frac{r_E}{r_J}\right)^2 \tag{5.3}$$

and as $(J_s)_E$, the solar constant calculated at distance of 1 AU, a value of 1360.8 W m^{-2} has been taken [25]. The spacecraft mass has been estimated to be 4000 kg (based on past missions to Jupiter); r_E and r_J are the distance of Earth and Jupiter from the Sun, again retrieved from De Pater and Lissauer [9]; *c* is the speed of light; the cross-section area *A* has been taken as 10 m^2 and as 100 m^2 to assess the effect of SRP on spacecrafts of different sizes.

Drag

Since the study is focused on aerocapture, it is natural to deduce that the drag force, and aerodynamic forces in general, will be the dominant ones, among all of them.

The peculiarity of drag of acting always in opposition with the direction of motion makes it a powerful tool for changing a spacecraft trajectory. It also comes with drawbacks, though, such as the heating that it induces on the spacecraft during the atmospheric entry. The heat flux and the total heat absorbed must be thoroughly modeled, otherwise an initially promising mission could result in a catastrophe due to excessive heating on the vehicle.

The formulation for the drag force is in principle very straightforward:

$$\boldsymbol{a}_D = -\frac{1}{2}\rho v^2 C_D \frac{A}{m}\hat{\boldsymbol{v}} \tag{5.4}$$

where ρ represents the atmospheric density; v the spacecraft velocity w.r.t. the atmosphere, which has been selected to be 59 km s^{-1} [26]; C_D is the drag coefficient, taken as 1.2 as a rough first estimate; *A* and *m*, the spacecraft area and mass, have been kept equal to those used for the Solar Radiation Pressure acceleration.

Since the drag acceleration varies according to ρ, and the atmospheric density of Jupiter varies with the altitude, the density profile of Jupiter's atmosphere is necessary to compute the drag. To obtain such a profile, a model that divides the atmosphere of Jupiter into layers, shown in Figure 3.3, has been adopted. The analytical model of the density variation has been presented in Chapter 3.

[3] The final mission geometry will actually feature an equatorial trajectory, however the results of this preliminary study have been kept as a rough first estimate.

Lorentz Force

It is common for spacecraft to get charged while in space. This can happen for several causes, ranging from interactions with the surrounding plasma environment to being exposed to the solar radiation. Such phenomena can leave the spacecraft positively or negatively charged, thus making it acquire a potential w.r.t. the environment.

If such spacecraft orbit planets equipped with a powerful magnetic field, they are then subjected to what is called the Lorentz force $\boldsymbol{F} = q\,\boldsymbol{v} \times \boldsymbol{B}$. From this basic formulation, well-known in physics, Wakker [2] derives the acceleration a satellite orbiting the primary body in a circular orbit experiences:

$$\boldsymbol{a}_L \approx -4\,\pi\,\epsilon_0\,g_{1,0}\,\frac{U^* R_s}{M}\left(\frac{R}{r}\right)^3\sqrt{\frac{\mu}{r}}\,\boldsymbol{e}_r \tag{5.5}$$

where ϵ_0 is the permittivity of vacuum ($8.8542 \cdot 10^{-12}$ F/m); $g_{1,0}$ is the first Gauss coefficient of the harmonic expansion for the magnetic field, which permits as a first-order approximation to consider such a field as a magnetic dipole, and for Jupiter is 4.242 G [27]; U^* is the electrical potential difference between the satellite and the surrounding plasma, estimated to be around -100 V for Jupiter [28]; R_s is the satellite radius; M is the mass of the satellite; R is the planet reference radius for the magnetic field spherical-harmonics expansion, which for Jupiter is 71,372 km [27]; μ is the gravitational parameter of the central body; r, finally, is the distance from the center of mass of the planet.

Apart from the assumptions already mentioned, such as the satellite placed in a circular orbit or the magnetic field approximated as a dipole, the satellite here has also been assumed to be a spherical conducting body, such that its capacitance is $C = -4\,\pi\,\epsilon_0\,R_s$.

For a more detailed formulation of the Lorentz force, refer to Wakker [2] (Chapter 20.5), and, for the coefficients of the Jupiter magnetic field, refer to Ness [27].

For what concerns the geometry of the acceleration, it acts in radial direction, as it can be seen in Equation 5.5. It can be inward or outward pointing depending on the charge of the spacecraft.

Relativistic effects

For high-accuracy applications, the effects of relativity must be regarded, since the Newtonian gravity formulation does not describe reality with sufficient precision.

Montenbruck, Gill, and Lutze [29] describe the relativistic effects presented below.

While regarding relativity, however, special relativity alone is not sufficient in the vicinity of a massive body. This happens because it assumes a flat four-dimensional space-time, but massive bodies with their mass and angular momentum lead to a curvature of the said four-dimensional space-time. General relativity must then be used, a formulation that lets the space-time to be warped by massive bodies. The *geodesic equation* describes the motion of a satellite in such space, and, if expanded to first order, while also dropping the gravito-magnetic contributions, it leads to the post-Newtonian correction of the acceleration:

$$\boldsymbol{a}_{rel} = -\frac{\mu}{r^2}\left(\left(4\frac{\mu}{c^2 r} - \frac{v^2}{c^2}\right)\boldsymbol{e}_r + 4\frac{v^2}{c^2}\left(\boldsymbol{e}_r \cdot \boldsymbol{e}_v\right)\boldsymbol{e}_v\right) \tag{5.6}$$

where $\boldsymbol{e}_r$ and $\boldsymbol{e}_v$ denote the unit position and velocity vectors; v is the circular velocity of the spacecraft; μ is the gravitational constant of the primary body; c is the speed of light. For the current first-order estimate, the orbit of the satellite has been considered circular, so that Equation 5.6 becomes:

$$\boldsymbol{a}_{rel} = -\frac{\mu}{r^2}\left(3\frac{v^2}{c^2}\right)\boldsymbol{e}_r \tag{5.7}$$

Here, also the relativistic terms act radially on the spacecraft.

5.4. Observations

As it could be seen Jupiter's surroundings is a very complicated environment with many different effects playing greater or smaller roles, depending on their intensity, or on the considered region.

It comes as consequence that a selection of the most important components of such environment, those to include in a simulation suite, has to be conducted once the mission trajectory and the problem are somewhat defined.

It is for this reason that such selection will be conducted in Chapter 13, where only the most important components will be selected.

Part II

Tools & Material

6

Hardware & Software

The current chapter presents the hardware and software tools that will be used throughout the study.

6.1. Hardware

As hardware tools for the project, a consumer-level laptop has been found sufficient. The required numerical tasks are well within the capabilities of current laptops, thus no need for additional hardware has been found.

This section aims at describing the hardware used for the project so that it would serve as a future reference when comparing the required time for running simulations to their complexity (number of function evaluations, model complexity, etc.).

CPU

The processor is an Intel Core i7 8750H, with a nominal clock speed of 2.20 GHz. As cache memory, it has 6 slots of 32 kB L1 D-Cache and also for the L1 I-Cache, 6 slots of 256 kB L2 Cache, and 9 MB of L3 Cache.

RAM memory

The laptop possesses one slot of 16 GB of DDR4 RAM memory, with a 1200 MHz clock speed.

Storage memory

As storage memory, data will be kept in a 500 GB SSD drive. It is estimated that the total volume of data will remain within the order of 10 GB.

6.2. Software

This section lists the software tools that will be used throughout the study.

6.2.1. Python

Python is a well-known and widely recognized coding language. It is often used in the field of research, and so will be for the current work. All the following libraries provide an interface to Python, and, together with its straightforwardness in usage, they make Python the best choice as the programming language for this project.

6.2.2. TUDAT

As stated in the software website: *"The TU Delft Astrodynamics Toolbox (Tudat) is a powerful set of libraries that support astrodynamics and space research. Such framework can be used for a wide variety of purposes, ranging from the study of reentry dynamics to interplanetary missions"*[30].

It is particularly suited for the current science case that will be studied and optimized.

Moreover, TUDAT allows for external contributions in the form of c++ or Python code, thus any new software that will need to be developed can be programmed using one of these two languages. It is

likely that Python will be preferred over c++, despite being less efficient, in order to keep the schedule constraints set for the thesis.

Available features
TUDAT is a software that can accurately simulate the Jupiter system and is capable of handling atmospheric entry portions of the trajectory as well. It also includes a wide set of integration and propagation schemes that are readily available. The USM7 and RKF7(8) propagation and integration schemes, which have been selected during the literature review and will be presented in Chapter 7, are already included.

Moreover, a JPL SPICE interface is also available, meaning that data from previously flown missions can easily be used in the software and no new tool has to be developed for that.

6.2.3. Pygmo
In addition to performing trajectory simulations, for which TUDAT suits perfectly, the project also features an optimization phase.

It is for this purpose that PyGMO will be used. PyGMO is in fact a scientific Python library for massively parallel optimization and provides a unified collection of optimization algorithms and problems [31]. It comprehends a wide list of optimization algorithms. Multi-objective Hypervolume-based Ant Colony Optimizer (MHACO), one of the promising candidates found in the literature review, is present there, but there are also algorithms capable of handling mixed-integer non-linear problems, an important feature that could be needed.

7

Numerical Methods

The following chapter on numerical methods provides an overview of several techniques used in numerical analysis, including root-finding algorithms, interpolation schemes, integration schemes, and optimization algorithms.

7.1. Root-finding algorithms

Root-finding algorithms are numerical methods used to determine the roots, or zeros, of a function. These algorithms are commonly used to solve equations that cannot be solved analytically. Root-finding algorithms include many techniques. Here, regula falsi, bisection, and the secant method will be presented.

7.1.1. Regula Falsi

The Regula Falsi method, also known as the method of false position, is a numerical method for finding roots of a function $f(x)$ in a given interval $[a, b]$.

Algorithm

The method starts with two initial guesses, $x_0 = a$ and $x_1 = b$, and, given that $f(x_0)$ and $f(x_1)$ have opposite signs, it calculates the next approximation, x_2, using the formula:

$$x_2 = x_1 - f(x_1)\frac{x_1 - x_0}{f(x_1) - f(x_0)} = \frac{x_0 f(x_1) - x_1 f(x_0)}{f(x_1) - f(x_0)} \tag{7.1}$$

If $f(x_2) = 0$, or $f(x_2)$ has a lower value than a set accuracy, then x_2 is the root. Otherwise, a new interval is chosen based on the signs of $f(x_0)$, $f(x_1)$, and $f(x_2)$, and the process is repeated until the desired accuracy is achieved. The new interval is chosen as follows:

- If $f(x_0)$ and $f(x_2)$ have opposite signs, the root is in $[x_0, x_2]$.
- If $f(x_1)$ and $f(x_2)$ have opposite signs, the root is in $[x_2, x_1]$.

The Regula Falsi method is a bracketing method, which means that it guarantees convergence to a root if the initial interval brackets a root and the function is continuous in the interval. However, the method can be slow to converge, especially if the function is highly nonlinear or has multiple roots in the interval.

Illinois addition

An improved version of the Regula Falsi method is the Illinois algorithm, which halves the value of the retained interval boundary edge when the new x_2 value has the same sign as the previous one.

$$x_2 = \frac{\frac{1}{2}x_0 f(x_1) - x_1 f(x_0)}{\frac{1}{2}f(x_1) - f(x_0)} \quad \text{or} \quad x_2 = \frac{x_0 f(x_1) - \frac{1}{2}x_1 f(x_0)}{f(x_1) - \frac{1}{2}f(x_0)} \tag{7.2}$$

The Illinois algorithm can converge faster than the Regula Falsi method, especially when the function has a steep slope near the root. However, it may also require more function evaluations per iteration.

7.1.2. Bisection

The bisection algorithm is a simple and robust numerical method for finding the root of a function $f(x)$ in a given interval $[a, b]$. The method starts by evaluating the function at the midpoint $c = (a + b)/2$ of the interval. If $f(c) = 0$, or $f(c)$ has a lower value than a set accuracy, then c is the root. Otherwise, a new interval is chosen based on the signs of $f(a)$, $f(b)$, and $f(c)$, and the process is repeated until the desired accuracy is achieved. The new interval is chosen as follows:

- If $f(a)$ and $f(c)$ have opposite signs, the root is in $[a, c]$.
- If $f(b)$ and $f(c)$ have opposite signs, the root is in $[c, b]$.
- Otherwise, c is a stationary point of the function and the method fails to converge.

The bisection algorithm is guaranteed to converge to a root if the function is continuous and changes sign in the interval $[a, b]$. However, the method may converge very slowly, especially if the function is highly nonlinear or if the interval is wide. The convergence rate is proportional to the width of the interval and decreases by a factor of 2 with each iteration.

7.1.3. Secant method

The secant method is a numerical method for finding the root of a function $f(x)$ that requires only one initial guess. The method uses a sequence of approximations $x_0, x_1, x_2, \ldots$ that are obtained by linearly interpolating between two previous approximations x_{n-1} and x_n. Specifically, the next approximation x_{n+1} is given by:

$$x_{n+1} = x_n - \frac{f(x_n)(x_n - x_{n-1})}{f(x_n) - f(x_{n-1})} \tag{7.3}$$

If $f(x_{n+1}) = 0$, or $f(x_{n+1})$ has a lower value than a set accuracy, then x_{n+1} is the root. Otherwise, the method is repeated until the desired accuracy is achieved. The secant method is a quasi-Newton method, which means that it uses only function values and does not require the calculation of derivatives. However, the method may converge slowly or fail to converge if the function has a flat slope near the root or if the initial guess is far from the root. The convergence rate of the method is roughly equal to the golden ratio $(1 + \sqrt{5})/2 \approx 1.618$, which is faster than the linear convergence of the bisection method but slower than the quadratic convergence of Newton's method.

7.2. Interpolation

Lagrange interpolation is a method of constructing a polynomial that passes through a set of n data points $(x_1, y_1), (x_2, y_2), \ldots, (x_n, y_n)$. The polynomial has degree at most $n - 1$, which means that it has the form:

$$L(x) = \sum_{i=1}^{n} y_i \ell_i(x)$$

where $\ell_i(x)$ is the ith Lagrange basis function, which is defined as:

$$\ell_i(x) = \prod_{j \neq i} \frac{x - x_j}{x_i - x_j}$$

The Lagrange basis functions have the property that $\ell_i(x_j) = \delta_{ij}$, where δ_{ij} is the Kronecker delta function. This means that $L(x_i) = y_i$ for all i, which implies that the polynomial passes through all the data points.

The accuracy of the Lagrange polynomial depends on the spacing and distribution of the data points. In general, the polynomial may oscillate or exhibit spurious behavior near the edges of the data range, especially if the data points are clustered or unequally spaced. In practice, it is common to use an interpolating polynomial of a lower degree or a smoothing function to avoid these issues.

For the current project, an 8th-order interpolator has been used, which is already available in TUDAT. It has been found that such an order provides a good trade-off between accuracy and stability.

7.3. Numerical Integration

The integration scheme is an instrument that will be used to compute the trajectories followed by the spacecraft. The RKF method is here described.

The Runge-Kutta-Fehlberg (RKF) method is a popular numerical scheme for solving ordinary differential equations (ODEs) that combines two different orders of the Runge-Kutta method to achieve high accuracy and efficiency. The method uses an adaptive step size strategy to adjust the integration step based on the error estimate, which allows it to handle stiff or non-stiff ODEs with varying degrees of smoothness.

The RKF method is based on two sets of coefficients, denoted for example as RKF7 and RKF8 for the RKF7(8) method. The RKF7 coefficients correspond to a seventh-order scheme, while the RKF8 coefficients correspond to an eighth-order scheme. The method works by integrating the ODE over a single time step h using both the RKF7 and RKF8 schemes, and then using the difference between the two solutions to estimate the local truncation error. If the error is below a specified tolerance level, the solution is accepted and the step size is increased. If the error is above the tolerance level, the solution is rejected and the step size is decreased. This process is repeated until the entire time interval is covered.

The RKF method is particularly useful when the solution of the ODE changes rapidly in some regions and slowly in others. By adjusting the step size in each region accordingly, the method can achieve high accuracy without requiring a large number of function evaluations. However, the method may be less efficient than other methods for ODEs that have a relatively smooth solution or do not require high accuracy.

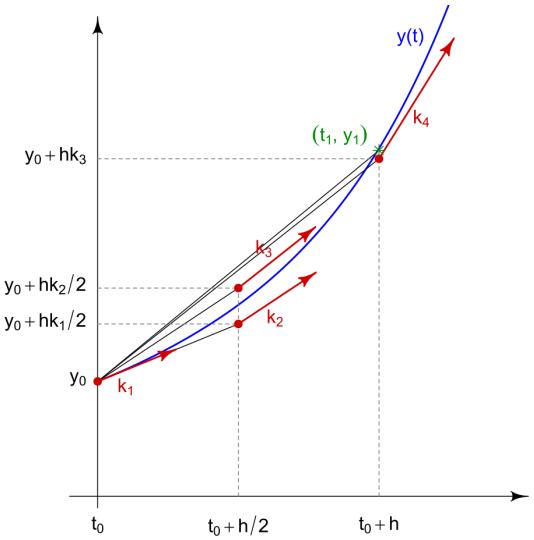

Figure 7.1: Working principle of a Runge-Kutta integration scheme [32].

The selected case study is particularly suited for RKF methods since it features dynamics that change rapidly in some regions and slowly in others. In particular, the RKF7(8) method has been selected as an integration scheme already during the literature review.

7.4. Propagation scheme

The choice of the propagation scheme shapes the equations of motion, which will take different forms based on the variables that will be used. As propagation scheme, the *Unified State Model* with quaternions USM7 has been chosen.

The *Unified State Model* is a singularity-free representation of the equations of motion. This peculiarity is achieved by defining a satellite's motion in a three-dimensional space with seven parameters instead of six.

The USM7 version uses quaternions as well as the velocity hodograph to define the state of a spacecraft, and its main advantage as said is the absence of singularities regarding the 3D motion of the spacecraft. One last singularity remains, that is the one reached when approaching the limiting true anomaly in hyperbolic orbits. Another drawback consists of the numerical integration of quaternion elements that causes noise and deviations of norm; an issue whose first-order effect can be removed, but still persists [22].

8

Verification & Validation Material

Verification and validation tools and data are crucial for ensuring the reliability of aerocapture trajectory studies at Jupiter. This chapter will explore the methods and tools used to verify and validate spacecraft trajectories during high-speed atmospheric entry and braking maneuvers, as well as the environment of Jupiter in general.

8.1. Verification

The verification tools for the aerocapture problem are presented here.

8.1.1. GTOPX

Stemming from the well-known, but no longer maintained, GTOP database published in 2005 by ESA, the Global Trajectory Optimisation Problem with eXtension (GTOPX) database adds new problems to the initial GTOP, precisely problems featuring mixed-integer and multi-objective properties [33]. The material regarding the GTOPX database can be found at MIDACO-SOLVER [34].

Since the selected science case can be modeled as a multi-objective problem that also includes integer and floating-point decision variables, using one of the mixed-integer and multi-objective problems provided by this extended GTOP database would result in a reliable benchmark of the selected study case.

8.1.2. Numerical simulations

Numerical simulations of aerocapture at Jupiter have the potential to serve as a powerful verification tool for analytical models of aerocapture. Analytical models use simplified equations and assumptions to predict the behavior of a spacecraft during aerocapture, but they may not capture the full complexity of the interaction between the spacecraft and the planet's atmosphere. Numerical simulations, on the other hand, use computer models to solve the full set of equations governing the motion of the spacecraft and its interaction with the atmosphere, expected to provide a more accurate and detailed picture of the process. By comparing the results of numerical simulations with those predicted by analytical models, a better understanding of the strengths and limitations of each approach can be gained and the current understanding of the aerocapture process be refined.

8.2. Validation

The validation material for Jupiter's atmosphere and environment, coming from the Galileo and Juno missions, is presented here.

8.2.1. Galileo

The available validation data from the Galileo mission consists of trajectory data, SPICE kernels, and reconstructed heat loads data.

Trajectory data
The available validation material from the Galileo mission comes from the reconstructed in-flight data available in Table B.2 in the appendix. Here, values for the trajectory geometry such as the probe altitude, velocity, and flight path angle, are displayed with respect to the elapsed time. Other probe parameters are presented as well, such as its mass and diameter profiles and its C_D coefficient during the entry. Moreover, flowfield parameters such as the Mach, Reynolds, and Knudsen numbers are also presented.

SPICE kernels
NASA's SPICE kernels are sets of data files that contain information about the geometry, position, and movement of celestial bodies. Some SPICE kernels for the Galileo mission, which explored Jupiter and its moons in the 1990s, are available as validation material [35]. These kernels can be used for testing the accuracy of simulation models of Jupiter's atmosphere. By comparing the output of such models with the data contained in the SPICE kernels, reliability and accuracy of these models can be ensured. This is particularly important in fields such as space exploration, where even small errors in calculations can have significant consequences on the final trajectory.

The curators of this library for the Galileo mission however warn that *"this collection is still being assembled and validated, after which it will be put through PDS peer review. It is not yet complete."*[1]

Such data set could still be used, but its validity alone would be limited.

Heat loads
Heat loads data has been reconstructed by Park [37], and their steady-state solutions for the stagnation point can be found in Table 10.4.

The altitude range is between 100 and 200 km, where the majority of the ablation occurred. These results are the closest match between flight and simulation data for heat fluxes.

8.2.2. Juno
The validation data taken from NASA's SPICE kernels of the Juno mission provides crucial information for testing and improving simulation models for the spacecraft's arrival trajectory.

SPICE kernels
Real orbital data about the Juno probe can be found at NASA SPICE Kernels [19]; data that can be used to verify the accuracy of the physical model, at least partially, by simulating the trajectory of Juno with the given model and comparing the trajectory with Juno orbital data. The impact of the Jovian atmosphere on a spacecraft trajectory, for example, cannot be validated with such data.

[1] PDS stands for Planetary Data System; it is a long-term archive of digital data products returned from NASA's planetary missions [36].

Part III

Problem Definition & Modeling

9 Problem Definition

The mathematical and logical definition of the problem is a necessary step for its solution. In this chapter, the trajectory geometry, the spacecraft properties, and the problem requirements will be presented. Additionally, an assessment of some requirements will be performed to verify that the initial assumptions hold under the problem's conditions.

9.1. Trajectory geometry and configuration

The trajectory that will be investigated will start at the edge of Jupiter's sphere of influence (SoI), so it will comprehend only the approach phase of a transfer from Earth to Jupiter. The initial position and velocity will be chosen by assuming an interplanetary Hohmann transfer that precedes Jupiter's approach phase.

The possibility of performing one flyby during the approach phase is considered, and after that, the spacecraft will perform an aerocapture entry at Jupiter's atmosphere with the scope of entering a bound orbit around the planet.

After the aerocapture phase, there is the possibility of performing one additional flyby, which will allow the spacecraft to raise its orbital pericenter and avoid a second atmospheric entry into the planet's atmosphere.

It is important to note that the trajectory will ideally be flown without any need for orbital maneuvers that require propellant. Later in this chapter it will be verified whether this assumption holds or not.

9.1.1. Flybys

A flyby is an orbital maneuver that consists of skimming over a planet or a moon, to change the shape of the original orbit by harnessing the gravitational pull of such body. A more detailed description of the flyby effect is given in Chapter 2.

Regarding the Jupiter system, flybys can be performed at the Galilean moons in order to reduce the orbital energy of the spacecraft, but the number of flybys that can be performed is limited. The more flybys are planned, the fewer times the favorable moon configuration would occur. For this reason, doing more than a double flyby would result in too few occurrences, thus posing a severe constraint on the launch time of the mission. If a double flyby is performed, it would be in the form of one pre- and one post-aerocapture flyby.

9.1.2. Areocapture

Aerocapture is a spaceflight maneuver that uses a planet's atmosphere to slow down a spacecraft and put it into an orbit around the planet. This technique involves using a combination of drag and heat generated by atmospheric friction and air compression to decelerate the spacecraft.

Thermal loads

The thermal loads a spacecraft has to withstand are a critical part of the aerocapture phase, thus their correct evaluation is crucial. A small survey on thermal loads will be done in Chapter 10, where the most accurate ways to evaluate them will be presented.

Theoretical corridor width

To perform aerocapture, the entry vehicle must enter the atmosphere within the aerocapture corridor bounded by the minimum and maximum acceptable Entry Flight-Path Angles (EFPAs) as shown in Figure 9.1. The minimum EFPA γ_{min} (undershoot limit) is the steepest EFPA at which the vehicle can enter and achieve the desired atmospheric exit conditions to achieve the target apoapsis. The maximum EFPA γ_{max} (overshoot limit) is the shallowest allowable for the vehicle to achieve the desired orbit upon atmospheric exit. The difference between the two bounding EFPAs is termed the theoretical corridor width (TCW), and it is a measure of the vehicle control authority [38].

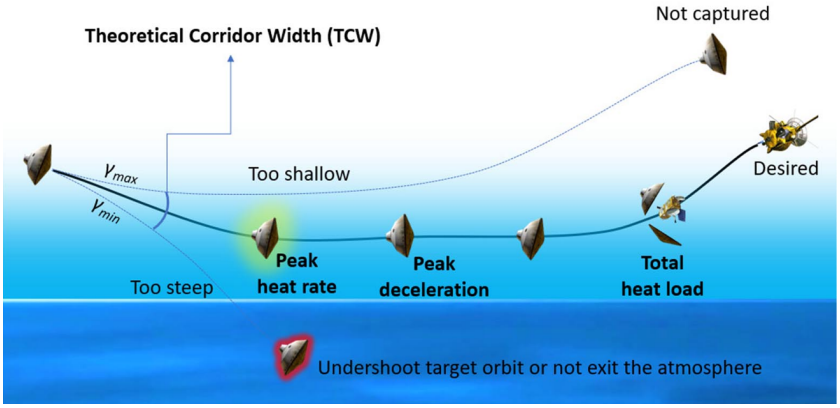

Figure 9.1: Theoretical corridor width (TCW) [38, Figure 2].

Feasibility

The entry TCW for a Jupiter atmospheric entry has been found to be of 0.4°[38] for a lift-modulated entry. The results of such a narrow entry corridor have the same assumptions as the current study, thus they can be considered to be valid results to be applied here as well.

Figure 9.3 shows the feasibility regions for lift and drag modulation aerocapture (for a visual depiction of those entry modulation techniques, see Figure 9.2). A primary observation is that drag modulation at Jupiter is unfeasible in the near future, as it requires too high ballistic coefficient ratios [38], whereas lift modulation can still be performed, although the presented scenario is far from optimal because of the narrow TCW.

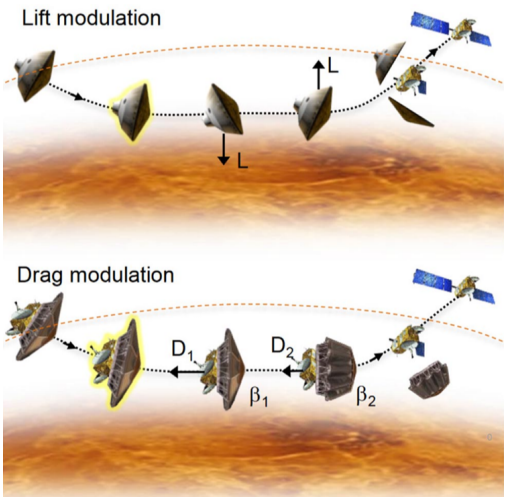

Figure 9.2: Two aerodynamic control approaches for an aerocapture vehicle: lift modulation and drag modulation; the dashed line indicates the atmospheric interface [39, Figure 1].

As can be seen, the most critical constraint comes from the maximum allowable peak heat flux q_w ($\dot{q}_w$ in the figure), whereas the limits on the maximum g-loads do not limit the feasibility space. The peak heat flux constraint selected by Girija et al. [38] is of 12000 W/cm^2, but for the current study it is set to 5000 W/cm^2, thus it can be expected that the feasibility region is narrower than what Figure 9.3 shows.

The arrival V_∞ range selected for the optimization in Chapter 15 is between 5 and 6 km/s (V_∞ = 5.6 km/s for a Hohmann transfer), thus well within the possible constraint line of 5000 W/cm^2 peak heat flux.

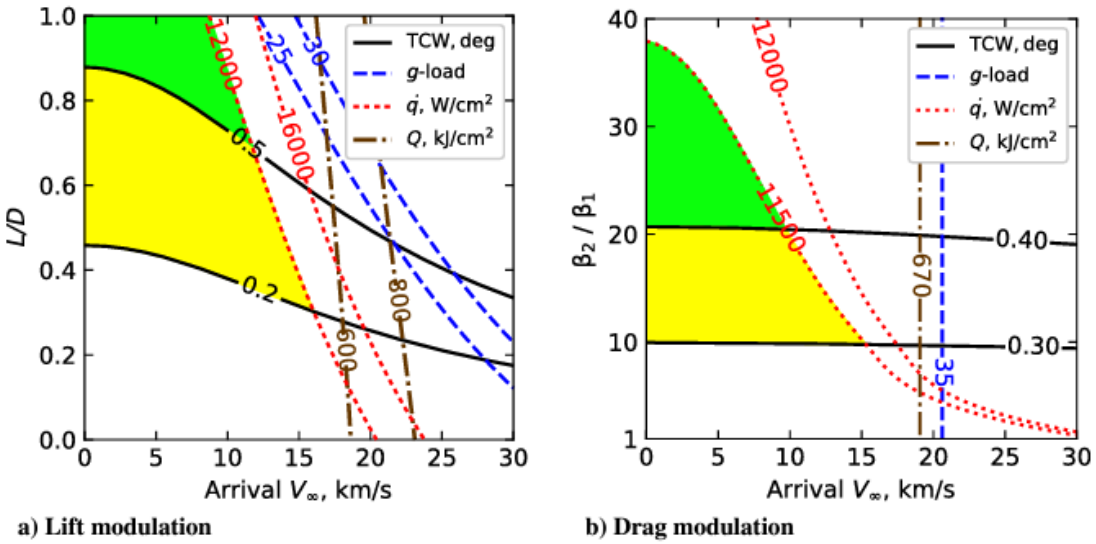

Figure 9.3: Aerocapture feasibility charts for Jupiter [38, Figure 9]. The green region indicates the feasible $(L/D, V_\infty)$ combination for lift-modulation aerocapture with a TCW limit of 0.5 deg. With a required TCW of 0.2 deg, the yellow region also becomes feasible. The same reasoning applies to the drag-modulation aerocapture. Here, β_2/β_1 indicates the ratio between the minimum and maximum achievable ballistic coefficients (see Figure 9.2).

9.1.3. Conventional-burn scenario

In a parallel scenario to an aerocapture maneuver, used for reference purposes here, a spacecraft would perform a similar trajectory, but instead of entering the planet's atmosphere, it would perform an insertion burn that would put it in a closed orbit around Jupiter. The insertion burn would happen at approximately 2000 km pericenter altitude. Unlike an aerocapture maneuver, which uses the planet's atmosphere to slow down and capture the spacecraft into orbit, an insertion burn relies on the spacecraft's propulsion system to slow down and achieve the desired orbit. This method requires propellant to be carried on board compared to an aerocapture maneuver, but it offers more precise control over the spacecraft's trajectory and avoids potential risks associated with the atmospheric entry. Additionally, an insertion burn can be used for missions that do not require the spacecraft to enter the planet's atmosphere, such as remote sensing or communication satellites.

The mass fraction of the propellant required for the insertion burn would be calculated by using the following formula, which is a readaptation of the rocket equation taken from Girija et al. [38]:

$$f_{\text{prop}} = 1.12\left(1 - \exp\left[-\frac{\Delta V_{\text{OI}}}{I_{\text{sp}} g_0}\right]\right) \tag{9.1}$$

where 1.12 is an assumed tankage factor to account for the structural mass of the propulsion system (the original value for the rocket equation is 1), ΔV_{OI} is the orbit insertion ΔV, I_{sp} is the propulsion system specific impulse, and $g_0 = 9.80665$ m/s^2 is the standard free-fall acceleration. The orbit insertion ΔV is computed by considering the ΔV needed to achieve a final orbit with 0.98 eccentricity.

An $I_{\text{sp}} = 320$ s will be used, as Girija et al. [38], assuming a conventional bipropellant engine.

9.1.4. Comparison rationale

The comparison, between the classical approach of using an impulsive manevuer and the aerocapture technique, will feature both quantitative and qualitative indicators:

- Technique-related deliverable payload mass fraction (payload is intended as any other subsystem that is not related to the orbit insertion - instruments + bus)
- Spacecraft shape configuration constraints
- Technique-related risks (flyby constraints, radiation...)

They will be used later in the final assessment.

Payload mass calculation

To calculate the payload mass fraction each technique can deliver, the required mass for orbit insertion each technique uses has to be subtracted from the spacecraft's total mass. It is important to note that for this study "payload mass" indicates the mass of the payload but also the mass of the spacecraft's bus, minus the mass of the orbital insertion subsystem. The payload mass fraction calculation has been taken from Girija et al. [38]. The total mass can be expressed in the following way for the aerocapture scenario:

$$M_{\text{Total}} = M_{\text{ESS}} + M_{\text{TPS}} + M_P \tag{9.2}$$

where M_{TPS} is the TPS mass, M_{ESS} is the Entry Support System (ESS) mass [1], and M_P is the useful payload mass, and for a classical insertion burn scenario:

$$M_{\text{Total}} = M_{\text{prop}} + M_P \tag{9.3}$$

where M_{prop} is the propellant mass.

To calculate the payload mass fraction each technique can deliver, the following equations will be used:

$$f_{P,\,\text{prop}} = 1 - f_{\,\text{prop}} \tag{9.4}$$

where $f_{P,\,\text{prop}} = M_P/M_{\text{Total}}$ and $f_{\,\text{prop}} = M_{\text{prop}}/M_{\text{Total}}$;

$$f_{P,\text{ac}} = 1 - f_{\text{ESS}} - f_{\text{TPS}} \tag{9.5}$$

where $f_{P,\,\text{ac}} = M_P/M_{\text{Total}}$, entry support systems mass fraction $f_{\text{ESS}} = M_{\text{ESS}}/M_{\text{Total}}$, and TPS mass fraction $f_{\text{TPS}} = M_{\text{TPS}}/M_{\text{Total}}$. Note that f_{ESS} in Equation 9.5 depends upon the assumption of including or not a GNC system in the spacecraft. If included, it can be assumed that such a fraction would be $f_{\text{ESS}} \sim 0.23$ [38], resembling that of the Mars Science Laboratory.

9.2. Spacecraft Properties

The main properties of a hypothetical spacecraft that would fly within Jupiter's atmosphere are here presented.

General properties

The spacecraft's mass is assumed to be about 2000 kg. Its area will be 5 m^2, and its nose radius will be that of the Galileo probe, which is 0.222 m.

Aerodynamics

The shape of the entry capsule will resemble that of the Galileo probe. It will be shaped to have a 45-degree inclined frustum, a body radius[2] of 1.26 m. Refer to Figure 4.1 for its full shape (cfr. Figure 9.3).

As drag and lift coefficients, values of 1.2 and 0.6 have been chosen. They would result in a lift-to-drag ratio of 0.5, which would be expected for an aerocapture entry at Jupiter.

Thermal Protection Subsystem

As Thermal Protection Subsystem (TPS), the Heatshield for Extreme Entry Environment Technology (HEEET) has been selected, due to its low mass and suitability for atmospheric entry at gas giants [40].

Structure and radiation shielding

For shielding, the spacecraft will feature a 1-cm thick outer shield of Aluminum as the Europa Clipper mission would [41]. Expressed in g/cm^2, the shield thickness would be 2.7 g/cm^2, since the density of Aluminum is 2.7 g/cm^3.

[1] The ESS includes aeroshell structure, guidance and navigation systems, and other supporting equipment that is not considered useful payload delivered to orbit [38].

[2] The body radius for the current project has been used as nose radius, as the heat flux validation process has been brought out with Galileo's body radius. Investigating the reason behind the discrepancies that arise when using the true nose radius is beyond the scope of the project.

9.3. Problem Requirements

The requirements of the problem, as well as the constraints, are presented here.

9.3.1. Problem functional requirements

The following requirements define what the spacecraft has to do. Due to the non-specific nature of the mission under study, only few functional requirements are necessary.

Capture trajectory
The spacecraft has to enter a closed and stable orbit around Jupiter.

Final orbit
The final orbit must allow rather frequent close encounters with Jupiter but it also must avoid spending large amounts of time in high-radiation areas.

9.3.2. Problem non-functional requirements

The following requirements describe the general properties of the mission.

State position error
The state position error can vary along the trajectory since different phases of the mission require different precision in position. The state position error would depend on the navigation accuracy of the spacecraft during the trajectory, thus depend on the onboard instrumentation. As a reference, the Juno mission to Jupiter has been taken, since it flew an approach trajectory comparable to that of the following problem. It is set as follows:

- The state position accuracy has to be of the order of 100 km during the arrival trajectory.
- The state position accuracy has to be of the order of 10 km during the flybys.
- At atmospheric entry, the position accuracy has to be of the order of 10 km.
- During the aerocapture phase, the position accuracy has to be of the order of 100 km.
- After the aerocapture phase, the position accuracy has to be of the order of 50 km.

The accuracy requirements have been set according to the results of the Juno mission. The ground-based radiometric position error of the Juno mission has been taken as the primary reference. During the beginning of its approach phase, the position error was close to 300 km. It then rapidly came down to 100 km as the spacecraft came closer to Jupiter, and it remained approximately constant until some weeks prior to the insertion burn when it came down to 50 km. By using optical navigation, as proposed by Bradley et al. [18], the error can be brought down to a few kilometers during the last week prior to the insertion burn. During the insertion burn, the position error rose to 100 km, to decrease again to 50 km in the post-burn orbit. During and after atmospheric entry similar values are expected. All such information is displayed in Figure 9.4.

For what concerns flybys, due to the fast dynamics and the high sensitivity of those phases, the position accuracy that is required for the atmospheric entry has been selected there as well.

State velocity error
The state velocity error is as well a requirement with different thresholds along the trajectory. The state velocity error would as well as the position error depend on the navigation accuracy of the spacecraft during the trajectory, thus depend on the onboard instrumentation. As a reference, the Juno mission to Jupiter has been taken here as well.

It is set as follows:

- The state velocity accuracy along the arrival trajectory has to be of the order of 0.1 m/s
- The state velocity accuracy has to be of the order of 10 m/s during the flybys.
- At atmospheric entry, the velocity accuracy has to be of the order of 0.1 m/s
- The state velocity accuracy has to be of the order of 10 m/s during aerocapture
- The state velocity accuracy has to be of the order of 0.1 m/s after aerocapture

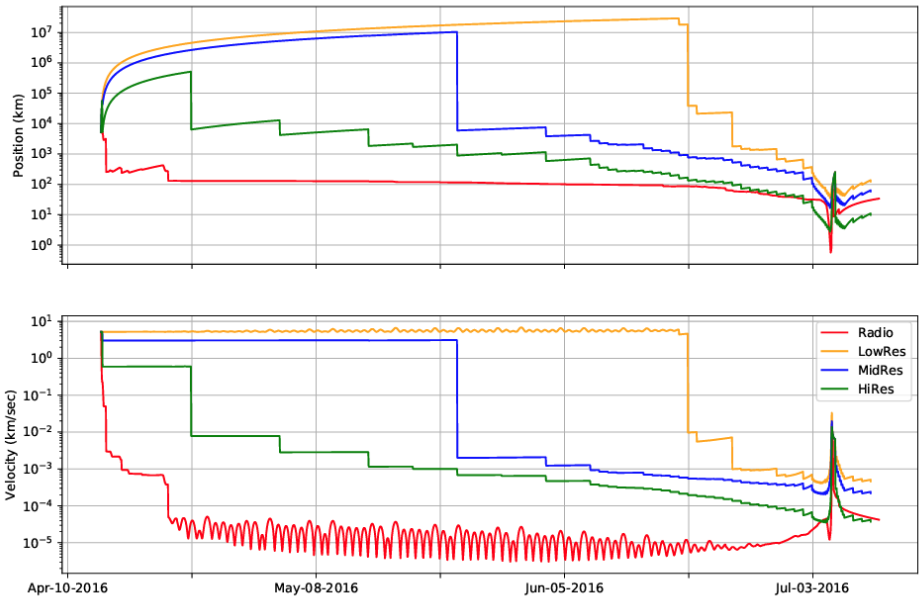

Figure 9.4: Current state uncertainty for the Juno approach trajectory. In red (the most accurate profile) is shown the actual performance of the ground-based radiometric-only solution from the as-flown trajectory. The other trends indicate the performance of the optical-only solutions, using different kinds of optical cameras [18, Figure 3].

The ground-based radiometric measurements of the Juno mission have been taken as the primary reference for the velocity as well, again referring to Figure 9.4. During the beginning of the Juno approach phase, the error in velocity was close to 3 m/s. Along the trajectory, it came down to values around 0.1 m/s, as the spacecraft came closer to Jupiter. It then slowly increased when coming closer to the insertion burn, but it still remained within the 0.1 m/s level.

During the insertion maneuver, the velocity error rose to 10 m/s, then decreased again to less than 0.1 m/s. Similar values for an aerocapture entry can be expected, thus the velocity accuracy requirement has been set accordingly.

For flybys the same accuracy set for the atmospheric entry has been selected, due to the fast dynamics of such phases which would make it difficult to have highly accurate measurements of the velocity.

Flight path angle at atmosphere entry interface

- The flight path angle must be accurate within $\pm 0.1°$

With a theoretical entry corridor width of 0.4°[38], the accuracy of the flight path angle at atmospheric entry is crucial for the success of an aerocapture mission at Jupiter.

Such high accuracy has been achieved for entry missions at Earth and Mars atmospheres, but for conceptual atmospheric entry trajectories at the gas giants (and Titan), the entry accuracy has been estimated to be about 25% of the entry corridor width, which in those cases was about 2°[38]. There is no analogue study about a Jupiter entry, but it can be assumed that the accuracy would be comparable to that achievable for other gas giants. Setting the required accuracy to $\pm$ 0.1°, that is 25% of the entry corridor width, makes it a reasonable guess, although it can be considered quite optimistic.

Required lift-to-drag ratio

- L/D has to be between 0.5 and 1.5.

Previous aerocapture missions featured vehicles with lift-to-drag ratios ranging from 0.5 to 1.5 [42]. Low lift-to-drag ratios (values lower than 0.5) result in unfeasible trajectories for Jupiter [38], whereas high ratios (higher than 1.5) are difficult to achieve with blunt bodies. The selected interval is hence particularly suited for the current mission.

CPU time per simulation

- The CPU time per simulation must not exceed 0.2 s.

A CPU time per simulation that meets this requirement would allow a batch of 30000 simulations to take 1h to compute. With such speed, enough flexibility would be guaranteed in running several simulation batches, even for debugging, without big losses of time that would result in a schedule delay.

9.3.3. Problem Constraints

Maximum peak heat flux

- The total wall incident heat flux must be lower than 5000 W/cm^2

which is the threshold above which the HEEET heatshield can no longer be used minus the maximum allowed uncertainty on the heat flux calculation. The HEEET is a heatshield specifically designed (Technology Readiness Level: 6) for atmospheric entry at gas giants [40], and is the best candidate for such entry, as will be discussed in Chapter 10.

Maximum aerodynamic acceleration

- The maximum aerodynamic acceleration experienced by the spacecraft must be lower than 30 g_E [38].

Minimum and maximum Jupiter distance

The arrival trajectory must remain contained within the sphere of influence of Jupiter, to avoid gravitational perturbations that might alter completely the trajectory geometry.

- The maximum distance from Jupiter has to be lower than 48.2 million km.

The spacecraft also cannot dive too deeply into Jupiter's atmosphere, otherwise it would experience unsustainable aerothermodynamic loads. As a comparison, the Galileo probe, which performed a ballistic entry at Jupiter, failed at an altitude of -35 km (with respect to the 1-bar pressure level). The minimum distance from Jupiter can be set to be higher than the 1-bar pressure level, which corresponds to the commonly accepted radius of Jupiter.

- The minimum distance from Jupiter's centre of mass has to be higher than 69946 km.

Minimum distance from moons

For the spacecraft not to collide with the Galilean Moons, it must keep a safe distance from them. A safety altitude for flybys at these moons is set to 100 km, which allows the spacecraft to avoid many of the risks connected to low-altitude flybys. The spacecraft must keep a distance from the moons higher than the following:

- r_I > 1921.6 km r_E > 1660.8 km r_G > 2734.1 km r_C > 2510.3 km.

The thresholds correspond to the radius of the moons with the safety altitude included. Subscripts I, E, G, C indicate the spacecraft distance respectively from Io, Europa, Ganymede, and Callisto.

Final orbit eccentricity

- The eccentricity of the final orbit must be lower than 0.985

This is approximately the current eccentricity of the Juno spacecraft. It was initially meant to be inserted in a less eccentric orbit, but due to a malfunction in the propulsion system, the spacecraft has been kept to its initial orbit of 53 days period. An orbital eccentricity that would go above this level would result in an orbit particularly sensitive to environmental perturbations, thus very unstable. It could even result in the spacecraft being ejected outside the Jupiter system, in the unfortunate case of a gravitational interaction with one of the main moons of Jupiter.

Final orbit pericenter

- The pericenter altitude of the final orbit must be higher than or equal to 1000 km

To avoid a second deep atmospheric entry of the spacecraft, the final orbit pericenter must be adjusted to meet this requirement. At this altitude, the magnitude of the drag perturbation is close to that of the moon Io, thus negligible compared to the gravitational forces of Jupiter.

The drag force could however be powerful enough to effectively perturb the spacecraft after several repeated passages. The effect would be an eccentricity reduction, thus it would be actually optimal at the beginning of the mission to better stabilize the orbit. It is then considered a desired effect for the purpose of this study. A detailed mission analysis would have to consider whether and for how long this aerobraking effect could or should be used.

Interplanetary arrival velocity direction

- The Sun-asymptote phase angle must fall within 70-110 degrees.

The sun-asymptote phase angle indicated the interplanetary direction from which the spacecraft arrives at Jupiter. The arrival phase angle of an optimal Hohmann transfer would be 90 degrees. Small deviations are accepted since the spacecraft could follow a faster, or propellant-saving, trajectory that would result in a slightly smaller or larger angle at arrival. Deviations that do not comply with the requirement are most likely the results of unfeasible transfer trajectories, thus will not be considered.

9.4. Non-functional Requirements Validity Assessment

Since the problem assumes that no corrective maneuvers are needed along the approach phase, a sensitivity study on some non-functional requirements is performed to verify this assumption.

For such analysis, simulations were run in batches of 100s, and the selected parameter of the analysis has been randomly perturbed by following a Gaussian distribution. The standard deviations (1σ) of the distributions have been set so that an interval of 3σ would encompass 99.7% of the admissible perturbation cases. A 3σ interval would encompass the entire uncertainty band for a selected requirement. Different requirements that regarded just some trajectory parts were assessed by just propagating those portions of the trajectory. This allowed for a more in-depth analysis of the single parts of the trajectory for such cases.

A full-trajectory analysis would return more complete and continuous results, but for the purpose of the current work it has been deemed unnecessary.

As a note, the Mersenne Twister has been used as the core module for the random generation of numbers [43]. It is available in Python in the ”random” module. The nominal seed number that has been used is 50, but results have been tested with other numbers such as 100, 150, and 200.

9.4.1. State position error assessment

The requirements for the position have been set based on the navigation accuracy of the Juno spacecraft. To verify their validity under the assumption of no corrective maneuvers, the sensitivity of the problem to perturbations in position at different stages of the trajectory has been assessed.

For this case, the initial position of the propagation has been randomly perturbed in the RSW frame (see Chapter 5 for a description of the RSW frame) for each simulation. Both single-axis and multiple-axis uncoupled and coupled perturbed simulations were performed, but only the most remarkable results are shown here.

The choice to perturb the initial position of the trajectory arc has been made because it is the state, among all those along the arc, that would lead to the biggest errors at the end of the propagation. Errors applied early in the propagation have more time to build up and get bigger, thus the earlier a perturbation is applied, the bigger the final error is going to be.

Arrival arc position accuracy

Here the position accuracy for the arrival arc, which goes from the beginning of the trajectory until the atmospheric entry, will be analyzed. No flybys are considered here.

For perturbation in all three R, S, and W axes, the Gaussian distribution of the initial position perturbation has been set with a standard deviation (σ) of 100 km so that an interval of 3σ would be equal to 300 km. This would be in accordance with the accuracy requirement of $\pm$300 km position accuracy.

Such interval has been seen to result in position errors up to 800 km in each direction at the atmospheric entry interface (t_E). Specifically, the greatest magnitude results along the R axis, whereas for the S and W axes, the final errors do not exceed 200 km. Velocity errors remained instead rather small, in fact, they did not exceed 3 m/s in any direction. Here again, the greatest magnitude resulted along the R axis. Results are shown in Figure 9.5.

The final position errors suggest that the required position accuracy of 100 km during the approach phase cannot be respected without the need for a GNC system, or by increasing our knowledge of the initial state accuracy. In fact, with an accuracy on the initial position of approximately 50 km in each direction, the 100-km position accuracy requirement for the approach phase would be met without any need for a GNC system.

Perturbations of the state position at the beginning of the trajectory do not lead to considerable variations in the entry flight path angle. The flight path angle in fact hardly changes, with variations of the order of 10^{-5} degrees. The airspeed, on the other hand, sees a variation of the order of 100 m/s (the airspeed depends also on the atmospheric region the spacecraft flies in). The effect of the initial position perturbation on these quantities can be seen in Figure A.1 in the appendix. The reported results are for perturbations singularly applied at each axis for different runs, thus a different case from that one of Figure 9.5. The individual effects have been preferred because of the predominance of the perturbations on the R axis, which make the effects of those on the S and W axes indistinguishable.

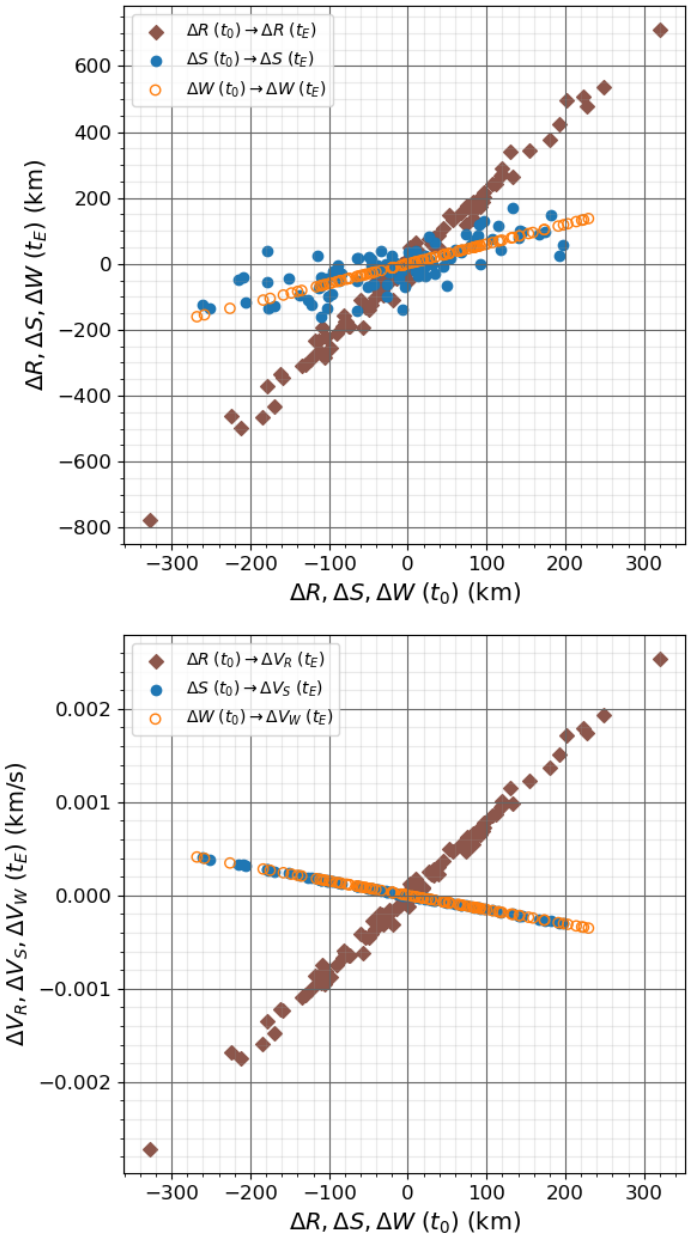

Figure 9.5: The RSW error at atmospheric entry (t_E) is shown in relation to the position perturbation of the initial state (t_0). Perturbations were applied along all three R, S, and W axes. The W axis shows an independent behaviour from the other two, meaning that it would only depend on an initial perturbation on that sole axis.

Having an airspeed with this great uncertainty is again another sign that such large errors in the initial position either have to be reduced or a GNC system has to be added to the equation.

Flyby phase position accuracy

The position error during flybys will depend on if and how they will be implemented. The following requirement of 10 km for each RSW direction in position is considered a first guess that resembles the accuracy for Juno during the insertion burn [18]. As said in Chapter 11, flybys are not part of the final problem, leaving this requirement to be evaluated as a recommendation.

Entry phase position accuracy

The position accuracy for the aerocapture phase at Jupiter has to be up to 100 km in each direction, but the uncertainty at the atmospheric entry interface has to be lower than 10 km in each direction.

The position accuracy at the atmospheric entry interface at Jupiter is clearly crucial for defining the quality of the aerocapture phase. A latitude/longitude change in entry position would translate into a different airspeed experienced by the capsule, which is a driving factor for aerocapture. This would eventually translate into a different atmospheric entry geometry, which would result in great differences in the final orbit, and entry aerothermal loads.

The entry position has been perturbed along the R, S, and W axes of the RSW frame, following a Gaussian distribution with a 3-σ interval of 10 km.

Results coming from such propagations show that the effects of perturbations along the R and S axes are strongly coupled, hence the final results show quite some noise regarding the trends in position and velocity error coming from these perturbations. Single-axis perturbations were also performed, and their results have been shown to closely match those of the combined R, S, and W perturbations, except for the absence of any noise in the results, which makes them easier to investigate. For this reason, the uncoupled effects on the R, S, and W axes have been presented in this case.

It can be seen in Figure 9.6 how perturbations on the initial position up to 10 km lead to position errors at the atmospheric exit that remain within 10-20 km. The altitude accuracy (R axis) is sensitive mostly to initial changes in the R axis, although it remains within a 5 km error. The entry trajectory, in general, is primarily sensitive along its S axis. Errors in the along-track direction (S axis) go easily up to 20 km for a perturbation in the R or S axes.

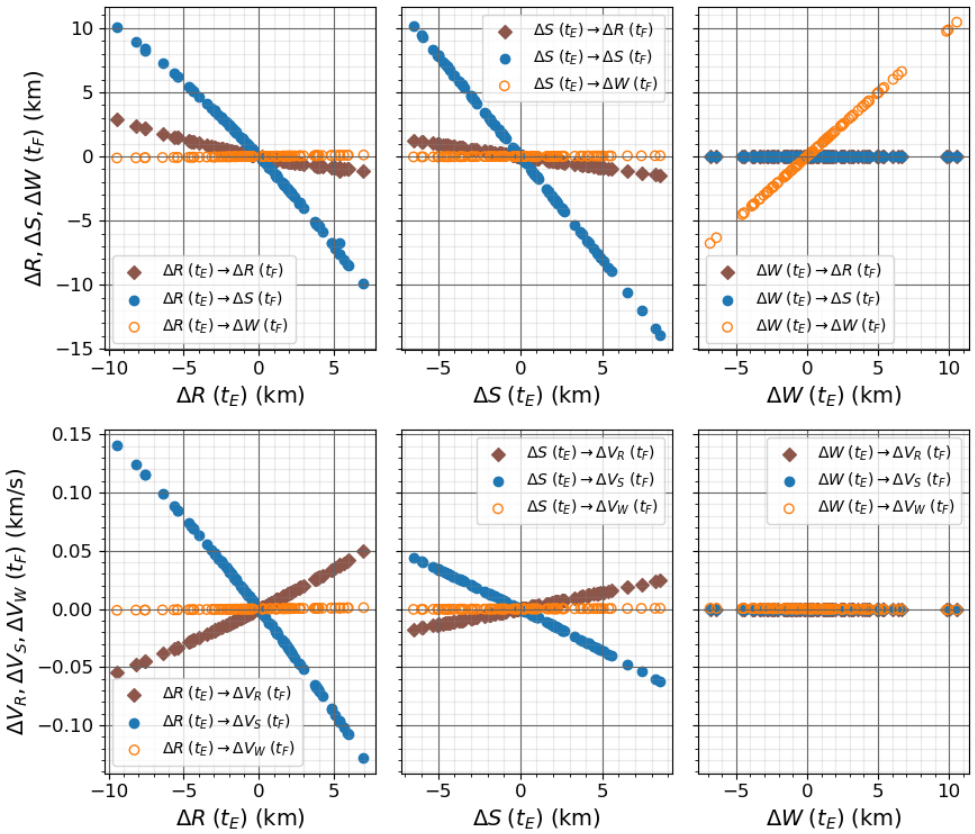

Figure 9.6: Resulting error in the R, S, and W components at the atmospheric exit epoch (t_F), when a single perturbation on the R, S, or W axis is applied (figures from left to right) at atmospheric entry (t_E). The top line shows the effect of the perturbation on the final position error (t_F), whereas the bottom line is for the final velocity error (t_F). Each figure shows the effect of the single perturbation on the simulations, thus their effects are evaluated separately and not coupled.

For what concerns the velocity error, Figure 9.6 shows how a perturbation in position along the R axis can lead to velocity errors up to 150 m/s in the along-track direction (S axis), which corresponds

to a direct change in velocity magnitude. A perturbation along this axis leads to the largest error in velocity, but final errors up to 50 m/s are present even for an initial perturbation along the S axis (at t_E). On the other hand, a perturbation in the across-track direction (W axis) leads to a negligible error in velocity.

For what concerns the error on peak heat flux (q_w) and total heat load (Q_w), an RSW position error at atmospheric entry would result in a peak q_w error of 500 W/m^2 and a Q_w error of 60 MJ/m^2 (Figure A.2). A different trajectory would mean different magnitudes of thermal loads, an aspect that in some cases could determine the success or failure of such a mission.

Post-aerocapture phase position accuracy

The required position accuracy for the post-aerocapture orbit is 50 km in each direction. Results from the atmospheric entry assessment showed that the accuracy at the atmospheric exit was about 20 km for a 10 km error at the entry interface. The orbit that follows from that is expected to be very sensitive to the entry conditions, hence its comparison to those.

The final orbit position accuracy has been evaluated by considering a position perturbation (3-σ interval of 10 km) at the atmospheric entry interface.

As presented in Figure 9.7, the final position accuracy exceeds the requirement by multiple orders of magnitude, since even small changes in position at the beginning of the atmospheric entry can result in million-km differences in the final orbit.

These results show how critical a GNC system would be during atmospheric entry. The resulting orbit would be too sensitive for a mission at Jupiter to be successful with no GNC system.

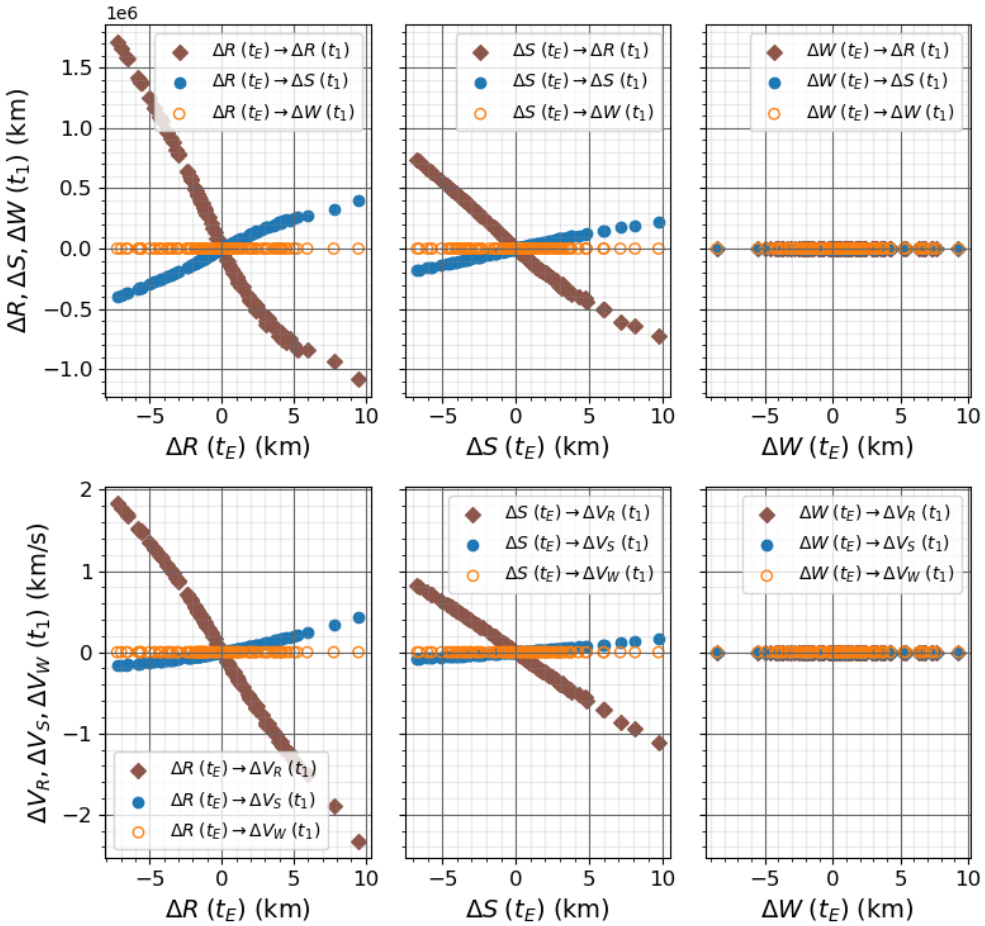

Figure 9.7: Resulting error in the R, S, and W components at the final orbit apocenter (t_1), when a single perturbation on the R, S, or W axis is applied (figures from left to right) at atmospheric entry (t_E). The top line shows the effect of the perturbation on the final position error (t_1), whereas the bottom line is for the final velocity error (t_1). Each figure shows the effect of the single perturbation on the simulations, thus their effects are evaluated separately and not coupled.
The W axis is here as well uncoupled from the other two, with much lower effects on position and velocity errors.

Another parameter that highlights how different the final orbit would be is its eccentricity. The eccentricity change resulting from these initial perturbations would be up to 0.01 (Figure A.3). Its value could seem rather small, however, for a nominal orbit that could have a 0.98 eccentricity even a 0.01 change could potentially result in a non-capture state, thus resulting in mission failure.

9.4.2. State velocity error assessment

The requirements for the velocity have been set as well based on the navigation accuracy of the Juno spacecraft. To verify their validity under the assumption of no corrective maneuvers, the sensitivity of the problem to perturbations in velocity at different stages of the trajectory has been assessed.

For this case as well, the initial velocity of the propagation has been randomly perturbed in the RSW frame (see Chapter 5 for a description of the RSW frame) for each simulation. Both single-axis and multiple-axis uncoupled and coupled perturbed simulations were performed. The most remarkable results from those are shown here.

Arrival arc velocity accuracy

Here the velocity accuracy for the arrival arc, which goes from the entry of the SoI until the atmospheric entry, will be analyzed. No flybys are considered.

For coupled perturbations in all three R, S, and W axes, the Gaussian distribution of the initial velocity perturbation has been set with a standard deviation (1σ) of 1 m/s so that an interval of 3σ would be equal to 3 m/s. This would be in accordance with the accuracy requirement of $\pm$3 m/s initial state velocity accuracy.

Such an interval has been seen to result in velocity errors up to 150 m/s in each direction at the atmospheric entry interface (t_E). Specifically, the greatest magnitude results along the R axis, whereas for the S and W axes, the final errors do not exceed 50 m/s. Position errors were strongly affected, as expected. They reached values up to 40000 km. Here again, the greatest magnitude resulted along the R axis. Results are shown in Figure 9.8.

The final velocity errors suggest that the required velocity accuracy of 0.1 m/s during the approach phase cannot be respected without the need for a GNC system, or by increasing our knowledge of the initial state accuracy. In fact, with an accuracy of approximately 3 m/s in each direction, the 0.1-m/s velocity accuracy requirement for the approach phase would be met without any need for a GNC system.

Moreover, perturbations of the state velocity at the beginning of the trajectory lead to considerable variations in the airspeed. The flight path angle varies up to 0.002 degrees, a value that cannot be completely ignored, but that is still below the required entry flight path angle margins. The airspeed, on the other hand, sees a variation up to 8 km/s, which exceeds the requirement by multiple levels of magnitude. The effect of the initial position perturbation

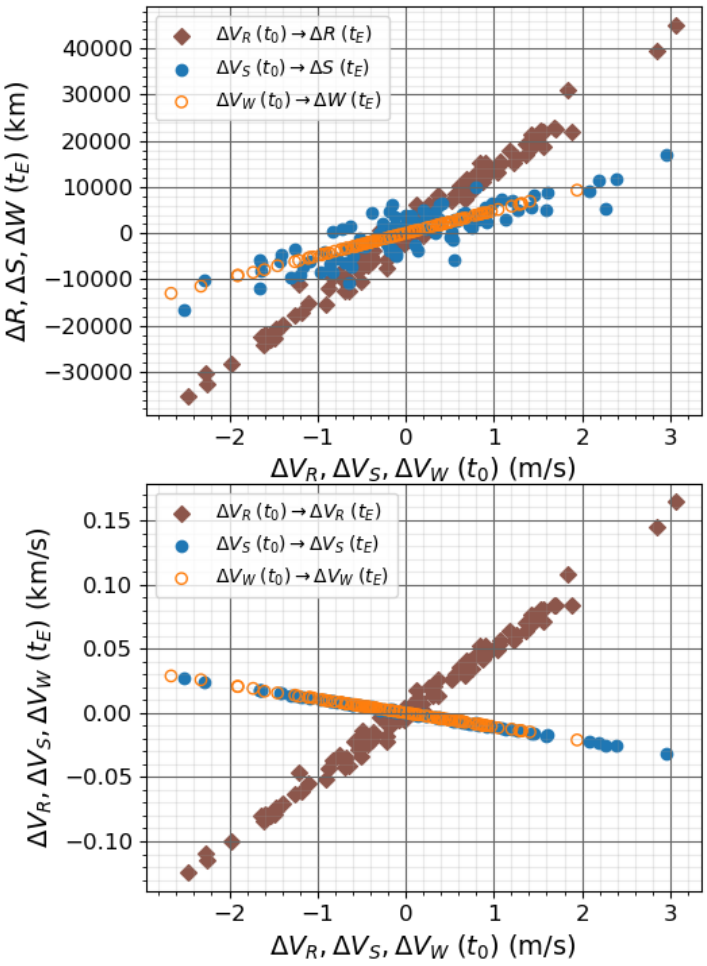

Figure 9.8: The RSW error at atmospheric entry (t_E) is shown in relation to the velocity perturbation of the initial state (t_0). Perturbations were applied along all three R, S, and W axes. The W axis shows an independent behaviour from the other two, meaning that it would only depend on an initial perturbation on that sole axis.

on these quantities can be seen in Figure A.4 in the appendix. The reported results are for perturbations singularly applied at each axis for different runs, thus a different case from that one of Figure 9.8. The individual effects have been preferred because of the predominance of the perturbations on the R axis, which make the effects of those on the S and W axes indistinguishable.

Due to the large position and velocity errors stemming from the initial state velocity uncertainty, it is clear that such large errors in the initial velocity either have to be reduced, or a GNC system has to be added to the equation.

Flyby phase velocity accuracy

The velocity error during flybys will depend on if and how they will be implemented. The following requirement of 10 m/s for each RSW direction in velocity is considered a first guess that resembles the accuracy for Juno during the insertion burn [18]. As will be said in Chapter 11, flybys are not part of the final problem, leaving this requirement to be evaluated as a recommendation.

Entry phase velocity accuracy

The velocity accuracy for the aerocapture phase at Jupiter has to be up to 10 m/s in each direction, but the uncertainty at the atmospheric entry interface has to be lower than 0.1 m/s in each direction.

The velocity accuracy at the atmospheric entry interface at Jupiter is another important parameter that drives the success of the mission. A change in the magnitude or direction of the velocity would translate into a different aerocapture trajectory, which would result in great differences in the final orbit, and entry aerothermal loads. The entry velocity has been then perturbed along the R, S, and W axes of the RSW frame, following a Gaussian distribution with a 3-σ interval of 0.1 m/s.

Figure 9.9 shows how perturbations on the initial velocity up to 0.1 m/s lead to velocity errors at the atmospheric exit that remain within the order of 0.1 m/s. The entry trajectory, in general, is primarily sensitive along its S axis. Errors in this along-track direction go easily up to 0.2 m/s for a perturbation at the entry interface.

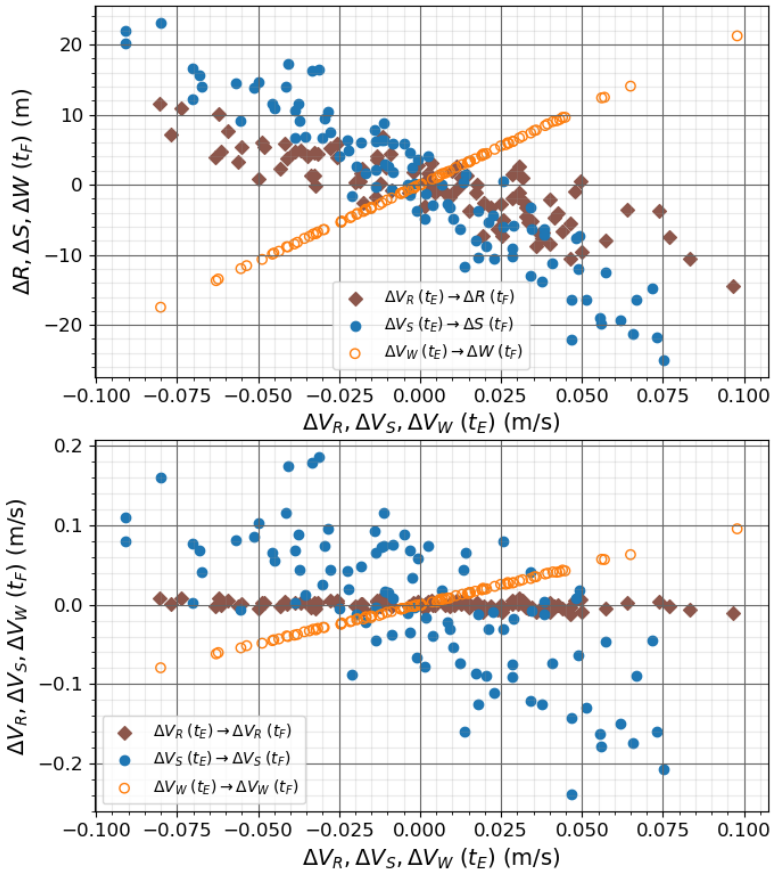

Figure 9.9: Resulting error in the R, S, and W components at the atmospheric exit epoch (t_F), when a velocity perturbation is applied at atmospheric entry (t_E). The top line shows the effect of the perturbation on the final position error (t_F), whereas the bottom line is for the final velocity error (t_F).

For what concerns the position error, Figure 9.9 shows how a perturbation in velocity of such magnitude does not produce considerable errors in position. Final errors are at most a few tens of meters and thus can be considered negligible.

For what concerns the peak heat flux (q_w) and total heat load (Q_w), such parameters hardly change for a velocity perturbation of 0.1 m/s, thus a trajectory with this uncertainty at the atmospheric entry would experience thermal loads comparable to the nominal one.

Post-aerocapture phase velocity accuracy

The required velocity accuracy for the post-aerocapture orbit is 0.1 m/s in each direction. Results from the atmospheric entry assessment showed that the accuracy at the atmospheric exit was about better or equal to 0.2 m/s for a 0.1 m/s error at the entry interface. The orbit that follows from that is expected to be very sensitive to the entry conditions, hence its comparison to those is made again.

The final orbit position accuracy has been evaluated by considering a position perturbation (3-σ interval of 0.1 m/s) at the atmospheric entry interface.

As presented in Figure 9.10, the final velocity error goes up to 3 m/s, which is only one order of magnitude greater than the 0.1-m/s requirement.

The final position error exceeds the requirement by multiple orders of magnitude, reaching 2000 km values for 0.1 m/s perturbations at the entry interface.

These results show as well how critical a GNC system would be during atmospheric entry. The resulting orbit would be too sensitive to velocity as well for a mission at Jupiter to be successful without a GNC system.

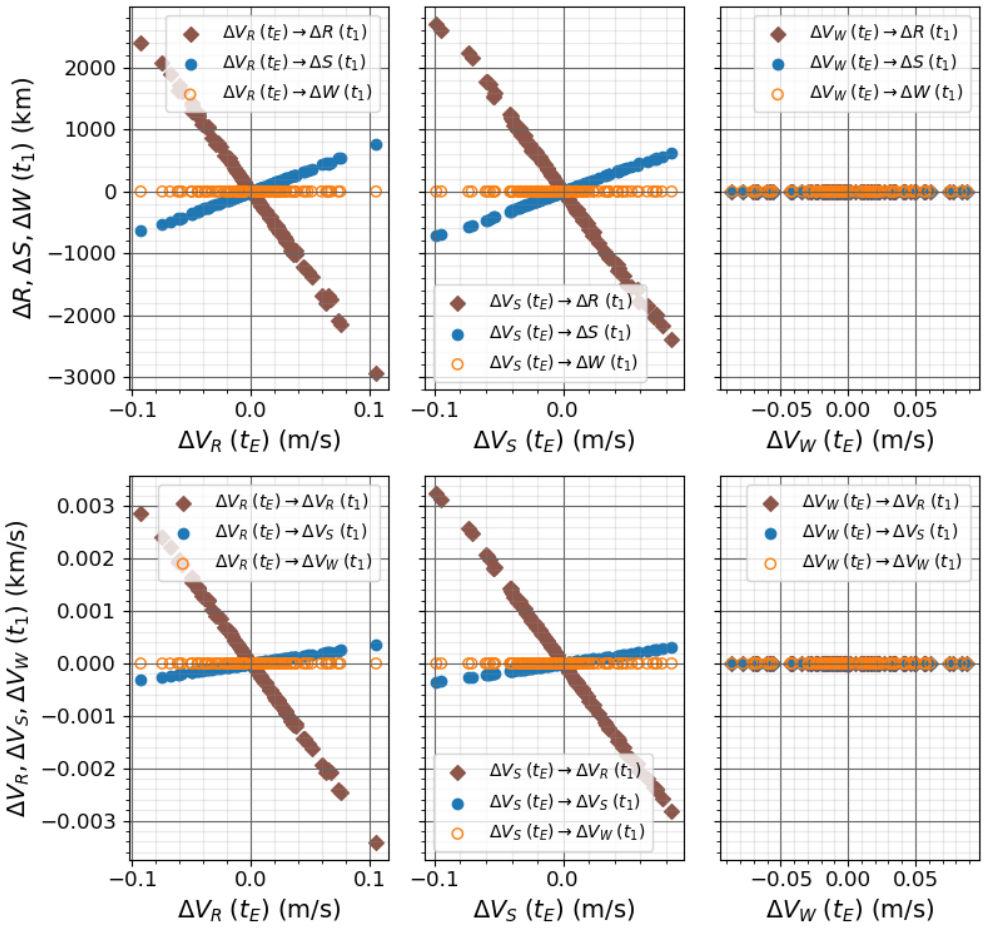

Figure 9.10: Resulting error in the R, S, and W components at the final orbit apocenter (t_1), when a single perturbation on the R, S, or W axis is applied (figures from left to right) at atmospheric entry (t_E). The top line shows the effect of the perturbation on the final position error (t_1), whereas the bottom line is for the final velocity error (t_1). Each figure shows the effect of the single perturbation on the simulations, thus their effects are evaluated separately and not coupled.

The eccentricity change of the final orbit for a velocity perturbation results to be negligible, hinting that an orbit that would respect the required position and velocity accuracy would be guaranteed to be in a captured state around the planet.

9.4.3. Observations

The results of the sensitivity analysis clearly show that a GNC system would be needed for an aerocapture trajectory at Jupiter that does not feature flybys. It would be needed both for the approach phase and the atmospheric entry to maintain the required position and velocity accuracy, assuring the spacecraft would end up in the desired orbit.

Another possibility would come from increasing the initial state accuracy, thus leading to lower navigation errors along the trajectory and meeting the expected requirements, but it is an unlikely scenario for the near future, thus the GNC option should be preferred.

Including a GNC system means that the mass required by all the entry-related sensors and instruments has to be accounted for, thus reducing the potential benefits from a ballistic aerocapture exercise.

10

Thermal Loads

The thermal loads for an aerocapture trajectory are the driving factor for the sizing of a spacecraft's heatshield. This chapter aims at finding effective ways of calculating the heat fluxes acting on a vehicle for a Jupiter entry. For this purpose, a literature review on the topic has first been performed, then some approaches for heat-load calculation have been drawn.

10.1. State of the art

The existing literature regarding thermal loads for a Jovian atmospheric entry has been reviewed here. The main goal was to find viable approaches for calculating the incident heat fluxes acting on a vehicle traveling into Jupiter's atmosphere. The majority of the findings is related in some way to the Galileo mission, whose entry probe entered Jupiter's atmosphere on December 7, 1995.

Also, all the available flight data related to this Jovian entry is related to the Galileo mission [12], which had been the first and only one of its kind to feature an entry into the Jovian atmosphere.

10.1.1. Heatshields

For planetary entry trajectories, the heatshield is the driving part of the Thermal Protection Subsystem (TPS), accounting for the majority of the TPS mass. For steep entries at gas giants, however, special heatshields need to be designed, since the environment there is substantially different from an atmospheric entry performed on an inner planet.

Here, a description of the Galileo mission heritage is given, together with some remarks on recent developments on the topic.

Galileo mission heritage

The Galileo mission was a first of its kind, featuring an entry probe entering Jupiter's atmosphere. For such purpose, an adequate heatshield had to be designed, and some of its data is presented by Milos et al. [14], where they also analyze the ablation data from the flown trajectory. They provide valuable information on the materials used for its heatshield. Tabulated data for c_p and k_v of carbon phenolic and phenolic nylon is provided.

New developments

A new heatshield for atmospheric entry at gas giants has recently been designed by NASA, named Heatshield for Extreme Entry Environments Technology (HEEET) [40]. This heatshield is capable of mass savings above 40%, compared to standard carbon-phenolic heatshields such as Galileo's and its technological readiness is at level 6, meaning it just needs to undergo a flight demonstration. HEEET's outer layer consists of a fine, dense weave using carbon yarns, whereas the inner layer is a low-density, thermally insulating weave consisting of a special yarn that blends together carbon and phenolic materials.

10.1.2. Giant planets entry studies

Studies on heat loads for entry trajectories at giant planets have been mainly conducted during the 60s-70s in preparation for what would have become the Galileo mission. All this work consists hence of the foundation upon which the Galileo mission, and its pre-flight studies, relied.

Thermal loads

Many ways for effectively and efficiently computing thermal loads have been studied, providing equations that could be used in simulations of an entry trajectory.

Sutton and Graves Jr [44] study an equation for arbitrary gas mixtures that calculates the stagnation point convective heat flux. It can thus be adapted to Jupiter, accounting for the H-He ratio of the gas mixture.

Zoby et al. [45] provide approximate solutions for inviscid, radiating flows about blunt probes entering atmospheres consisting of hydrogen and helium. It is a fast way of assessing the heat fluxes, which would be suitable for optimization processes where batches of simulations have to be run.

Entry simulations

The first attempts at simulating a Jupiter entry had the main objective of assessing the magnitude of the thermal loads. Their importance determined the heatshield sizing, thus an accurate calculation that accounted for the most effects had to be carried out.

The dominant uncertainty factor associated with the heat shield recession calculations, fundamental for heatshield sizing, was the radiation absorption within the ablation layer, which was not well known at the time. Consequently, the evaluation of the convective and radiative blockage due to ablation vapors was a major issue [12]. What follows are two studies whose major aim was to effectively assess the importance of such an effect.

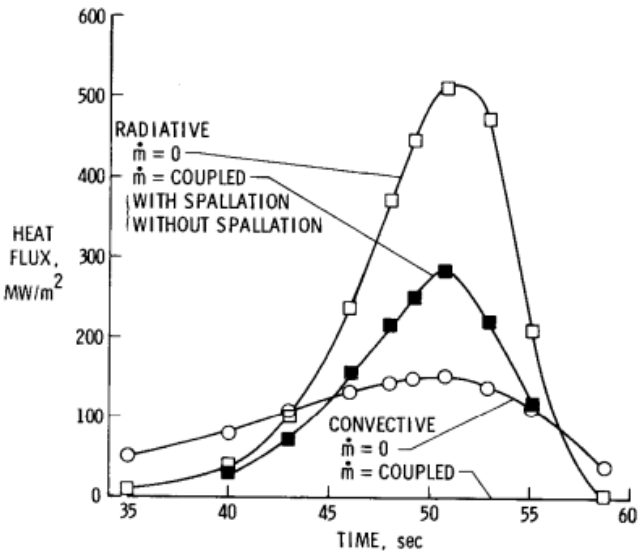

Figure 10.1: Stagnation point heat fluxes with ($\dot{m} \neq 0$) and without ($\dot{m} = 0$) coupled ablation injection [46, Figure 16]. Noteworthy is the coupled convective heat flux, which becomes almost negligible when considering ablation injection.

Moss J. N. [47] study the radiative blockage due to ablation injection for a Jupiter entry. Three entry trajectories are simulated. They account for variations in probe configuration, atmospheric gas composition, and entry conditions. Based on their assumptions, it results that ablation had a significant role in blocking the incident heat fluxes, similar results as those shown in Figure 10.1. The results are given in the form of tabulated data in which flight parameters, wall conditions, and heat fluxes are present for each case.

Moss and C. Bolz [48] performed a study focused on defining the heating environment during entry and on determining the effectiveness of coupled ablation injection in reducing the surface heating rate. They provide tabulated data on incident heat fluxes and on wall conditions for pressure and temperature. This is a pre-flight study, and, as had been seen with the Galileo entry, the effectiveness of ablation injection turned out to have been underdetermined at the stagnation point and overdetermined at the frustrum.

10.1.3. Galileo probe atmospheric entry

Following the previous work, the Galileo mission was conceived and flown. As already presented in Chapter 4, the part considered in this project is the probe entry.

Time, s	Altitude, km	V_∞ km/s	ρ_∞, kg/m^3	p_s, atm	ρ_s/ρ_∞	T_s, K	δ_s, cm	q_C, MW/m^2	q_R, MW/m^2
35.00	215.3	47.65	1.35e-5	0.28	13.64	14472	1.23	50	8
40.00	184.5	47.14	4.22e-5	0.85	12.75	15497	1.29	80	40
43.00	166.6	46.38	8.47e-5	1.65	12.16	16054	1.35	107	101
46.00	149.0	44.89	1.72e-4	3.12	11.53	16437	1.55	131	237
48.00	138.0	43.25	2.72e-4	4.56	11.07	16461	1.73	141	370
49.13	132.2	42.06	3.47e-4	5.50	10.82	16357	1.86	150	446
50.78	123.9	39.77	4.99e-4	7.04	10.34	15989	2.00	154	512
52.86	114.1	36.00	7.66e-4	8.79	9.60	15027	2.39	138	474
55.06	105.1	31.08	1.16e-3	9.77	8.76	13085	2.71	111	210
58.75	93.0	22.24	2.03e-3	9.11	12.41	5493	2.04	39	0

Table 10.1: Flight data and radiative and convective wall heat fluxes at radiation pulse phase [46, Table 4]. The probe mass in this simulation has been set to 335 kg. Subscript s indicates surface conditions, whereas ∞ indicates free-stream flow.

The work related to the Galileo mission includes the pre-flight studies performed prior to the entry, but much of the literature has sparked after the mission had flown. The attempts at reconstructing the heat loads are presented here.

Pre-flight studies

Although they could not rely on direct mission data, pre-flight studies are an important part of the literature about the Galileo entry, and their results are still valuable as a starting point to model the heat fluxes. As proof of this, they can be adjusted with later discoveries to match the reconstructed heat fluxes of the trajectories. The two most complete pre-flight studies are presented here.

Moss and Simmonds [46] study the forebody flowfield solutions for Jupiter entry conditions, where the ablation injection rate is coupled with the surface heating rate. They report radiative and convective wall heat fluxes at 100-200 km altitudes for the Galileo mission. Report data of interest is shown in Table 10.1 and the visual trends are presented in Figure 10.1. It is still a pre-flight study, but they account for most effects and, together with the work of Haas and Milos [49], they represent the culmination of the pre-flight literature on the topic.

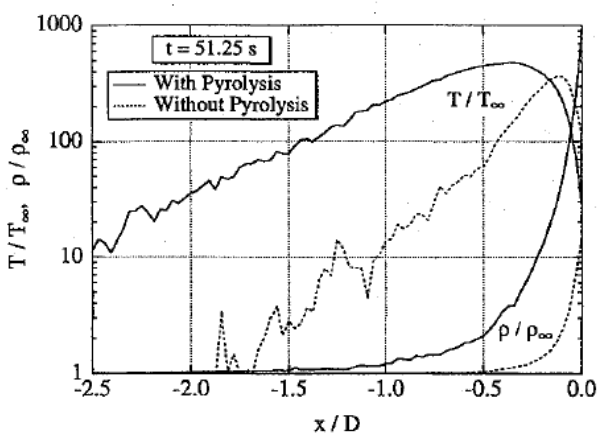

Figure 10.2: Profiles of flow temperature and density along the stagnation streamline. Results are shown both with and without accounting for pyrolysis [49, Figure 9]. D is the probe diameter and x is the independent variable expressing the distance from the stagnation point along the streamline. These results are plotted at time $t = 51.25$ s relative to the reference time used in Table 10.2.

Flowfield properties and aerodynamics are computed with a direct Monte Carlo simulation in the rarefield flow regime in Haas and Milos [49]. Simulation results, employing a simple radiative equilibrium surface model, indicate that the drag coefficient, C_D, varies from 2.1 at the free-molecule limit down to 1.6 when approaching the near-continuum transition regime ($Re_\infty = 1000$). They perform different simulations for different values of the accommodation coefficient A, which relates to how flow particles collide with the probe heatshield. From these simulations, they report flow parameters and thermal loads at altitudes between 350-750 km. See Table 10.2 and 10.3. Moreover, in Figure 10.2 they show how the particle density approaches near-continuum flow when close to the probe incident surface, and the temperature greatly increases, suggesting the formation of a bow-shock-like structure.

Time, s	Altitude, km	Re	M	Kn	T, K	ρ, kg/m^3
0.00	735.00	0.10	31.47	415.59	425.0	2.024e-11
19.00	604.00	1.03	34.15	43.01	360.5	1.896e-10
33.50	506.00	8.69	37.20	5.55	303.2	1.422e-09
41.00	453.00	34.01	39.61	1.51	267.0	5.100e-09
46.40	416.00	103.41	41.86	0.53	238.7	1.435e-08
51.25	382.00	322.47	44.58	0.18	210.0	4.097e-08
55.50	353.00	926.15	46.35	0.07	194.0	1.114e-07

Table 10.2: Galileo probe entry simulation conditions [49, Table 1].

Re	A	C_D	q_{nose}, W/m^2	T_{nose}, K
0.10	0.75	2.060	766	358.0
1.03	0.75	2.048	6495	602.4
8.69	0.75	2.024	48728	998.1
34.01	0.75	1.970	168523	1365.1
103.41	0.75	1.896	448881	1737.4
322.47	0.75	1.777	1201362	2236.4
926.15	0.75	1.629	2980082	2798.3
0.10	0.50	2.061	474	318.8
8.69	0.50	2.046	32564	909.9
103.41	0.50	1.934	309602	1580.3
926.15	0.50	1.628	2085700	2545.3
0.10	0.90	2.043	848	366.8
8.69	0.90	2.008	57941	1050.3
103.41	0.90	1.864	528677	1826.8
926.15	0.90	1.648	3559079	2931.1
34.01	pyrol	1.959	166779	482.2
103.41	pyrol	1.969	342187	642.1
322.47	pyrol	1.694	375325	896.8
926.15	pyrol	1.411	710552	1132.5

Table 10.3: Galileo probe entry simulation results at stagnation point [49, Table 2]. Simulations have been run for different values of A. 'pyrol' stands for pyrolisis, that is when ablation occurs.

Post-flight reconstruction

The success of the Galileo mission and the discrepancy of the mission data with the previous models sparked a series of studies aimed at understanding the nature of this inconsistency. The nose tip of the probe, approximately where the stagnation point was located, experienced a much lower ablation than expected, whereas the probe frustrum experienced a heatshield recession significantly higher than what the models predicted [12] [14]. The following papers investigate the nature of such discrepancies.

Matsuyama et al. [50] and Matsuyama et al. [51] analyze the Galileo trajectory and try to reproduce the overall heat shield recession experienced by the probe. They investigate the case with radiation only [50], then they include the effects of ablation [51]. The altitude range is between 100-200 km, thus it represents the part with continuum flow, far from the free-molecular regime. Remarkable is their approach to the probe mass loss modelling, where an energy-based approach has been followed.

Time, s	Altitude, km	Ablation rate, kg/m^2·s	Spallation rate, kg/m^2·s	q_R boundary-layer edge, kW/cm^2	q_R wall, kW/cm^2	q_C wall, kW/cm^2
40.35	190	0.473	0	3.713	2.031	0.4179
43.79	170	1.128	0	8.369	3.707	0.2283
47.36	150	2.943	0	19.42	8.120	0.1562
49.21	140	4.459	0	28.34	11.75	0.1537
51.16	130	5.672	0.0120	34.38	14.68	0.1375
53.23	120	5.749	0.0376	30.18	14.88	0.1151
55.52	110	5.664	0.0174	25.01	14.68	0.1568
58.19	100	1.604	0	5.310	4.743	0.7707

Table 10.4: Steady-state solutions for the Galileo probe at the stagnation point [37, Table 4].

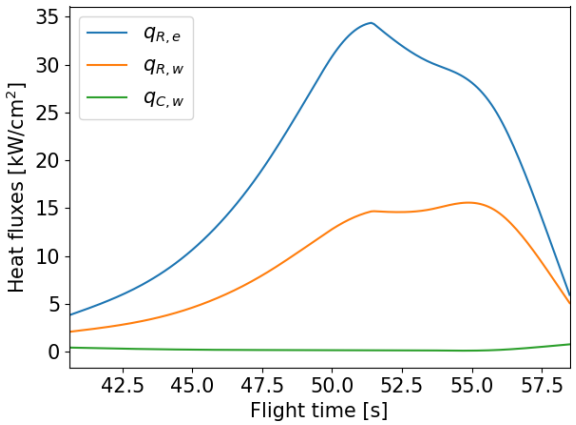

Figure 10.3: Park q_R and q_C trends from data of Table 10.4. The data points have been interpolated using a Lagrange 8th-order interpolator scheme. Subscripts 'e' and 'w' stand respectively for boundary-layer edge and wall conditions.

Park [37] analyze the heating/ablating environment of the Galileo probe, with a focus on the stagnation-point region. They run simulations for altitudes between 100-200 km, including the effects of ablation and spallation. This study is limited to stagnation point results, but it has been capable of reaching the closest match between flight and simulation data for calculating the heat fluxes in that region. The steady-state solutions for the Galileo probe at the stagnation point are present in Table 10.4. Apart from ablation and spallation rates, they provide radiative and convective heat fluxes, with the radiative heat flux calculated also at the boundary layer edge. The convective heat flux shows a different behavior from the rest, which could seem unexpected, but this has likely to do with the effect of blockage from ablation vapors, which was the strongest during the radiation pulse. The convective heat flux can be seen to increase at the end because that is when the blockage effect becomes weaker. Figure 10.3 shows the trend of q_R and q_C, the radiative and convective heat fluxes. Data from Park [37] is then particularly suited for V & V purposes since it is the most detailed study of the heat fluxes at the stagnation point performed with Galileo's in-flight data [52].

Milos et al. [14] study the ablation and temperature data from the Galileo entry. As previously presented, they provide info on the heatshield properties and some sensor data. They also estimate the peak heat flux and heat load experienced by the vehicle.

Mass loss models

Accurately describing the behavior of the mass loss experienced by the probe is critical for an accurate estimation of the blockage effect from the ablation vapors. In fact, many approaches are available in the existing literature, and here the two most promising ones have been selected and presented here.

A data-regression approach is proposed by Seiff et al. [53], where they suggest the formula

$$\dot{m} = k\,\rho\,V^{6.9} \tag{10.1}$$

where k is a constant, ρ is the atmospheric density, and V is the airspeed. According to them it provides a good approximation of the mass loss rate experienced by the probe during entry. The parameter k however was not given, thus it has been estimated by fitting reconstructed flight data from Seiff et al. [13] with that formula. A least-squares algorithm has been used, returning a value of $k = 2.765998e-28$. The fitted curve is presented in Figure 10.4 and can be seen to match the flight data quite accurately.

Moreover, a similar curve is also present in Figure 12 of Seiff et al. [53], providing additional proof of the correctness of the calculation.

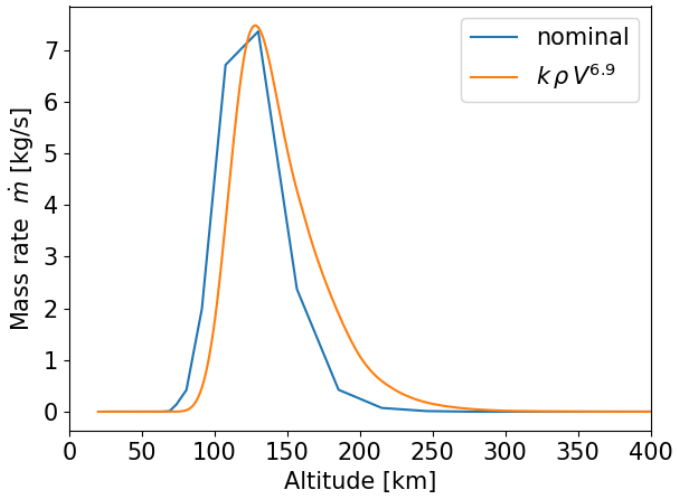

Figure 10.4: Mass loss rate (absolute value) calculated following the law presented in Seiff et al. [13]. Note that here the mass loss rate has been plotted with respect to the altitude.

An energy-based mass loss model is instead proposed by Matsuyama et al. [51], where the mass injection rate ($\dot{m}$) is indeed determined from an energy balance at the wall, given by

$$\dot{m} = -\frac{q_{C,w} + q_{R,w}}{\Delta H_a} \tag{10.2}$$

where ΔH_a is the heat of ablation. Quasi-steady ablation is assumed, and the wall temperature is assumed to coincide with the sublimation temperature of the ablator. The sublimation temperature (T_{sub}) and the heat of ablation (ΔH_a) for a carbon-phenolic ablator are calculated with

$$T_{\text{sub}} = 3797.0 + 342.0 \log p_w + 30.0(\log p_w)^2 \tag{10.3}$$

$$\Delta H_a = 28.0 - 1.375 \log p_w + 27.2(\log p_w)^2 \tag{10.4}$$

where p_w is the wall pressure in atmospheres. The mass composition of the carbon-phenolic ablator is chosen to closely match that one of the probe's heatshield, thus it is assumed to be 92% carbon, 6% oxygen, and 2% hydrogen. Finally, the surface recession rate can be calculated by using $\Delta s = \dot{m}/\rho_v$ where the density of the heat shield material is given by $\rho_v = 1448\, kg/m^3$.

However, a challenge posed by this energy-based method is finding a way of calculating the pressure at the surface of the capsule, which is far from trivial.

10.1.4. Tools for thermal loads evaluation

As shown, quantifying the thermal loads for a Galileo-like entry trajectory at a gaseous planet is rather complicated. This chapter aims at collecting another set of more generic tools that can aid the calculation process. Some are presented also as already tailored for an aerocapture trajectory at Jupiter, whereas some others are just more general techniques that can be adapted to a Jupiter entry.

Correlations by data regression

Tauber and Sutton [54] show a powerful yet simple technique for approximating the radiative heating by using entry data for cases at Earth and Mars. It consists of an equation fitted to flight data to effectively measure the heat fluxes during re-entry. However, the entry velocity range for the formulation to be valid is at most in the order of 10 km/s, thus not applicable for a Jupiter entry. However, the general technique, which makes use of the Chapman equation [55], can still be adapted to derive a formulation for the radiative heat for Jupiter. The Chapman equation is the following:

$$q = c_1 \sqrt{\frac{\rho}{R_N}} V^m \left(1 - \frac{T_w}{T_{w,ad}}\right) \tag{10.5}$$

where q is the heat flux, ρ is the atmospheric density, R_N is the vehicle nose radius, V is the airspeed, T_w is the wall temperature, and $T_{w,ad}$ is the adiabatic wall temperature ($= T_\infty$). The free parameters are c_1 and m. The term $(1 - T_w/T_{w,ad})$[1] is often regarded as the hot-wall correction since in the cold-wall approximation, especially valid for hypersonic flight, it usually happens that $T_w/T_{w,ad} \approx 0$.

Another more general formulation of the Chapman equation allows for more degrees of freedom when curve fitting, and is more suitable for this project. Such equation is the following:

$$q = c_1 \frac{\rho^n}{\sqrt{R_N}} V^m \tag{10.6}$$

where the free parameters are c_1, m, and n, and R_N is the nose radius, ρ is the density, and V is the airspeed. The hot-wall correction has been neglected here since non-adiabatic effects usually get considered in a second moment when using this form of the equation.

Ritter et al. [56] derive two correlations for fluxes based on Galileo mission data. One is for the convective heat flux, and the other one is for the radiative heat flux. They validate them and they turn out to be in good agreement with the Galileo flight data if non-adiabatic effects and blockage from ablation vapors are taken into account. Such correlations will be presented in section 10.2.

Jupiter Atmospheric Entry code

Park and Tauber [57] talk about a simple yet accurate model to predict the turbulent convective heating rate, which explains part of the Galileo heat shield recession. Their results refer to the work of Tauber et al. [15], where a fast code for a Jupiter entry analysis is discussed and its equations are provided. The model would take into account both the incident convective and radiative heat, then it would apply some derived correlations that account for the non-adiabatic effects of radiation and for the blockage effect due to ablation vapors. The coefficients for those correlations are however left undetermined. They can be found from Reynier [58]. They show how the code works, and how it can be implemented. Much information is taken from the work of Tauber and Wakefield [59], where the heating environment at Jupiter entry is investigated, and three entry probes for Jupiter are compared.

Preliminary studies on aerocapture at Jupiter

Aso et al. [60] conduct a preliminary study on the Jupiter aerocapture mission type, one of the few of its kind. They calculate launch windows, set a corridor width for the aerocapture based on eccentricity and strict aerothermal loads constraints, plot altitude density, velocity, and deceleration, and perform a numerical study of the heat loads.

10.2. Stagnation point heat loads calculation

In a zero-angle-of-attack configuration, the stagnation point is the region where the most intense thermal loads act on the vehicle, hence it is the most critical part of a heatshield for this kind of atmospheric entry. This configuration closely matches the Galileo mission's case, but can be applied to an aerocapture mission as well. A first-order estimate of the size of a heatshield can be done with just the thermal loads at the stagnation point. For this reason, the focus will be primarily put on the stagnation point region for calculating both the convective and radiative heat fluxes (respectively, q_C and q_R). For that, the results of section 10.1 on thermal loads are used, and some viable approaches have been drawn. Such approaches to calculating heat fluxes are the following:

1. Gather heat flux data from Haas and Milos [49] and Moss and Simmonds [46] (Table 10.1, 10.2, 10.3) and correlate it with equations from Tauber and Sutton [54]
2. Use the code developed by Tauber et al. [15]
3. Use the correlation equations derived by Ritter et al. [56]

[1] The fact that $T_w/T_{w,ad}$ is written, instead of $h_w/h_{w,ad}$ (the enthalpy ratio) assumes that the pressure gradient between the bow shock and the vehicle surface is constant so that $(T_{w,ad} - T_w) = c_p\,(h_{w,ad} - h_w)$.

It turns out that such approaches have to be integrated within each other, since each of them can contribute only in a partial way to the heat loads calculation. Only the joint use of all approaches can hence give satisfying results.

Once the heat fluxes are calculated, the total heat load Q can be derived by a simple time integration procedure. This value has been seen to be strongly correlated with the TPS mass fraction of previously flown space missions, hence its calculation is crucial for first-order TPS sizing.

10.2.1. Vehicle heating environment

An aerocapture mission would most likely fly above altitudes of 200-250 km, thus for the majority of its trajectory the atmosphere the spacecraft encounters is very thin, so there is free molecular/transitional flow, and only in a few cases and for a short time period the continuum-flow regime is encountered. It can be shown with data from Seiff et al. [13] where the Knudsen number (Kn) decreases with altitude and reaches a value around 0.1 slightly above 300 km altitude. Free molecular flow occurs when Kn > 10, whereas transitional flow occurs when 10 > Kn > 0.1, thus for the majority of the trajectory the spacecraft would fly in altitudes corresponding to free molecular/transitional flow.

At the free molecular flow regime, with very high velocities w.r.t. air (tens of km/s), a bow-shock region can however still form around the spacecraft, allowing for heat convection to occur. This happens because the speed is 50 times as much as the thermal speed of molecules, so large it can compress the molecular flow to transient/continuum fluid, eventually forming a bow-shock-like structure [60].

It will later be shown that convection is far greater than radiation for shallow entries such as those for aerocapture, and radiation becomes dominant only for deep dives into the atmosphere, such as Galileo's, where gas molecules ionization happens at a larger scale.

Non-adiabatic effects for the radiative heat flux

At hypersonic speeds, it usually happens that the hot wall correction term gets neglected, thus the cold-wall approximation is implicitly used. This works well because, as explained before, the temperature of the compressed fluid is far greater that the vehicle surface temperature. However, when radiative heat fluxes become important, non-adiabatic effects can in some cases become far from negligible [59]. This is the case for the Galileo entry, where such effects had a strong influence on the reduction of the incident radiative heat flux. How their behavior has been modeled will be shown in the following paragraphs.

Heat flux blockage due to ablation vapors

The blockage effect due to the ablation products can be rather important in case of strong ablation, and, as a consequence, it can drastically reduce the incident heat fluxes on the vehicle. This applies both to radiation and convection.

The assessment of its magnitude, however, is far from trivial. Its modeling is indeed rather difficult since it strongly depends on the interacting chemical species (from the atmosphere and the ablating material) and on the laminar or turbulent nature of the boundary layer. Ablation injection of vapors greatly encourages the transition from laminar to turbulent, as post-flight studies have observed [37]. Pre-flight studies carefully evaluated the impact of this blockage effect, however, they did not account for this induced turbulence. This has been the cause of their underestimation of the cone frustum recession. Turbulence indeed encourages the exchange of heat, making the boundary layer more "transparent" to incident heat fluxes [58].

A useful correlation to model the impact of this effect is derived by Brewer and Brant [61]. It will be later presented when addressing the blockage effect on the convective and radiative heat fluxes.

10.2.2. Convective heat flux

Due to the importance of the convective heat flux for aerocapture at Jupiter, all three approaches presented at the beginning have been considered for the heat flux calculation.

Data regression

For the convective heat flux, the first approach consists of fitting Equation 10.6, the Chapman equation in its generic formulation to some Galileo convective heat flux data. The convective heat flux data as said before is obtained from Haas and Milos [49] and Balakrishnan and Nicolet [62] (Table 10.1, 10.2,

10.3), the two most complete pre-flight studies of the Galileo trajectory [12]. The following expression can then be obtained:

$$q_{C_{B=0}} = 4.13377754 \frac{1}{\sqrt{R_N}} \rho^{0.51467325} V^{5.66475942} \tag{10.7}$$

where $q_{C_{B=0}}$ is the convective heat flux for non-ablating conditions [kW/m^2], R_N is the nose radius [m], ρ is the density [kg/m^3], and V is the airspeed [km/s]. Note that the hot-wall correction term has been neglected due to the hypersonic nature of the trajectory. A least-squares algorithm has been used, and it has been fed with simulated flight data comprehending altitudes between 750 and 150 km. Input values have been scaled with respect to their maximum value, to allow for a better convergence of the interpolating algorithm. Such values are presented in Table 10.5, and they must be used as scaling parameters when using Equation 10.7. The result of such curve fit is shown in Figure 10.5. This approach however suffers from the high uncertainty of the convective blockage factor, which was better understood only after studying the Galileo in-flight data.

Variable Name	Scaling Value
R_N	1.58227848e+00
ρ	4.92610837e+02
V	2.09863589e-02
$q_{C_{B=0}}$	6.49350649e-06

Table 10.5: Scaling values for variables of Equation 10.7. Values such as 6.49e-06 are to be read as $6.49 \cdot 10^{-6}$.

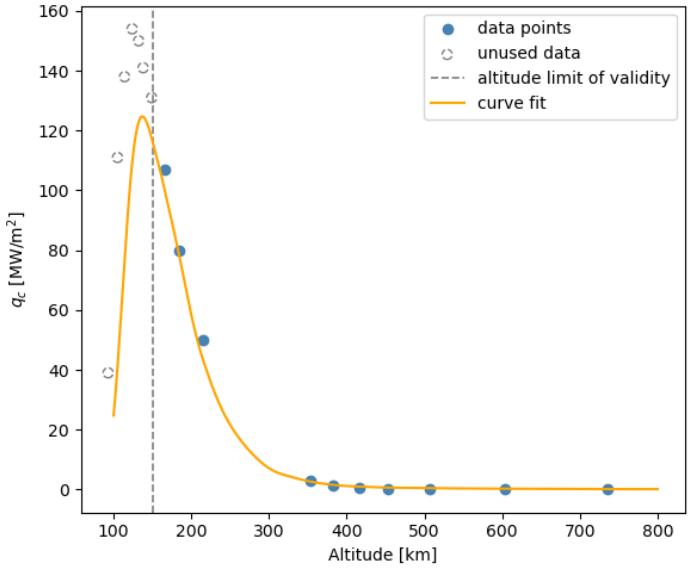

Figure 10.5: Curve fit for the convective heat flux $q_{C_{B=0}}$. As shown, not all the available data points have been used. This choice has been made to allow for a more precise interpolation at higher altitudes, at the cost of constraining the range of applicability to altitudes higher than 150 km. The 150 km limit is anyway below the desirable minimum altitudes for aerocapture entries. The gap in data points present at 200-350 km is due to the fact that data has been taken from two different works; one investigating high altitudes, above 350 km, and the other investigating low altitudes, below 200 km. No additional data could be found for the intermediate range to fill this gap.

Jupiter code

The second approach would use the code developed by Tauber et al. [15], but much of the necessary information for the code set-up could not be collected, thus making this way unfeasible on its own. It has been regarded more as a general guideline on how to set up the heat loads model.

Usage of existing correlations

The third approach consists of using Ritter et al. [56] correlation for the convective heat flux, which is the following:

$$q_{C_{B=0}} = 2004.2526 * \frac{1}{\sqrt{\frac{2*R_N}{0.6091}}} * \left(\frac{\rho}{1.22522}\right)^{0.4334441} * \left(\frac{V}{3048}\right)^{2.9978867} \tag{10.8}$$

where $q_{C_{B=0}}$ is the convective heat flux for non-ablating conditions [kW/m^2], R_N is the nose radius [m], ρ is the density [kg/m^3], and V is the airspeed [m/s]. This equation already comes with variable scaling integrated into it.

Alternative to this, Girija et al. [38] provided a similar but simpler equation that results in similar outcomes. This is their expression for the ablation-free convective heat flux:

$$q_{C_{B=0}} = C_{\text{hfx}} \frac{\rho}{\sqrt{R_N}} V^3 \qquad C_{\text{hfx}} = 0.6556E-4 \tag{10.9}$$

where C_{hfx} is a constant determined by the planet's atmospheric composition, Jupiter in this case, ρ_∞ is the free stream atmospheric density [kg/m^3], R_N is the vehicle's effective nose radius [m], and V is the free stream velocity in [m/s]. Lastly, $q_{C_{B=0}}$ is the ablation-free ($B = 0$) convective heat flux and has units of W/m^2.

Convective blockage

Correlations for convection blockage are empirical and based on experimental or computational data valid only for Jupiter entry conditions and carbon–phenolic material [58]. The following is a material-dependent correlation derived by Brewer and Brant [61]:

$$\psi_{C_T} = \left[\frac{2.344}{B}\left(\sqrt{B+1}-1\right)\right]^{1.063} \tag{10.10}$$

where the turbulent convective blockage factor, $\psi_{C_T} = q_C/q_{C_{B=0}}$, is represented as a function of the non-dimensional blowing coefficient B. The correlation can be seen in Figure 10.6.

What comes next is calculating the blowing parameter, or blowing rate, B. It is the driving point of the blockage effect. The blowing term represents the gaseous diffusion of the decomposing material into the boundary layer causing a thickening of the boundary layer and a reduction of the temperature gradient [58]. According to Reynier [58], the blowing parameter can be described as

$$B = \frac{\dot{m}\, c_p\, (T_{w,ad} - T_w)}{q_{C_{B=0}}} \tag{10.11}$$

where c_p is the specific heat at constant pressure of the gas mixture and $\dot{m}$ is the mass injection rate. Equation 10.11 can then be reworked to highlight the ratio between the two temperatures so that it becomes

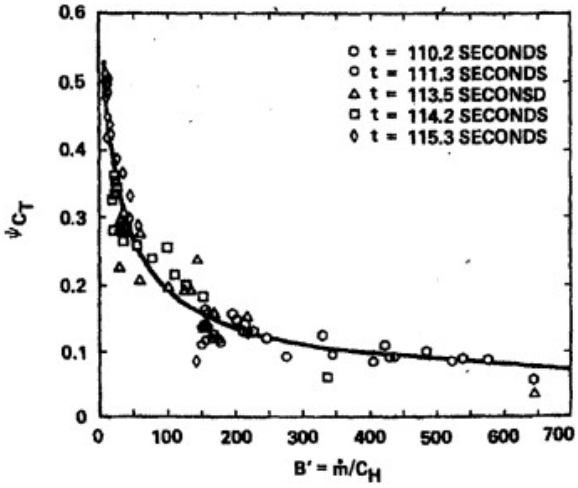

Figure 10.6: Convective blockage for turbulent boundary-layers [61]. Note that $B' = B$.

$$B = \frac{\dot{m}\, c_p\, T_{w,ad}}{q_{C_{B=0}}}\left(1 - \frac{T_w}{T_{w,ad}}\right) \tag{10.12}$$

where $T_w/T_{w,ad}$ can be neglected for hypersonic flow. According to Mooij [6], $T_{w,ad}$ can be described as

$$T_{w,ad} \approx \frac{V_\infty^2}{2c_{p,\infty}} \tag{10.13}$$

at the stagnation point and for a hypersonic flow regime, since it is assumed that $T_{w,ad} \gg T_\infty$. The resulting expression for the blowing coefficient then becomes:

$$B = \frac{\dot{m} V_\infty^2}{2\, q_{C_{B=0}}} \tag{10.14}$$

assuming $c_p \approx c_{p,\infty}$. The most critical factor to model is the mass injection rate $\dot{m}$. Two different approaches for its modeling come from a data-regression model (Equation 10.1) and an energy-based approach (Equation 10.2).

10.2.3. Radiative heat flux

For what concerns the radiative heat flux, the third approach [56] already gives a good estimate of its magnitude, as it will be later shown, thus there was no need to pursue other ways. The correlation for the radiative heat flux is the following:

$$q_{R_{\text{AD},B=0}} = 9.7632379^{-40} * (2 * R_N)^{-0.17905} * (\rho)^{1.763827469} * (V)^{10.993852} \tag{10.15}$$

where $q_{R_{\text{AD},B=0}}$ is the radiative heat flux without accounting for non-ablating conditions and non-adiabatic effects [kW/m^2], R_N is the nose radius [m], ρ is the density [kg/m^3], and V is the airspeed [m/s]. This equation again already comes with variable scaling integrated into it.

Non-adiabatic effects

Equation 10.15 alone, however, has to be corrected for non-adiabatic flow effects (also regarded as radiative cooling), which have an important role in a steep entry like the Galileo one [56]. The equation that approximated this effect is obtained from the work of Tauber and Wakefield [59], which adapted the Goulard equation to a Jupiter entry, and is the following:

$$\Gamma = \frac{4 q_{R_{\text{AD},B=0}}}{\rho_\infty V_\infty^3} \qquad q_{R_{B=0}} = \frac{q_{R_{\text{AD},B=0}}}{1 + 3\Gamma^{0.7}} \tag{10.16}$$

where Γ is the Goulard number (the radiation cooling parameter) and the heating rate $q_{R_{\text{AD},B=0}}$ has to be here provided in W/m^2 for the equation to work. Here, ablation is neglected ($\dot{m} = 0$, $B = 0$).

Radiation blockage

When ablation is taken into account, however, the incident radiative heat flux at the wall gets reduced even further. As said before, this has to do with the ablation vapors blocking part of the radiative heat flux from the probe. The greater the ablation, the larger the blockage.

The same empirical correlation used to model the blockage effect on the convective heat flux can be applied here as well. The radiation blockage effect would then be described by Equation 10.10 and 10.14, the equations for calculating the blockage factor $\psi_{R_T} = q_R / q_{R_{B=0}}$ and the blowing parameter B.

10.2.4. Total heat load and Peak heat flux

Total heat load and peak heat flux are two critical quantities that need to be considered when designing a TPS for an atmospheric entry mission. The calculation method for both of them, as well as a TPS-sizing method, are presented here.

Total heat load

The total heat load acting on the vehicle's wall, Q_w, is a crucial quantity that determines the size of a spacecraft's TPS. A correlation between the total heat load and the TPS mass fraction for previously flown missions has been derived by Wright et al. [63] and is shown in Figure 10.7. The correlation for the mass fraction is the following:

$$f_{\text{TPS}} = \frac{m_{\text{TPS}}}{m_{\text{vehicle}}} = \frac{0.091}{100} \left(\frac{Q_w}{10000}\right)^{0.51575} \tag{10.17}$$

where Q_w is in J/m^2, and an extra factor of 10^{-2} has been introduced to express the mass ratio f_{TPS} as a value ranging from 0 to 1, and not in percentage form.

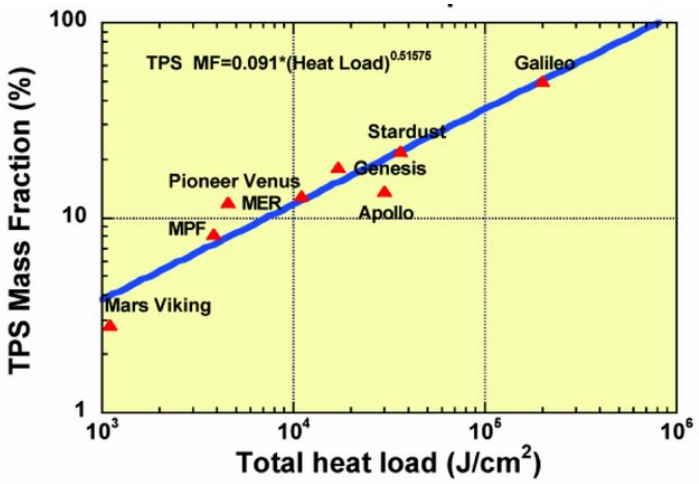

Figure 10.7: TPS mass fraction for prior NASA missions [63, Figure 1] Note that the Galileo probe experienced a total heat load of about 200 kJ/cm^2, which corresponds to a TPS mass fraction of about 50%.

This correlation, however, implies that the value of Q_w must be known. An effective way of calculating this quantity is by integrating the total incident heat flux on the vehicle's wall over the flight time, following this expression:

$$Q_w = \int_{t_0}^{t_f} q_w \, dt = \int_{t_0}^{t_f} (q_C + q_R) \, dt \tag{10.18}$$

where Q_w is the total wall heat load [J/m^2], q_w is the total wall heat flux [W/m^2], and t_0 and t_f are the atmospheric entry and exit epochs. For the accuracy required by the current work, the trapezoidal rule approximation for calculating the integral is more than sufficient. The integration errors that would be introduced have a limited influence on the value of Q_w, which as well would make the TPS mass fraction vary by a negligible value.

Peak heat flux

Alongside the total heat load, the peak heat flux is another crucial quantity that determines the type of heatshield that will be used. Different heatshields are composed of different materials, often interwoven in different ways, all characteristics that determine the maximum incident total heat flux that a given heatshield can sustain. Table 10.6 gives an overview of the maximum total heat flux sustainable by the currently available heatshields.

The calculation of the total heat flux is quite straightforward. It consists of taking the maximum value of the total incident wall heat flux along the trajectory.

Material Name	Manufacturer	Density, kg/m^3	Heat flux limit, W/cm^2
SLA-561V	Lockheed-Martin	256	$\sim$200
FM 5055 Carbon Phenolic	Fibercote	1450	>10,000
MX4926N Carbon Phenolic	Cytec (pre-preg), ATK, HITCO	1450	>10,000
PhenCarb-20,24,32	Applied Research Associates	320-512	$\sim$750
PICA (Phenolic Impregnated Carbon Ablator)	Fiber Materials, Inc. (FMI)	265	>1500
Avcoat 5026 (Apollo)	Textron Systems	513	$\sim$1000
ACC	Lockheed-Martin	1890	$\sim$1500
HEEET [40]	/	$\sim$1000	$\sim$5000

Table 10.6: Density and heat flux limit values of the most commonly used heatshield materials [55].

10.3. Observations

An effective method for calculating the heat loads acting on the vehicle is presented in this section.

Starting from an overview of the existing literature, with a focus on the Galileo mission, several approaches for calculating the incident heat fluxes on a Jupiter atmospheric entry have been found and derived.

As a result, correlations for calculating the incident convective and radiative heat fluxes (q_C and q_R) have been found, plus other effects acting on the entry environment have been considered. In particular, non-adiabatic effects on the radiative heat flux and the blockage of heat fluxes due to ablation have been regarded and modeled. Correlations of empirical nature, or theory-derived ones, describe such effects on the basis of trajectory parameters such as velocity and density. Important to mention is the model selected for approximating the mass injection rate $\dot{m}$. The data-regression model has been selected due to its simplicity and the fairly good results it can give, as it will be seen in Chapter 14.

Moreover, the derivation of the total heat load Q_w acting on the vehicle has been presented, which requires knowing the values of q_C and q_R.

Lastly, a way of correlating Q_w and the TPS mass fraction of a spacecraft has been found and presented.

11

Addition Of Flybys

This chapter assesses the problem of flybys, to see whether a pre- and/or post-aerocapture flyby(s) can be added.

11.1. Pre-aerocapture Flyby

Adding a flyby prior to aerocapture can help reduce the orbital energy. However, this approach poses serious constraints on orbit geometry. Although flybys at moons have been observed to reduce orbital energy by 20-35%, which is a considerable amount, it is not expected to sufficiently counterbalance the constraints on trajectory geometry that adding a flyby imposes. Moreover, it is worth noting that the aerocapture technique is more effective when it has more energy $\Delta\mathcal{E}$ to dissipate [26].

The maximum delta energy obtainable with flybys can be calculated using the following equation [2]:

$$\Delta\mathcal{E}_{\text{max}} = \frac{2V_t' V_{\infty_t}}{1 + V_{\infty_t}^2 / V_{c_{\text{surf}}}^2} \tag{11.1}$$

where V_t' represents the velocity of the moon, V_{∞_t} is the asymptotic incoming velocity, and $V_{c_{\text{surf}}}$ is the surface circular velocity of the moon. The results of this calculation for different moons are summarized in Table 11.1.

Moon	$\Delta\mathcal{E}_{\text{max}}$ (MJ/kg)
Io	4.695
Europa	2.756
Ganymede	4.719
Callisto	3.534

Table 11.1: Maximum Delta Energy Obtainable with Flybys for Various Moons. The initial orbital energy is 13.051 MJ/kg for an interplanetary arrival velocity of 5.6 km/s (based on a hypothetical Hohmann transfer).

In conclusion, pre-aerocapture flybys will **not** be considered on this study because the constraints that adding a flyby poses are not properly counterbalanced. The energy reduction it gives just slightly helps reducing the loads in the aerocapture phase, which however performs better when required to achieve a higher $\mathcal{E}_{\text{max}}$.

Moreover, the additional complexity that adding a pre-aerocapture flyby would have posed, would have been in conflict with the time constraints set for the thesis project. That is why it is left as a recommendation

11.2. Post-aerocapture Flyby

A post-aerocapture flyby would aim at changing the orbital energy in such a way that the pericenter of the orbit gets raised. In this case, the delta energy amounts are significant enough for a post-aerocapture flyby to be considered in the simulation. Furthermore, adding only one flyby does not

impose as strict constraints as adding two, thus the benefits of one post-aerocapture flyby **could** be investigated.

The results of the maximum delta energy obtainable with post-aerocapture flybys for different moons are summarized in the table below:

Moon	$\Delta\mathcal{E}_{\text{max}}$ (MJ/kg)
Io	4.813
Europa	2.858
Ganymede	4.990
Callisto	3.857

Table 11.2: Maximum Delta Energy Obtainable with Post-Aerocapture Flybys for Various Moons. The orbital energy post-aerocapture of the reference orbit is -4.623 MJ/kg, obtained with a 2.5 deg entry flight path angle aerocapture.

Table 11.2 provides insights on the maximum delta energy obtainable through post-aerocapture flybys for the moons Io, Europa, Ganymede, and Callisto, which is essential for mission planning and optimization. It can be seen how the $\Delta\mathcal{E}_{\text{max}}$ are on the same order of magnitude of the pre-aerocapture flyby, but now the energy of the closed orbit is much smaller than prior to aerocapture, making the effect of a flyby much greater in proportion.

A strict constraint that a post-aerocapture flyby poses comes from the short time of flight between the atmospheric exit and the moon flyby. The available window for corrective maneuvers could be too narrow or non-existing, depending on the moon at which the flyby would occur. That is the case because the less time is between the maneuver and the flyby, the more costly in delta-v terms the maneuver is going to be, potentially nullifying the benefits of a flyby over a conventional pericenter-raise burn.

Nevertheless, the potential of a post-aerocapture flyby is still being investigated, and a flyby-targeting method to intercept the moon at the right time and location is being developed.

11.3. Flyby Targeting Method

A complete flyby-targeting method has been developed, by using second-order equations from Engelsma and Mooij [64] and the full flyby description from [2] (see Chapter 12).
The flyby-targeting method calculates the entire trajectory based on the following parameters:

- interplanetary arrival velocity V_∞
- atmospheric entry flight path angle γ_E
- atmospheric entry altitude (set to 450 km by default)
- moon of flyby
- epoch of flyby
- flyby impact parameter B

from these parameters, the initial state and epoch of the trajectory are calculated with the following steps:

1. The orbital geometry of the arrival phase at Jupiter is determined thanks to the interplanetary arrival velocity V_∞ and atmospheric entry flight path angle γ_E. The initial distance from Jupiter is set at Jupiter's SoI, whereas the entry distance is set at 450 km altitude above the 1-bar level of Jupiter's atmosphere.
2. The aerocapture phase geometry and loads are calculated using the second-order equations for atmospheric entry available from Engelsma and Mooij [64] (see Chapter 12). They are particularly well suited for shallow-entry γ_E.
3. The post-aerocapture arc that leads to the flyby is calculated by using the atmospheric exit state and the flyby impact parameter B. The flyby formulation corresponds to that one expressed by Wakker [2]. The flyby epoch fixes the position of the moon from which the entire orbit follows. From here the initial epoch at which the orbit begins is backward calculated using the Keplerian time to true anomaly expressions.
4. The final orbit that results from the flyby is calculated, and its pericenter altitude is assessed.

5. From here on, the algorithm is capable of returning a state history of the analytical trajectory, with the required number of points, as well as the initial state and epoch for the numerical simulations.

Once the initial state and epoch of the trajectory are returned, they can be given to the numerical propagator, which will serve as a verification tool for testing the validity of the analytical expressions.

11.4. Method Verification

The method has been verified using a comprehensive numerical model, which incorporates Jupiter's point-mass gravity, the most advanced atmospheric model available, and the point-mass gravity of the moon during the flyby.

As discussed in Chapter 14, the outcomes are inconsistent due to various assumptions in the semi-analytical model that are not valid in the numerical context. Consequently, employing this method for flyby targeting would be exceedingly unreliable, yielding results unsuitable for both numerical simulations and actual mission scenarios.

Although the semi-analytical method remains promising if refined to better align with the numerical simulations, further improvements to the model exceed the current project's scope and time constraints. Therefore, this refinement is proposed as a future recommendation, given the method's demonstrated potential as an effective analytical targeting predictor.

11.5. Observations

The addition of a pre- and a post-aerocapture flyby has been considered. The pre-aerocapture flyby would have helped in reducing the loads in the atmospheric phase, but its contribution was too little in comparison to the geometry and time constraints it would put. The post-aerocapture flyby seemed to be a promising substitute for conventional pericenter-raise maneuvers, despite its strict geometrical and time constraints.

The targeting method implemented to harness the benefits of such flyby works well under its assumptions, but fails when verified with a more accurate numerical model that does not involve these assumptions, as will be shown in Chapter 14. Flyby targeting using this method would result in a far too unreliable approach: the results would not be applicable in a numerical simulation, let alone in a real mission scenario. The final problem will make use of a numerical model to compute the aerocapture, and the post-aerocapture flyby, while being a valuable addition to the research of the project, exceeds its time constraints and is not part of the main focus of the research question. Investigating the post-aerocapture flyby will be left as a future recommendation.

Moreover, the semi-analytical method should be refined to better match the numerical simulations, however further refinement of the model goes beyond the scope of the current project since it would also go beyond its time limitations. The refinement of the flyby-targeting algorithm is left as a future recommendation.

12

Problem Modeling

Various approaches have been considered for modeling a multi-flyby aerocapture trajectory at Jupiter. They are presented in the following sections.

12.1. Semi-analytical Modeling

The semi-analytical models used or developed for the project are presented here.

12.1.1. Lambert-targeting algorithms

The first attempt at modeling a multi-arc aerocapture trajectory at Jupiter concerned the usage of Lambert-targeting algorithms (also called Lambert targeters). They are algorithms whose scope is solving Lambert's problem. They had been selected because of their ease of usage and the flexibility given by the parameters of the problem. In the current project, a revisited formulation of Lambert's problem given by Izzo [65] has been used.

To compute a trajectory arc, the Lambert targeter in fact requires only the trajectory time of flight and the initial and final positions of the spacecraft. With just these quantities, and through a root-finding process, the algorithm is capable of calculating the respective full orbital arc.

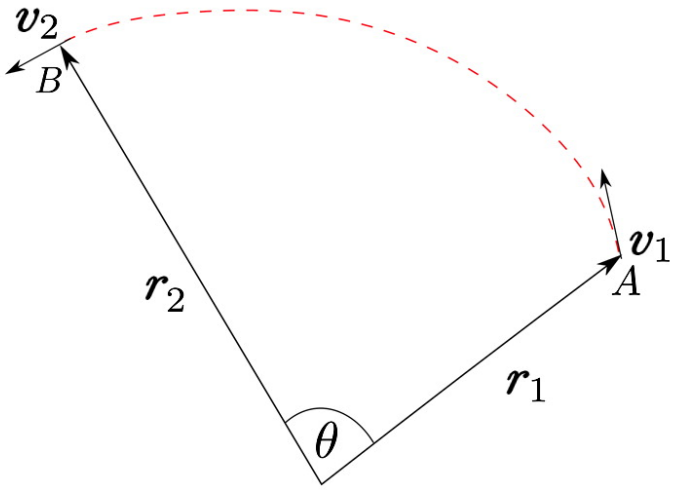

Figure 12.1: The general Lambert's problem geometry. By selecting the initial and final positions r_1 and r_2, and the time of flight of the arc, the entire trajectory positions and velocities from the initial and final positions can be reconstructed by means of a root-finding routine [66, Figure 2].

For what concerns multi-arc trajectories, namely those under consideration, using a Lambert targeter would make matching the position vectors at the trajectory nodes rather straightforward, as can be seen in Figure 12.1. The position vectors are indeed a parameter of the problem, thus they can be set accordingly so that the trajectory arcs are all matching.

For what concerns the boundary values for the velocity vectors, those are calculated only after solving Lambert's problem, thus they cannot be set to match beforehand. Matching the velocity vectors between arcs at the trajectory nodes would require an optimization process over the trajectory time of flight. The time of flight would be adjusted so that its value satisfies the boundary criteria both in between arcs but also at the trajectory boundaries.

Usually, multi-arc trajectories computed by means of Lambert targeters assume that impulsive burns at the trajectory nodes would bridge the gap between the mismatching velocity vectors. The optimization process would still be performed by varying the time of flight, but here the aim would be more at minimizing the total required delta-v, ideally bringing it to zero.

Since an optimization routine that would nullify the required delta-v for a multi-arc trajectory is likely to be an ill-posed problem, with not even the certainty of the existence of a solution, at least of an easy one to find, other approaches were considered.

The need for a tailored approach when calculating multi-arc trajectories resulted in the development of several semi-analytical models that will be depicted in the following sections.

12.1.2. Multi-flyby semi-analytical approaches

All the approaches assume the orbit remains within the same plane throughout the trajectory, which coincides with the moon's orbital plane. Hence, the flyby does not change the orbital plane and the orbital axis remains constant.

Instantaneous flyby at moon's center

Here other assumptions are made. It is assumed that the arrival position of the pre-flyby arc coincides with the moon's position and that the flyby happens at a single point in space. In this way, the position vectors of the two arcs would match at the flyby node.

The problem now requires a root-finding algorithm to find the pericenter altitude of the flyby that would allow the atmospheric entry conditions of choice. Info on the available root-finding algorithms is available in Chapter 7.

This approach is very straightforward in calculating a first estimate of a multi-arc trajectory. However, its applications are rather limited, since it is assumed that the flyby would happen at the moon's center of mass and with a fictitious flyby altitude.

Instantaneous flyby at a set pericenter distance

In this approach, it is instead assumed that the arrival position of the pre-flyby arc has to be at a set distance from the moon, but the flyby still happens instantaneously at a single point in space. In this way, the position vectors of the two arcs would still match at the flyby node by definition.

It is an in-between approximation between the first-order approach presented above and the full analytical flyby description.

The problem in this case still requires a root-finding algorithm for it to be solved, and the free parameter is still the flyby pericenter altitude. In this case, an additional equation has to be numerically solved to extract the β angle, a parameter of the flyby geometry that indicates the angle between the flyby pericenter direction and the direction opposite to the moon's velocity.

Complete analytical flyby description

In this approach, the flyby phase is treated with the full description presented in Chapter 2. This would mean that the position vectors of the two arcs would no longer match, but they would depend on the flyby's initial and final conditions. The flyby would no longer happen instantaneously, and the position change of the moon between the start and end epochs of the flyby would be taken into account as well.

The result is a rather accurate representation of the analytically computed orbit. The computation is, however, less straightforward. As the free parameter, the angle the spacecraft arriving at the moon forms with the moon's velocity vector is taken. It will be called the Σ angle. The set of equations will be solved by finding the right value of such Σ angle that satisfies both the initial and final conditions of the approach trajectory.

12.1.3. Aerocapture semi-analytical approximations

Two semi-analytical approaches that approximate the aerocapture phase were selected. They are first- and second-order approximations of the atmospheric entry equations. The first-order approximation

works best for steep entries, whereas the second-order one performs better at shallow entry flight path angles.

First-order equations

The following summarised derivation is taken from Mooij [6]. Refer to that for the full derivation starting from the equations of motion. The starting point for the derivation is given by a set of simplified and reworked equations of motion by Mooij [6]:

$$m\frac{dV}{dt} = -D - mg\sin\gamma \tag{12.1}$$

$$mV\frac{d\gamma}{dt} = L - mg\cos\gamma\left(1 - \frac{V^2}{V_c^2}\right) \tag{12.2}$$

$$\frac{dr}{dt} = \frac{dh}{dt} = V\sin\gamma \tag{12.3}$$

where m is the vehicle mass, V is the airspeed, g is the gravitational force of the planet, γ is the flight path angle, V_c is the local circular velocity for a given altitude h (or distance r), D, L are the drag and lift forces respectively.

A simple approximation of the motion for steep-entry trajectories can be obtained if the aerodynamic forces L and D are assumed to be large in relation to the mass terms in the equations of motion (12.1.3). With $D >> W$ and $L >> W$, it follows that

$$m\frac{dV}{dt} = -D \tag{12.4}$$

$$mV\frac{d\gamma}{dt} = L \tag{12.5}$$

$$\frac{dr}{dt} = \frac{dh}{dt} = V\sin\gamma \tag{12.6}$$

Dividing the above equations directly yields:

$$\frac{1}{V}\frac{dV}{d\gamma} = -\frac{D}{L} \tag{12.7}$$

Assuming L/D to be constant, we find for initial conditions V_E and γ_E (E stands for *Entry*)

$$\frac{V}{V_E} = e^{-\frac{\gamma - \gamma_E}{L/D}} \tag{12.8}$$

and since $\gamma_F = -\gamma_E$ (symmetric flight profile - F stands for *Exit*)

$$\frac{V_F}{V_E} = e^{\frac{2\gamma_E}{L/D}} \tag{12.9}$$

For an assumed exponential atmosphere, it follows with

$$\frac{p}{\rho} = RT = \frac{g}{\beta} \qquad \rho = \rho_0 e^{-h\beta} \tag{12.10}$$

where p and ρ are the atmospheric pressure and density, R is the gas constant for Jupiter's atmosphere, T is the atmospheric temperature, $\beta = 1/H_S$ with H_S being the scale height, and g is the gravitational acceleration, that

$$\cos\gamma - \cos\gamma_E = \frac{g}{2\beta}\frac{1}{\frac{W/S}{C_L}}(\rho - \rho_E) \tag{12.11}$$

so that the current free-stream density and altitude can be related to the flight path angle. Here W is the weight force, S is the cross-section area, and C_L is the lift coefficient.

Regarding the down-range, the following equation can be used

$$X = \frac{1}{\beta}\left[\gamma - \gamma_E + \cot\gamma'_E \ln\left(\frac{\tan\frac{\gamma'_E}{2} + \tan\frac{\gamma}{2}}{\tan\frac{\gamma'_E}{2} - \tan\frac{\gamma}{2}} \cdot \frac{\tan\frac{\gamma'_E}{2} - \tan\frac{\gamma_E}{2}}{\tan\frac{\gamma'_E}{2} + \tan\frac{\gamma_E}{2}}\right)\right] \tag{12.12}$$

where

$$\cos\gamma'_E = \cos\gamma_E - \frac{\rho_E\, g}{2\beta}\frac{C_L}{W/S} \tag{12.13}$$

By using Equations 12.8 and 12.11, the airspeed and the density the capsule experiences during entry can be calculated for any given flight path angle γ. Knowing that from the beginning to the end of an aerocapture trajectory γ monotonically increases from γ_E to γ_F, we can fully reconstruct the shape of the atmospheric entry with such means.

Second-order equations

This set of second-order equations is more suitable for shallow entries, with low flight path angles γ. The main downside of this set is that new dependent and independent variables and constants have to be introduced to non-dimensionalize the equations. The equations thus lose their intuitive nature and become increasingly complex. However, the non-dimensionalization and rewriting process is solely a mathematical operation, and the obtained equations of motion, when no approximations are added, still produce the exact results also obtained from standard equations of motion. The new non-dimensionalized values use symbols that may appear in other parts of the report, where they are used to indicate other quantities. These symbols have to be considered to take the meaning assigned here just for the current derivation.

Starting with the maximum lift-to-drag ratio E^*, where K and C_{D_0} are related to the parabolic drag polar, the equation is

$$E^* = \frac{1}{2\sqrt{KC_{D_0}}} \qquad \left(C_D = C_{D_0} + KC_L^2\right) \tag{12.14}$$

then we have the constants B, which specifies the entry altitude and physical characteristics of the vehicle; λ, the lift-control constant, which allows for lift-modulation; k_1, defined from the other two:

$$B = \frac{\rho_E\, S\, r_E}{2\,m}\sqrt{\frac{C_{D_0}}{K}} \qquad \lambda = \frac{C_L}{\sqrt{C_{D_0}/K}} \qquad k_1 = B\,\lambda \tag{12.15}$$

where ρ_E and r_E are the density and altitude at atmospheric entry, S is the cross-section area, and m is the vehicle mass. Other constants have been introduced to simplify the equations, namely, η, k, and α:

$$\eta = \frac{B}{E^*\sqrt{\frac{r_E}{H_S}}} \qquad k = \frac{2E^*}{B\sqrt{\frac{r_E}{H_S}}} \qquad \alpha = \frac{r_E\, g_E}{{V_E}^2} \tag{12.16}$$

where H_S is the scale height of the exponential atmosphere model (an exponential atmosphere is assumed), and g_E and V_E are the entry gravitational acceleration and velocity. Lastly, the constant c indicates the non-dimensionalized entry flight path angle ϕ:

$$c = \phi(0) = -\sqrt{\frac{r_E}{H_S}}\, sin\,\gamma_E \tag{12.17}$$

with γ_E as flight path angle at atmospheric entry.

The full set of second-order equations that includes this non-dimensionalization process is presented here. They are taken from Engelsma and Mooij [64]. See that reference for a full description.

The main challenge came from finding an analytical expression relating x, the non-dimensional altitude (it is reciprocal to the altitude - see Equation 12.34), to the range angle τ, coming from the equation $d\tau = dx/d\phi$. The range-angle τ is an independent variable that is obtained from

$$\tau = \sqrt{\frac{r_E}{H_S}}\theta \qquad \frac{d\theta}{dt} = \frac{V\,cos\gamma}{r} \tag{12.18}$$

where θ is also a measure of the range angle. ϕ, as said, is the non-dimensional flight path angle, which can be calculated with

$$\phi^2 = c^2 - 2k_1(e^x - 1) - 2(1-\alpha)x + 2\eta\alpha I(x) \qquad \text{or} \qquad \phi = -\sqrt{\frac{r_E}{H_S}}\,sin\,\gamma \tag{12.19}$$

which in the left expression is the second-order approximation of the flight path angle. In that expression, $I(x)$ is an integral value that gets calculated using Equation 12.26. From the expression on the right note that the sign of ϕ is positive for the descending leg of the trajectory, and negative for the ascending leg, thus opposite to the dimensional flight path angle.

One way of solving $d\tau = dx/d\phi$ analytically is by approximating ϕ with a second-order polynomial (Equation 12.22). It follows that all the other quantities can be expressed by using the coefficients of this polynomial. This approach requires knowing the values of the polynomial coefficients a_1, a_2, a_3. They can be calculated with the following expressions:

$$\begin{aligned} a_1 &= \frac{3}{x_1}\left(2(1-\alpha) - \frac{c^2 + 4k_1}{x_1} + \frac{4k_1\left(e^{x_1} - 1\right)}{x_1^2}\right) \\ a_2 &= -6(1-\alpha) + \frac{2\left(c^2 + 6k_1\right)}{x_1} - \frac{12k_1\left(e^{x_1} - 1\right)}{x_1^2} \\ a_3 &= c^2 \end{aligned} \tag{12.20}$$

where x_1 is the minimum altitude reached during entry. x_1 can be calculated by iteratively solving the left expression of Equation 12.19 for $\phi^2 = 0$, which occurs when $x = x_1$. It is solved by first calculating the minimum altitude x_1' with the first-order approximation of ϕ (the left expression of Equation 12.19 without the term $2\eta\alpha I(x)$). Then, once a first-order approximation of x_1', and a_1', a_2', a_3' is available, the left expression of Equation 12.19 can be solved for $\phi^2 = 0$ by keeping $I(x) = I(x_1')$. Once solved, second-order values for x_1, and a_1, a_2, a_3 are obtained.

All the other quantities can now be derived by using the coefficients a_1, a_2, a_3, calculated with Equation 12.20, and the full aerocapture entry can be reconstructed. The equations that allow for the derivation of all the aerocapture quantities (trajectory parameters, aerodynamic loads, heat fluxes) are the following:

$$x(\tau) = -\frac{a_2}{2a_1} - \frac{\sqrt{a_2^2 - 4a_1a_3}}{2a_1}\sin\left(\sqrt{-a_1}\tau - \arcsin\frac{a_2}{\sqrt{a_2^2 - 4a_1a_3}}\right) \tag{12.21}$$

$$\phi_a^2(\tau) = a_1x(\tau)^2 + a_2x(\tau) + a_3 \tag{12.22}$$

$$\phi_a(\tau,\delta) = \delta\sqrt{\phi_a^2(\tau)} \tag{12.23}$$

$$I_1(\tau,\delta) = \frac{1}{2}\phi_a(\tau,\delta)x(\tau) - \frac{a_2}{4a_1}(c - \phi_a(\tau,\delta)) + \frac{\left(4a_1a_3 - a_2^2\right)}{8a_1}\tau \tag{12.24}$$

$$I_2(\tau,\delta) = -\frac{1}{a_1}(c - \phi_a(\tau,\delta)) - \frac{a_2}{2a_1}\tau \tag{12.25}$$

$$\begin{aligned} I(\tau,\delta) = {} & \frac{\left(1+\lambda^2\right)}{k_1}cx(\tau) - \frac{1}{2}k\alpha x(\tau)^2 + \\ & - \frac{(1-\alpha)\left(1+\lambda^2\right)}{k_1}\tau x(\tau) - \frac{\left(1+\lambda^2\right)}{k_1}I_1(\tau,\delta) + \frac{(1-\alpha)\left(1+\lambda^2\right)}{k_1}I_2(\tau,\delta) \end{aligned} \tag{12.26}$$

$$J(\tau,\delta) = \frac{\left(1+\lambda^2\right)}{k_1}c\tau - \frac{\left(1+\lambda^2\right)}{k_1}x(\tau) - \frac{(1-\alpha)\left(1+\lambda^2\right)}{2k_1}\tau^2 - k\alpha I_2(\tau,\delta) \tag{12.27}$$

$$\phi(\tau,\delta) = \delta\sqrt{\phi^2(\tau,\delta)} \tag{12.28}$$

$$\begin{aligned} v(\tau,\delta) = {} & \frac{\left(1+\lambda^2\right)}{k_1}(c-\phi(\tau,\delta)) - k\alpha x(\tau) + \\ & - \frac{(1-\alpha)\left(1+\lambda^2\right)}{k_1}\tau - \eta k\alpha I(\tau,\delta) + \frac{\eta\alpha\left(1+\lambda^2\right)}{k_1}J(\tau,\delta) \end{aligned} \tag{12.29}$$

$$\frac{D}{g_E}(\tau,\delta) = \frac{\left(1+\lambda^2\right)Be^{x(\tau)-\eta v(\tau,\delta)}}{2\alpha E^*} \tag{12.30}$$

$$\frac{L}{g_E}(\tau,\delta) = \frac{\lambda B e^{x(\tau)-\eta v(\eta,\delta)}}{\alpha} \tag{12.31}$$

$$q(\tau,\delta,C,a,b,M) = CR_n^a\rho_E^b V_E^M e^{bx(\tau)-\frac{M\eta v(\tau,\delta)}{2}} \quad (C,a,b,M \text{ are set by using heat flux data}) \tag{12.32}$$

where all the equations are only dependent on the fixed entry conditions, range-angle τ, and δ. The latter, δ, has a value of 1 or -1, and specifies whether the flight is in the downwards or upwards leg, respectively.

The value of x starts at zero at atmospheric entry, then increases up to a maximum at the deepest point in the atmosphere, and decreases back down to zero at the atmospheric exit. With this in mind, the boundaries of the range of values τ takes can be determined by solving $x(\tau) = 0$. At atmospheric entry, $\sqrt{-a_1}\tau = 0$, and consequently $x(\tau) = 0$. By considering the cyclic behavior of the sin function, one set of roots can be expressed as $\sqrt{-a_1}\tau = 2\pi k$, where k is any integer, or, $k \in \mathbb{Z}$ and the first root is part of this set. Similarly, a second set of roots can be expressed as $\sqrt{-a_1}\tau = (1+2k)\pi + 2\beta$, where $\beta = \arcsin\dfrac{a_2}{\sqrt{a_2^2 - 4a_1a_3}}$, and again $k \in \mathbb{Z}$. Only the smallest two roots (atmospheric entry and exit) described by these two sets are of interest. These roots are, for atmospheric entry and exit, respectively,

$$\tau = 0 \qquad \text{and} \qquad \tau = \left(\pi + 2\arcsin\frac{a_2}{\sqrt{a_2^2 - 4a_1a_3}}\right)\frac{1}{\sqrt{-a_1}} \tag{12.33}$$

When the above equations are evaluated from atmospheric entry to exit, values have to be converted to the classical dimensional variables. The equations needed to transform back to the radial distance, velocity, flight-path angle, and aerodynamic loads are presented here:

$$r(\tau) = -H_s x(\tau) + r_E \tag{12.34}$$

$$V(\tau,\delta) = \sqrt{\frac{V_E^2}{e^{\eta v(\tau,\delta)}}} \tag{12.35}$$

$$\gamma(\tau,\delta) = \arcsin\left(\frac{\phi(\tau,\delta)}{-\sqrt{\dfrac{r_E}{H_s}}}\right) \tag{12.36}$$

$$\frac{D}{g_E}(\tau,\delta) = \frac{D}{g_E}(\tau,\delta)\frac{g_E}{g_E} \tag{12.37}$$

$$\frac{L}{g_E}(\tau,\delta) = \frac{L}{g_E}(\tau,\delta)\frac{g_E}{g_E} \tag{12.38}$$

This set of equations is particularly suited for analytically calculating shallow atmospheric entries, hence with small values of γ_E. This approximation tends to underestimate the impact of steep entry flight path angles, thus it can be considered a counterpart of the first-order approximation, which is best at modeling steep entry trajectories and overestimates shallow entries.

12.1.4. Observations

The suite of analytical tools presented here is quite promising for serving as an initial-state trajectory estimator in the numerical simulations that will be performed. The capabilities of each method will have to be individually verified by means of a full numerical model of the problem. This process will select the most accurate tools for the project.

By just an initial estimation, some considerations can be already made both for multi-flyby tools and aerocapture equation sets.

Modeling the flyby as instantaneously happening at the moon's center of mass leads to a very straightforward approach, but also to a model that lacks too much adherence to reality to be considered viable. Treating the flyby as instantaneous, but now happening at a set distance and location from the moon's center, is already a much better approach than the previous one. In this case, the risk of the vehicle impacting the moon due to a miscalculation of the analytical approximation is still rather large. However, the more precise the model ends up being, the lower the risk of a moon impact is going to be. This does not hold true for the former approach, where a 100% precision would mean certainty of a moon impact. The third approach to flybys, the complete flyby description, is the most complex model out of these three, but at the same time it is also the most promising approach. It is indeed the most accurate model since it includes most of the effects of a satellite-moon gravitational interaction. Its effectiveness will hence be the first to be evaluated, and, if deemed sufficient in terms of both accuracy and efficiency, no other model for flyby would be considered.

Regarding the aerocapture entry, two approaches have been identified. A first-order set of equations, which performs best for large values of γ_E, and a second-order set of equations, which complements the other set by performing best for small values of γ_E. Due to the shallow nature of aerocapture entry trajectories, it is highly expected that the second-order set of equations will perform best when verified with the numerical model, but in this case both approaches will be evaluated, regardless of each one's effectiveness.

12.2. Numerical Modeling

As already mentioned before, the need for a numerical model for the multi-flyby aerocapture at Jupiter comes from the need for verifying all the semi-analytical tools that have been presented and developed. Moreover, the numerical model can become a tool itself to use in simulating the aerocapture trajectory.

A numerical model would also provide highly precise trajectories capable of meeting the requirements set in Chapter 9, thus it would be the ultimate tool for conducting the optimization process and performing the final assessment and evaluation of the aerocapture technique. In this section, its main characteristics will be described.

12.2.1. Environment

Bodies

Bodies that have to be included in the environment are Jupiter, the main body, and the Galilean Moons if flybys are to be performed. However, as presented in Chapter 11, no flybys are considered in the current project. Other bodies that can be included in the environment are Saturn and the Sun, based on the assessment done in Chapter 5.

Accelerations

The accelerations considered for the environment are the gravitational acceleration from Jupiter, and the aerodynamic acceleration from Jupiter's atmosphere. The choice of the gravitational and atmo-

spheric models is made in Chapter 13.

Radiation
For the radiation environment, the orbit will be considered equatorial, thus the equatorial profile for radiation intensity at Jupiter, the profile presented in Chapter 3, will be used.

12.2.2. Propagation and integration schemes

From the literature review conducted previous to the current project, a combination of propagation and integration schemes has been selected. It has been estimated that this combination would be the best candidate for the characteristics of the science case at hand. It is indeed going to be a highly dynamic environment, making the RKF7(8) the best candidate for an integration scheme. Moreover, the absence of singularities and the good performance of the USM7 makes it the best choice in terms of propagation scheme. In conclusion, the following schemes have been chosen:

- USM7, as propagator
- RKF7(8), as integrator

12.2.3. Aerothermodynamical loads

Understanding how severe the entry loads will be for the vehicle is crucial for assessing the effectiveness of the mission. Here their calculation rationale is summarised.

Aerodynamic loads
Aerodynamic loads are calculated using the well-known expressions for the drag and lift forces (Chapter 5 shows how the drag force is calculated). Such formulations are already built in the TUDAT environment that will be used for running the simulations, thus the data about the aerodynamic force will be retrieved from the simulation results. Then, based on the vehicle attitude, the various aerodynamic forces such as lift, drag, and potentially side force, will be calculated.

Thermal loads
The calculation of the thermal loads is thoroughly explained in Chapter 10. For aerocapture trajectories it has been seen that the convective heat flux is much greater than the radiative heat flux, thus making the calculation of the former more important. For the convective heat flux, the following formula will be used, taken from Girija et al. [38]:

$$q_{C_{B=0}} = C_{\text{hfx}} \sqrt{\frac{\rho}{R_N}} V^3 \qquad C_{\text{hfx}} = 0.6556E-4 \tag{12.39}$$

where C_{hfx} is a constant determined by the planet's atmospheric composition, Jupiter in this case, ρ_∞ is the free stream atmospheric density [kg/m^3], R_N is the vehicle's effective nose radius [m], and V is the free stream velocity in [m/s]. Lastly, $q_{C_{B=0}}$ is the ablation-free ($B = 0$) convective heat flux and has units of W/m^2.

For the radiative heat flux, the following formula has been used, from Ritter et al. [56]:

$$q_{R_{\text{AD},B=0}} = 9.7632379^{-37} * (2 * R_N)^{-0.17905} * (\rho)^{1.763827469} * (V)^{10.993852} \tag{12.40}$$

where $q_{R_{\text{AD},B=0}}$ is the radiative heat flux without accounting for non-ablating conditions and non-adiabatic effects, and has units of W/m^2, R_N is the nose radius [m], ρ is the density [kg/m^3], and V is the airspeed [m/s].

The radiative heat flux $q_{R_{\text{AD},B=0}}$ has been then corrected for non-adiabatic effects (Tauber and Wakefield [59]):

$$\Gamma = \frac{4q_{R_{\text{AD},B=0}}}{\rho_\infty V_\infty^3} \qquad q_{R_{B=0}} = \frac{q_{R_{\text{AD},B=0}}}{1+3\Gamma^{0.7}} \tag{12.41}$$

where Γ is the Goulard number (the radiation cooling parameter) and the heating rate $q_{R_{\text{AD},B=0}}$ has here as well units of W/m^2. Here, ablation is neglected ($\dot{m} = 0$, $B = 0$).

Finally, both heat fluxes are corrected for the effect of ablation. The following is a material-dependent correlation derived by Brewer and Brant [61]:

$$\psi_{C_T} = \left[\frac{2.344}{B}\left(\sqrt{B+1}-1\right)\right]^{1.063} \tag{12.42}$$

where the turbulent convective blockage factor, $\psi_{C_T} = q_C/q_{C_{B=0}}$, is represented as a function of the non-dimensional blowing coefficient B. The correlation can be seen in Figure 10.6. The same empirical correlation can be applied to the radiative heat flux as well, with blockage factor $\psi_{R_T} = q_R/q_{R_{B=0}}$ that follows the same correlation.

The blowing coefficient is calculated with:

$$B = \frac{\dot{m}V_\infty^2}{2\,q_{C_{B=0}}} \tag{12.43}$$

assuming $c_p \approx c_{p,\infty}$, and the mass injection rate $\dot{m}$ modeled with a data-regression model (Equation 10.1).

From those heat fluxes, the total heat load and the peak heat flux are calculated, and from that the TPS mass fraction is extrapolated. More on that is discussed in Chapter 10.

12.2.4. Termination conditions

In order to terminate all simulations in a consistent way, a specific set of termination conditions has been selected. The nominal conditions for termination, which have to be satisfied **altogether**, are the following:

- **Bound orbit:** *Terminate when* $E < 0$, hence when the spacecraft's orbit is bound to the planet (analog is to require the semi-major axis to be positive).
- **No aerodynamic forces** *Terminate when* the aerodynamic forces are lower than 0.4 mm/s^2. This prevents termination to occur within Jupiter's atmosphere.
- **Negative flight path angle:** *Terminate when* the spacecraft's γ goes below zero. This allows termination to occur at the final orbit's apocenter, where the γ angle goes from positive to negative.

This set of nominal termination conditions works for all cases where a skipping entry (thus the spacecraft eventually exits the atmosphere) that results in aerocapture (thus the spacecraft enters a bound orbit around the planet) occurs.

For all cases that result in an atmospheric entry undershoot (no aerocapture) or overshoot (no atmospheric exit), additional non-nominal termination conditions have been added. For these non-nominal conditions, even triggering **just one** of them would lead to termination, since each of them tackles a specific non-nominal outcome. They are the following:

- **Minimum distance from Jupiter:** *Terminate when* the spacecraft's altitude goes below 50 km. This condition terminates in case of an overshoot entry.
- **Maximum distance from Jupiter:** *Terminate when* the spacecraft exceeds the boundaries of Jupiter's SoI (48.2 million km). This condition terminates in case of an undershoot entry.
- **Maximum duration:** *Terminate when* the simulation propagates for more than 200 days. Within this timespan, the trajectory is able to fully occur, thus this condition is purely a safe stop in case of unexpected outcomes.
- **Maximum CPU time:** *Terminate when* the elapsed CPU time of the simulation exceeds 5 s. This assures that in case the propagation gets stuck in a non-nominal scenario, the simulation eventually terminates allowing the script to proceed to the next step in a reasonable amount of time.

12.3. Observations

When it comes to modeling complex trajectories such as multi-flyby aerocapture trajectories at Jupiter, both semi-analytical and numerical models have their own advantages and drawbacks. While semi-analytical models are fast and computationally efficient, they often rely on crude approximations of

reality, making them inaccurate and unreliable on their own. This is why they need to be evaluated using numerical models. On the other hand, numerical models that are complex enough to accurately simulate such trajectories can become highly inefficient without an initial-state targeting algorithm. Randomly guessing the initial state of the trajectory would take a large number of guesses before getting closer to optimal solutions. In this scenario, semi-analytical approximations can come in handy in identifying the most promising areas in the design space of decision variables, greatly speeding up the optimization process. Therefore, a combination of both numerical and semi-analytical models can be a powerful tool in designing complex trajectories.

13

Integrator & Environment Tuning

Integrator and environment tuning is a key part of the process to build a robust simulation model for the problem under investigation. This chapter will aim at tuning the integration scheme so that it can achieve the required accuracy without requiring massive computational power. The environment model will also be assessed, to make sure it has the required accuracy for the problem to be effectively studied.

13.1. Integrator tuning

Tuning the integrator is a process that requires setting up a robust benchmark upon which the tuning process can be performed. Hence, the section starts with the definition of a benchmark trajectory, whose accuracy is one/two orders of magnitude more accurate than the required accuracy for the integrator.

On the other hand, the integrator accuracy is usually set to be two orders of magnitude lower than the required accuracy for the physical model. Hence, since in Chapter 9 the set position accuracy was respectively 100, 10, 100 km for approach, aerocapture, post-aerocapture orbit, the set accuracy for the integrator will be 1 km, 100 m, 1 km, for the same respective phases.

As a consequence, the benchmark accuracy will be set to 10, 1, and 10 m for approach, aerocapture, and post-aerocapture orbit.

13.1.1. Benchmark set-up: RK8

Three different step sizes for different parts of the trajectory are selected by running a step size study on the benchmark. The three parts, as said before, are: approach, aerocapture, and post-aerocapture orbit. Each part will be individually studied to select the correct step size for the benchmark that achieves the required accuracy while staying in the truncation error regime. The integration scheme is Runge-Kutta 8; the most accurate Runge-Kutta method available in TUDAT.

Approach arc

This is the arrival part of the trajectory. It arrives in the vicinity of Jupiter, precisely at a 3.9 million km distance, thus outside the influence of any of the Galilean moons. The choice has been made because, when running the analysis, the root finder failed to converge when smaller distances were set, thus resulting in simulation failure. The investigated step sizes range from 10^4 to $61 \cdot 10^4$ s. From such interval, 31 linearly spaced samples were taken.

The resulting final position error for each step size is presented in Figure 13.1, where it can be seen that choosing a step size of 10^5 s could guarantee the required accuracy, staying in the truncation regime, and at the same time maintain a reasonable speed.

As a result, a step size of 10^5 s has been chosen.

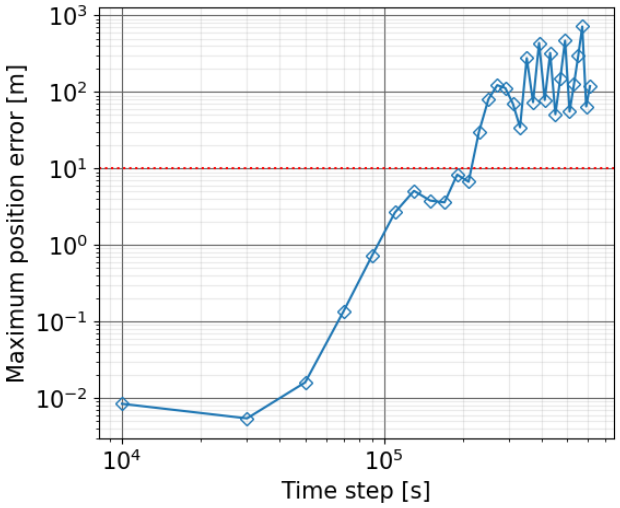

Figure 13.1: Step size study of the approach arc of the benchmark.

Aerocapture arc

This is the aerocapture part of the trajectory, it starts at a 3.9 million km distance from Jupiter, then goes down deep into Jupiter's atmosphere and arrives at a distance of 3.9 million km from Jupiter (again, further than the Galilean moons). The investigated step sizes range from 1 s to 21 s. From such interval, 11 linearly spaced samples were taken.

The resulting final position error for each step size is presented in Figure 13.2, where it can be seen that choosing a step size of 10 s could guarantee the required accuracy, staying in the truncation regime, and at the same time maintain a reasonable speed.

As a result, a step size of 10 s has been chosen.

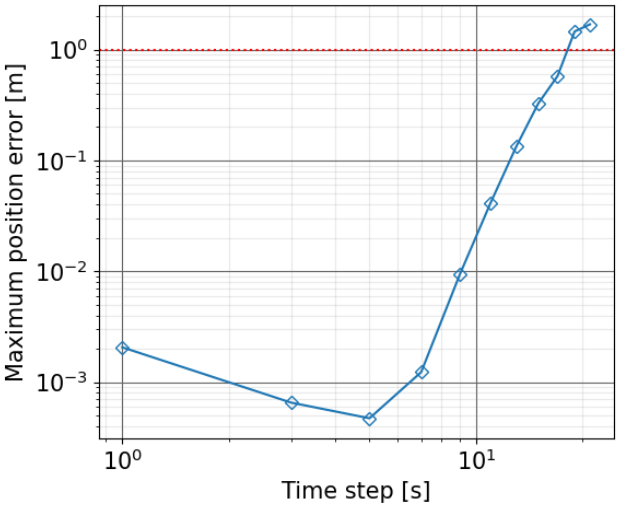

Figure 13.2: Step size study of the aerocapture arc of the benchmark.

Post-aerocapture arc

This is the last part of the trajectory, it comprehends part of the elliptical orbit that results from the aerocapture phase. The propagation is stopped at the apocenter. The investigated step sizes range from 10^4 to $61{\cdot}10^4$ s. From such interval, 31 linearly spaced samples were taken.

The resulting final position error for each step size is presented in Figure 13.3, where it can be seen that choosing a step size of $8{\cdot}10^4$ s could guarantee the required accuracy, staying in the truncation regime, and at the same time maintain a reasonable speed.

As a result, a step size of $8{\cdot}10^4$ s has been chosen.

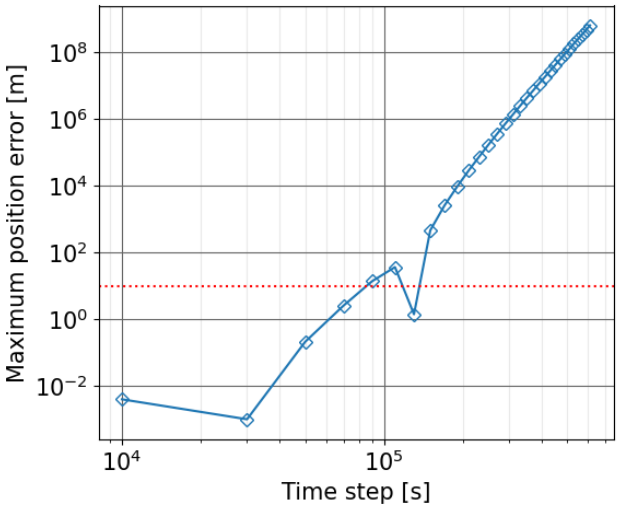

Figure 13.3: Step size study of the post-aerocapture arc of the benchmark.

Result

An issue that arises when using the benchmark to assess the integrator's accuracy is the lack of data points to effectively compare the integration outcome with the benchmark. Figure 13.4 shows the comparison. Apart from the fact that the integrator of choice with tolerance 10^{-14} already outperforms the benchmark, large interpolation errors can be seen. Such errors are caused by the sparse dataset of points.

By instead using the combination (4e3, 4, 4e3) s of step sizes for the benchmark, a relatively close benchmark error behavior can be obtained, despite being in the round-off error regime.

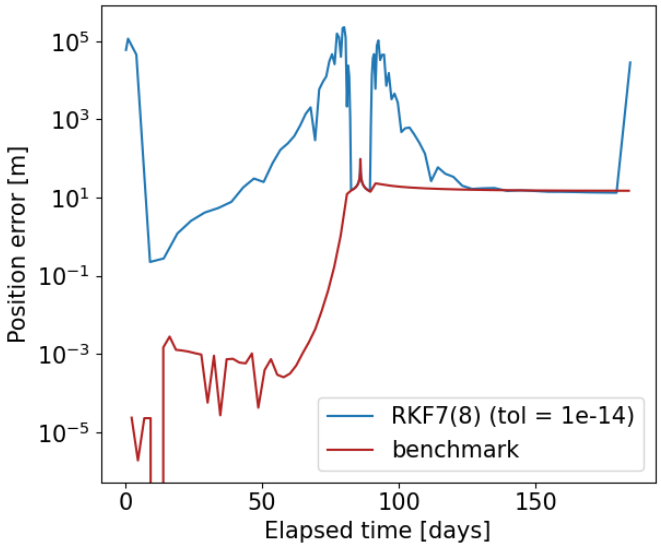

Figure 13.4: Trajectory computed with an RKF7(8) (tolerance set to 10^{-14}), and compared with a benchmark with time steps (1e5, 10, 8e4) s.

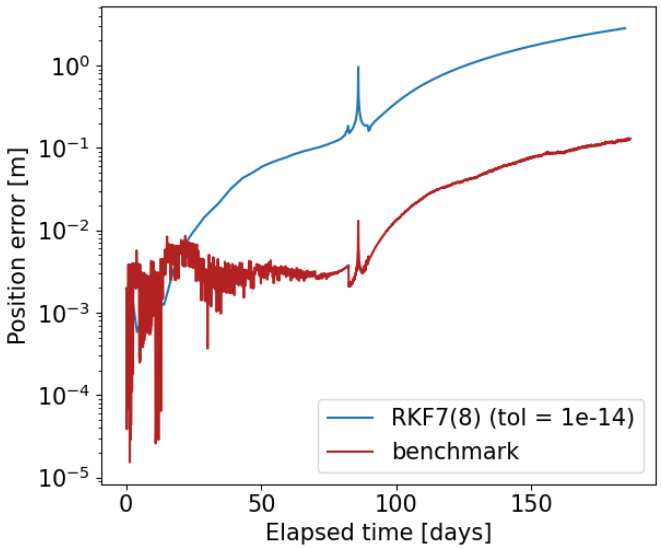

Figure 13.5: Trajectory computed with an RKF7(8) (tolerance set to 10^{-14}), and compared with a benchmark with time steps (4e3, 4, 4e3) s

The result obtained in Figure 13.5 can be considered satisfactory. The benchmark is 2 orders of magnitude more precise than the integrator with such settings and the interpolation errors are much smaller. Their presence now is not dramatic enough for the results to be unreadable, so they can be tolerated unless they pose a problem for future applications.

13.1.2. Integrator accuracy selection

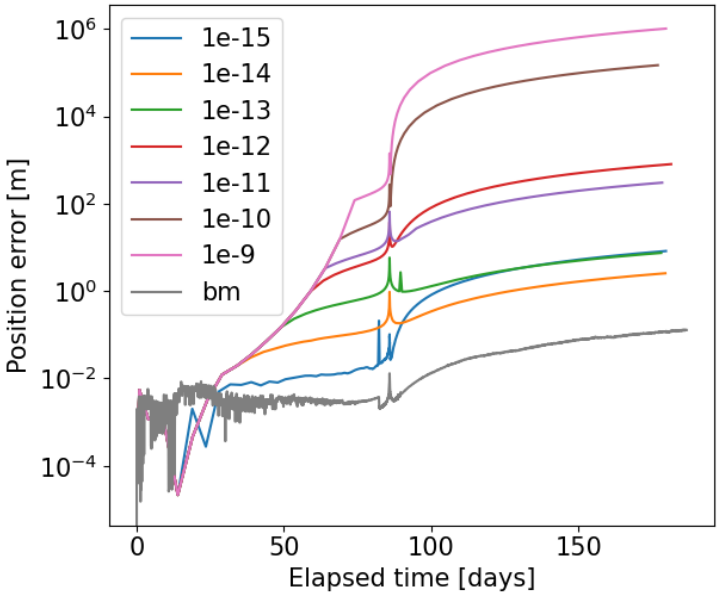

Figure 13.6: RKF7(8) integration scheme evaluated with different tolerances.

The benchmark affects the evaluation only of the most accurate settings for RKF7(8), precisely only the case with tolerance set to 10^{-15}. However, a tolerance set to values around 10^{-14} or 10^{-13} should result in an integration scheme that maintains the required position accuracy of 1 km outside Jupiter's atmosphere, and 100 m within it. The integrator accuracy would actually be better by one or two orders of magnitude, but for the relatively little computational load required for the optimization (see Chapter 15), the focus is more on accuracy than speed.

13.2. Environment tuning

In this section, the major forces at play in the Jupiter system will be evaluated and selected, with their respective models.

13.2.1. Forces assessment

Based on the assessment of forces presented in Chapter 3, some key effects have been selected:

- Jupiter's gravitational pull, the point mass gravity, and the main spherical harmonics effects;
- The Galilean moons' gravitational pull;
- The atmosphere of Jupiter;
- The gravitational pull of Saturn and the Sun;
- The solar radiation pressure effect.

Among these forces, which ones to consider, and how to model them, is the topic of the current section.

13.2.2. Selection

The aspects earlier presented are here evaluated and their inclusion or not is assessed.

Jupiter & atmosphere: The main components necessary for studying the aerocapture technique are Jupiter's gravitational pull and Jupiter's atmosphere, which are included in the environment.
Galilean moons: Regarding the Galilean moons, since no flybys would be performed, and thus the focus is set on the aerocapture technique, their effect on the position accuracy goes beyond the scope of the current project, therefore they are not included in the environment.
Sun & Saturn: The Sun and Saturn could provide perturbations of significant values for the accuracy of the approach phase, as seen in Chapter 3, precisely in Figure 5.7 and 5.8, but since the aerocapture phase is the main focus of the project, their effect on the approach trajectory has not been considered. It is as well something that goes beyond the current scope of the project.
Solar Radiation Pressure (SRP): The same reasoning applies to solar radiation pressure, which would have a major effect during the approach phase of the trajectory. It is as well not included in the environment.

The components included in the environment are thus only Jupiter's gravitational field and its atmosphere.

13.2.3. Models

The available models are here evaluated and the final ones are selected.

Jupiter's gravitational field: For Jupiter's gravitational field, two models can be used: the point-mass gravity, or a spherical harmonics expansion that considers the values of J_2 J_4 and J_8, which according to Figure 5.7 and 5.8 (Chapter 3) have significant contributions in terms of magnitude. Using the spherical harmonics expansion would surely increase the accuracy of the physical model, but since the trajectory is set to fly close to Jupiter's surface, the frequency of the model diverging and resulting in failed runs is rather high. With this drawback, and the fact that its addition would not be necessary for the scope of the project, which is more directed towards a feasibility study, the spherical harmonics expansion has been discarded. As a consequence, Jupiter's point-mass gravity model has been selected.
Jupiter's atmosphere: Regarding Jupiter's atmosphere, due to the fact that its accuracy is the most critical component in determining the aerocapture entry accuracy, the most accurate atmospheric model available for Jupiter has been selected (it has been presented in Chapter 3). The lack of a strict constraint on computation speed allows this model to be chosen without a proper trade-off analysis.

13.3. Observations

A benchmark with step sizes (4e3, 4, 4e3) s, where each step size has been used for a different arc, has been selected, and the integrator RKF7(8) has been evaluated with different tolerances. It has been found that the tolerances set to 10^{-14} provide very good accuracy at a reasonable speed. It is a bit slower but speed was not a driving requirement for the trajectory.

The simulation environment has been defined as well. The final components are Jupiter's gravitational field and its atmosphere.

As environment models for those components, a Jupiter point-mass gravity field has been chosen, since the spherical harmonics expansion was found to be unstable and provided little benefit in accuracy. Moreover, for this feasibility study, the effect of spherical harmonics was not necessary to be included. The atmospheric model has been chosen to be the interpolation of Galileo's data, the most accurate atmospheric model available.

14

Verification & Validation

Verification and validation is a crucial step to assure the correctness and validity of the models. Here, the analytical models have been verified with a numerical model, which has been validated with Galileo flight data.

14.1. Numerical Model Validation

The numerical model has been validated by using data from the Galileo atmospheric entry at Jupiter. Both data from the Galileo trajectory and the thermal loads has been used for the validation.

14.1.1. The Galileo trajectory

The Galileo probe entered Jupiter's atmospheric interface at a speed of about 47.8 km/s, at 450 km altitude. To withstand the intense heat generated by the atmospheric entry, the probe was protected by a heat shield made of carbon phenolic material. As the probe decelerated, it experienced peak temperatures up to 15,500 °C and deceleration forces up to 230 g [61].

Only the first part of the Galileo entry has been implemented into TUDAT for the model validations, specifically the atmospheric entry, up to the heatshield ejection phase. The probe has been modeled to be a spherical shape of the same cross-section as the probe. The descent trajectory has been found to not provide data of great interest for validating an aerocapture trajectory model. Reconstructed flight data available in Table B.2 and Table 10.4 has been used to validate both the trajectory dynamics, with the acceleration loads, and the heat fluxes.

14.1.2. Model accuracy results

As can be seen in Figure 14.1 and 14.2, several aspects of the flight trajectory have been compared. Specifically, the drag acceleration, the altitude, the flight path angle, the Mach number, the density, and the airspeed. The simulated data and the validation data from the Galileo mission seem to be in good accordance.

A closer look, given by Figure 14.3, shows how the error in airspeed goes up to 1 km/s, but just during the peak of the entry loads, whereas the error in altitude remains within 5 km. The f.p.a. angle significantly diverges towards the end of the trajectory. This could have to do with the difference in shape between the actual probe and what has been used for the simulations here. However, the accuracy meets the requirements set for the project, thus a better model for the shape has been deemed unnecessary for this project.

Overall, the results indicate a rather good accordance of the model with the validation data. The accuracy of the model would be high enough for the purposes of the current project.

An observation goes to the discrepancy of the Mach number as well, as seen at the beginning of the trajectory in Figure 14.2. This discrepancy originates from the atmospheric model used in the simulations, which uses real in-flight density data from the Galileo mission, but sets the atmospheric temperature to be constant. As a result of this, the speed of sound remains constant as well throughout the whole trajectory, and the Mach number is affected as a consequence.

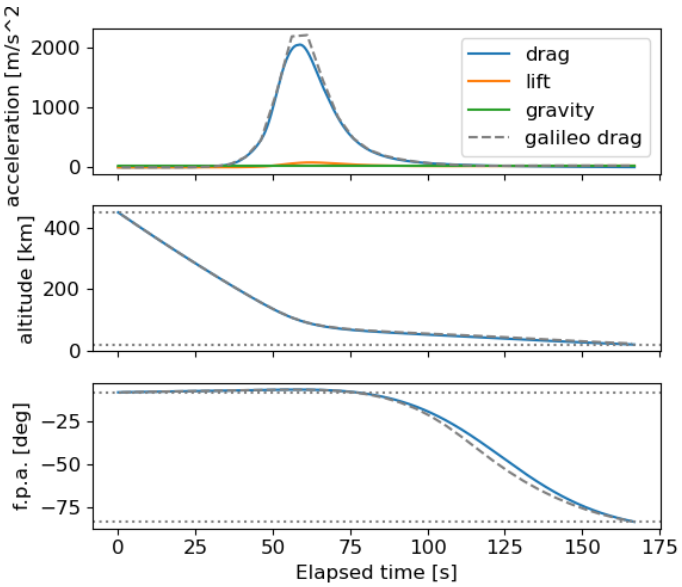

Figure 14.1: Acceleration, altitude, and flight path angle plots of the Galileo descent. The dashed grey line indicates the trend expressed by the validation data. t=0 is set at the entry interface.

The only parameter of concern would be the flight path angle (Figure 14.1 and 14.3), which varies significantly during the end of the atmospheric entry, and the beginning of the descent. This is likely due to unmodelled effects such as mass ablation that greatly impact the simulation accuracy at a later stage of the trajectory for this variable. The same reasoning applies to the other variables, although for the velocity it happens more on the peak of deceleration. Again, this does not pose a serious issue for the accuracy of the simulations, since effects such as mass ablation (which are not included in the numerical model) are not that significant in an aerocapture scenario. The thermal loads are somehow contained, thus leading to little to no ablation on the vehicle.

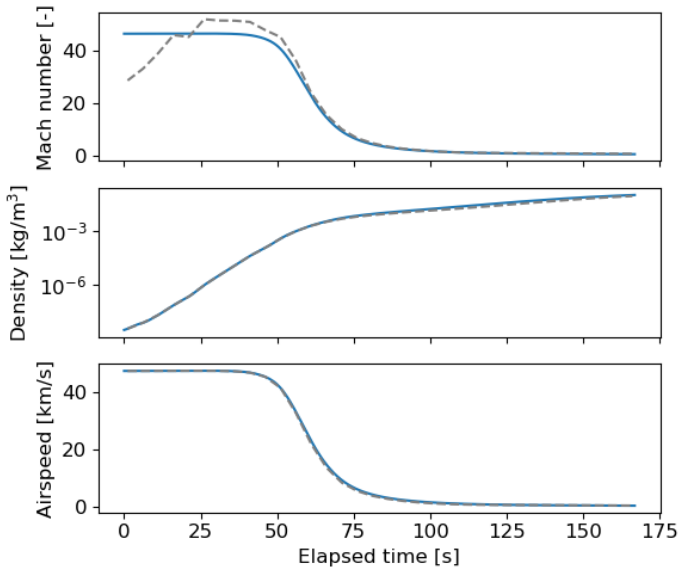

Figure 14.2: Mach number, density, and airspeed plots of the Galileo descent. The dashed grey line indicates the trend expressed by the validation data. t=0 is set at the entry interface.

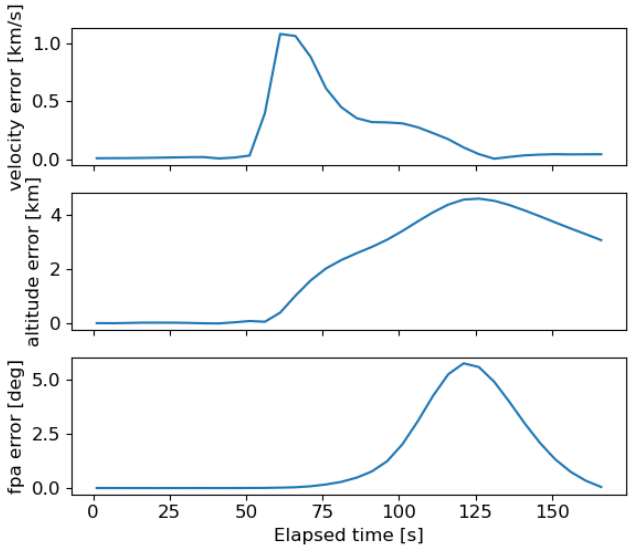

Figure 14.3: Plots of velocity, altitude, and flight path angle errors during the Galileo descent. t=0 is set at the entry interface.

14.1.3. Aerothermal loads

The thermal loads are verified by flying the Galileo probe in the simulation environment and assessing whether the models in use comply with results from the Galileo mission.

Validation data

To verify the correctness of the equations for the thermal loads, reconstructed in-flight data has been taken from Park [37] and is here provided in Table 10.4. The actual values of the wall convective heat flux, wall radiative heat flux, and boundary-layer edge radiative heat flux are there available for altitudes ranging from 100 to 200 km. Such data has been interpolated with respect to altitude, by means of an 8-th order Lagrange interpolator, but its validity cannot extend beyond that altitude range because of the large extrapolation errors that would be introduced.

Convective heat flux

A first observation regards the convective heat flux calculated with Equation 10.8, which appears to be of the same order of magnitude as that calculated with Equation 10.7 (see Figure 14.4). For this reason, Equation 10.8 has been kept as the preferred method for the calculation of the convective heat flux. The selected equation, already presented in Chapter 10, is the following:

$$q_{C_{B=0}} = 2004.2526 * \frac{1}{\sqrt{\frac{2*R_N}{0.6091}}} * \left(\frac{\rho}{1.22522}\right)^{0.4334441} * \left(\frac{V}{3048}\right)^{2.9978867}$$

When corrected for the effect of ablation ($\psi_{C_T} = q_C / q_{C_{B=0}}$), the current model still overpredicts Park's results, although it shows the expected qualitative trend. A deeper investigation of the problem might highlight the cause of the overprediction, but the current result could be still used as a conservative measurement of the actual flux experienced by the probe. Moreover, the effect of ablation for an aerocapture entry will not be as pronounced as that for the Galileo probe, thus reducing the error committed when modeling this effect.

The analysis of the results would anyway have to consider the overprediction factor, but there would be certainty over the fact that the convective heat flux does not get underdetermined.

A plot of the two correlations, the selected correlation with the blockage effect included, and the results from Park [37], is available in Figure 14.4.

Radiative heat flux

The radiative heat flux $q_{R_{\text{AD},B=0}}$, calculated with Equation 10.15, is over-determined when compared to results from Park [37], as shown in Figure 14.5.

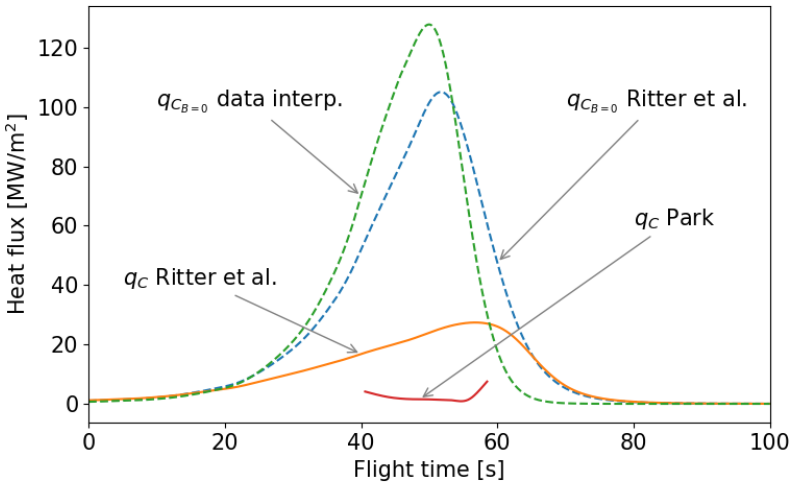

Figure 14.4: Comparison between the convective heat flux ($q_{C_{B=0}}$) calculated with the correlation obtained by data interpolation in this work and the correlation provided by Ritter et al. [56]. The correlation provided by Ritter et al. [56] has been kept and adjusted for the ablation effect ($\psi_{C_T} = q_C/q_{C_{B=0}}$). This correlation has been then compared to the actual heat fluxes experienced by Galileo, those calculated by Park [37].

However, when the non-adiabatic effects on radiation are considered, the curve ($q_{R_{B=0}}$) matches the boundary-layer-edge radiative heat flux $q_{R,e}$ calculated by Park [37], but it is still higher than the wall radiative heat flux.

Finally, when also the blockage effect due to ablation injection is considered, the curve (q_R) comes close to matching the wall radiative heat flux $q_{R,w}$ calculated by Park [37]. The wall conditions for the incident radiative heat flux are then well approximated by the selected method, as clearly shown in Figure 14.5.

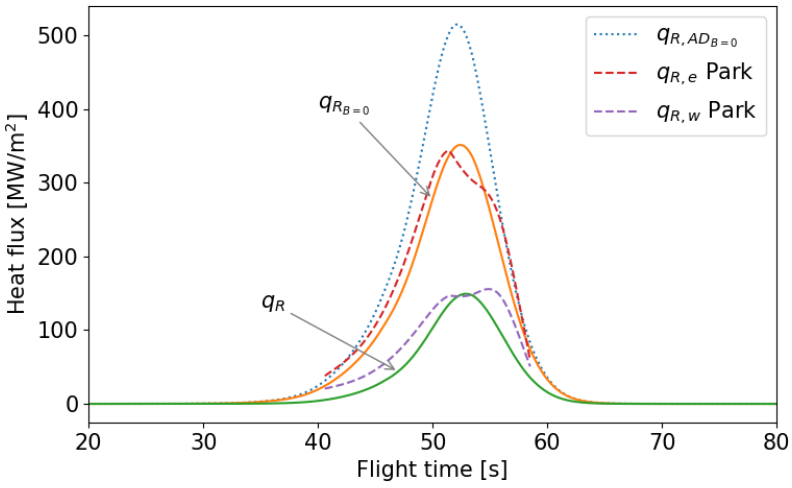

Figure 14.5: Radiative heat flux calculated at different conditions and compared to results from Park [37]. $q_{R_{AD,B=0}}$ is the total incident heat flux, $q_{R_{B=0}}$ is the heat flux rescaled accounting for non-adiabatic effects, q_R is the wall incident heat flux, where also the effect of ablation has been considered. For Park [37] results, $q_{R,e}$ is the radiative heat flux at the boundary-layer edge, and $q_{R,w}$ is the radiative heat flux at the wall.

Integrated heat load

The total integrated heat load that results from a simulated Galileo entry has been seen to comply with the value reported by Figure 10.7, which is about 200 kJ/cm^2. For this to happen, all the main effects on the heat fluxes have to be taken into account. The total integrated heat load calculated for the wall

conditions is 226.631 kJ/cm^2, which corresponds to a mass fraction of 0.526.

As a consequence, the resulting TPS mass fraction matches rather well the actual TPS mass fraction of the Galileo probe.

Observations

The models for calculating the convective and radiative heat flux have been verified using the Galileo probe trajectory and heat fluxes from the literature.

Good accordance between Galileo's radiative heat flux and the radiative heat flux models has been found, whereas the calculation for the convective heat flux seems to overpredict the actual values when excessive ablation is occurring. Anyway, the overprediction is not severe, thus making this model a good conservative tool for calculating the convective heat flux.

The total heat load resulting from the numerical model is also closely matching the total heat load experienced by the Galileo probe. The TPS mass fractions match as well as a consequence.

Although an aerocapture trajectory has a different geometry than the Galileo entry, such models can be considered reliable enough for a rough estimate of the thermal loads for aerocapture.

An uncertainty analysis to understand the impact of the model uncertainty would increase the insight into the models in use, which is essential to assess their robustness when applied for aerocapture.

14.2. Analytical Model Verification

The analytical model prediction accuracy is here verified with the numerical model, and the results of such verification are presented.

14.2.1. Verification process

The analytical model presented in Chapter 12 and Chapter 11 has been verified using a numerical model that features Jupiter's point-mass gravity, the most accurate atmosphere model, and the point-mass gravity of the moon of the flyby.

The problem parameters have been varied through a grid search according to the boundaries presented in Table 14.1. The variation has been for a single parameter at once. The nominal ones are present in that table as well. For each parameter, and for each moon considered (4 Galilean moons), 100 runs have been performed, evenly line-spacing the selected parameter among the considered interval.

Decision Variable	Lower Boundary	Upper Boundary	Nominal Value	Unit
Interpl. Velocity V_{J_∞}	5100	6100	5600	m/s
Entry Fpa γ_E	-4	-0.1	-3	deg
Flyby Epoch t_{flyby}	14610	14627	14610	days since J2000
Impact Parameter B	-$r_{\text{SoI}_{\text{moon}}}$	$r_{\text{SoI}_{\text{moon}}}$	R_{moon}	m

Table 14.1: Decision variable ranges for the verification

The numerical model has been run by using the initial state and epoch calculated by the analytical model, those that according to the assumptions of the analytical model would result in the desired trajectory.

For the validation, the propagation of the numerical model has been set to start at the atmospheric entry interface, with the entry state and epoch provided by the analytical model. This allowed to remove any integration error stemming from the approach phase, but most importantly it ruled out the perturbation of the moon's gravity that would have affected the orbit precision during the approach, leading to a different entry state. In this way, the actual accuracy of the atmospheric entry equations, and of the subsequent parts of the model, have been properly assessed.

14.2.2. Results

Among all the results obtained from the grid search, the variable with the strongest impact on the outcome of the simulations has been seen to be the entry flight path angle γ_E, whereas other parameters did not induce many variations in the results. The entry velocity has shown to be almost not sensitive to a change in the interplanetary velocity V_{J_∞}, as it has been just marginally affected by a variation of V_{J_∞}

along all the interval provided by Table 14.1. The epoch of the flyby, on the other hand, just affected the position of the initial state, and the initial epoch, since the trajectory geometry is built around the desired arrival conditions at the moon. Lastly, the impact parameter, B, had little effect on the overall outcomes of the simulations, and did not greatly influence the comparison. Here, the main driver of the analytical model accuracy was the aerocapture phase, rather than the flyby phase.

For all these reasons, the most impactful decision variable has been the entry flight path angle γ_E, and thus all results portrayed here show how the accuracy varies with a variation of such variable.

As seen in Figure 14.6 and 14.7, the position and velocity errors escalate rather quickly right after the aerocapture phase, although this representation is far too general and does not give much insight into what is the root cause of these errors. The position error shown in Figure 14.6 might appear to rise as γ_E decreases, however, this is only due to the fact that shallower flight path angles lead to more elliptical orbits (or escape trajectories), thus terminating the simulation, and comparison, at a later moment in time, where the discrepancies have had more time to increase.

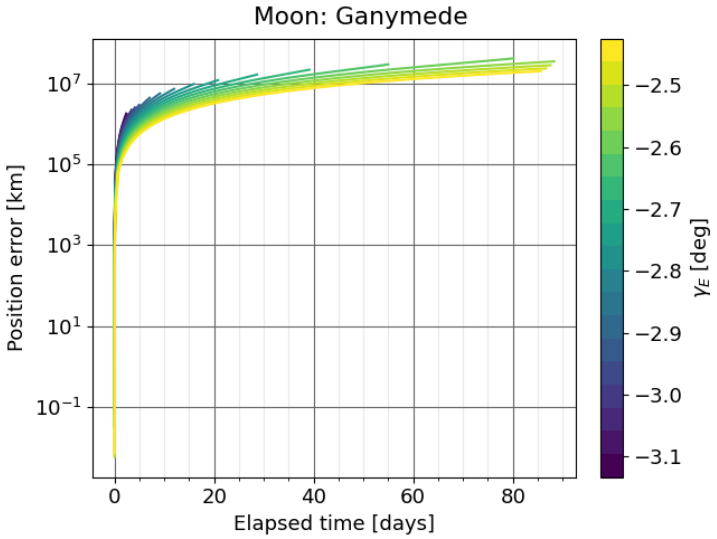

Figure 14.6: Magnitude of position error between the analytical and the numerical model. Starting epoch is set at the atmospheric entry interface. The runs have been performed by varying the atmospheric entry flight path angle γ_E, and the successful runs have been plotted.

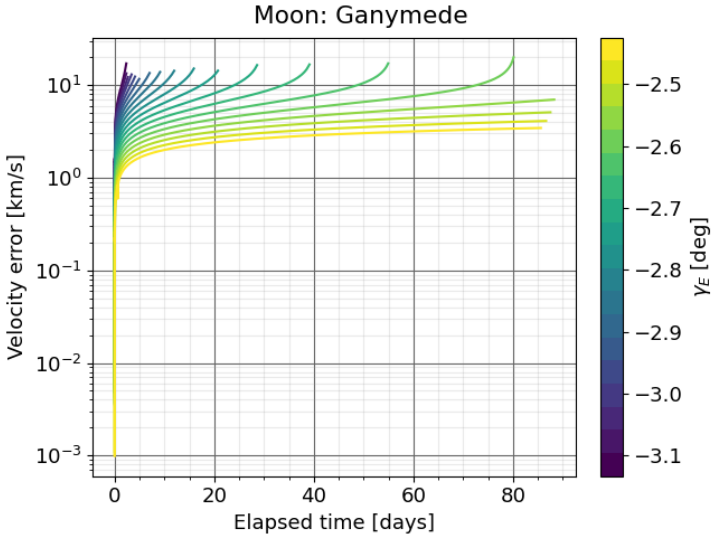

Figure 14.7: Magnitude of velocity error between the analytical and the numerical model. Starting epoch is set at the atmospheric entry interface. The runs have been performed by varying the atmospheric entry flight path angle γ_E, and the successful runs have been plotted.

A look at what components of the position and velocity errors are more affected is given by Figure 14.8, where the errors have been presented in the RSW components. The R and S components are the most affected, with the R axis being the most affected one, whereas the W component has been seen to be rather stable. This behaviour can be explained by the different geometry of the resulting orbits. As it will be later shown, it often happens that the analytical equations for aerocapture have a tendency to undershoot the exact solution, thus leading to capture orbits with a much shorter period than the capture orbits resulting from the numerical model. Moreover, it often happens that what has been computed to be a capture orbit by the analytical model, is actually an unbound orbit according to the numerical model (see Figure 14.11). This discrepancy in geometry explains the great difference in the R, and in the S directions of the RSW frame.

Lastly, the errors in velocity are a result of such reasoning. Being the two geometries very different, it follows that the velocity vectors at any given epoch will be pointing toward different directions, leading to errors in velocity that shine a grim light on the analytical model, making its predictions appear worse than what they actually are.

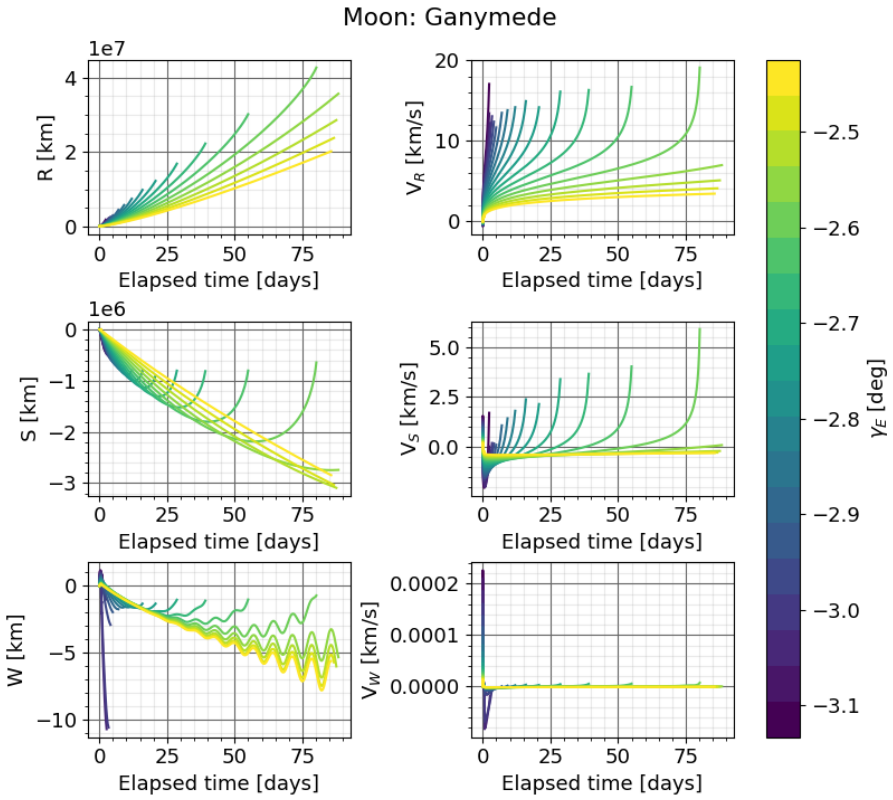

Figure 14.8: Error in position and velocity along the RSW axes (R: radial, S: along track, W: across-track), between the analytical and the numerical model. Starting epoch is set at the atmospheric entry interface. The runs have been performed by varying the atmospheric entry flight path angle γ_E, and the successful runs have been plotted.

Such information from the RSW components of the position and velocity error gives more insight into how the two orbits diverge after the aerocapture phase. However, the key point that should be investigated to address the root causes of such discrepancies is indeed the aerocapture phase itself.

For this reason, the aerocapture phase has been singularly investigated, and its aspects individually examined. The trend shown by various driving quantities of the aerocapture phase is presented in Figure 14.9 and 14.10. These figures show the behavior of errors on flight data as well as on loads acting on the vehicle. In these figures, it comes clear how reducing the entry flight path angle γ_E leads to more accurate solutions, as expected. The analytical equations perform better with shallow values of γ_E. The trend is confirmed by every quantity presented in those figures.

Regarding the accuracy of the atmospheric exit state, a reasonable value of γ_E that leads to a stable capture orbit is around 3 degrees, thus errors up to 50 km in altitude and 1.5 km/s in velocity can be expected for a nominal aerocapture trajectory computed with the analytical model.

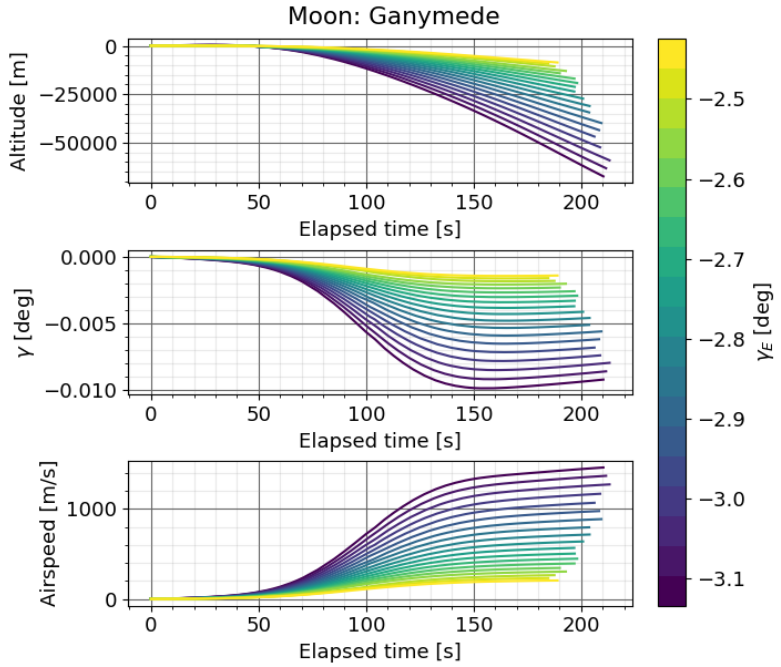

Figure 14.9: Error in altitude, flight path angle, and airspeed, between the analytical and the numerical model. Here, only the atmospheric entry phase is considered, and the elapsed time is in the order of 100s of seconds. The runs have been performed by varying the atmospheric entry flight path angle γ_E, and the successful runs have been plotted.

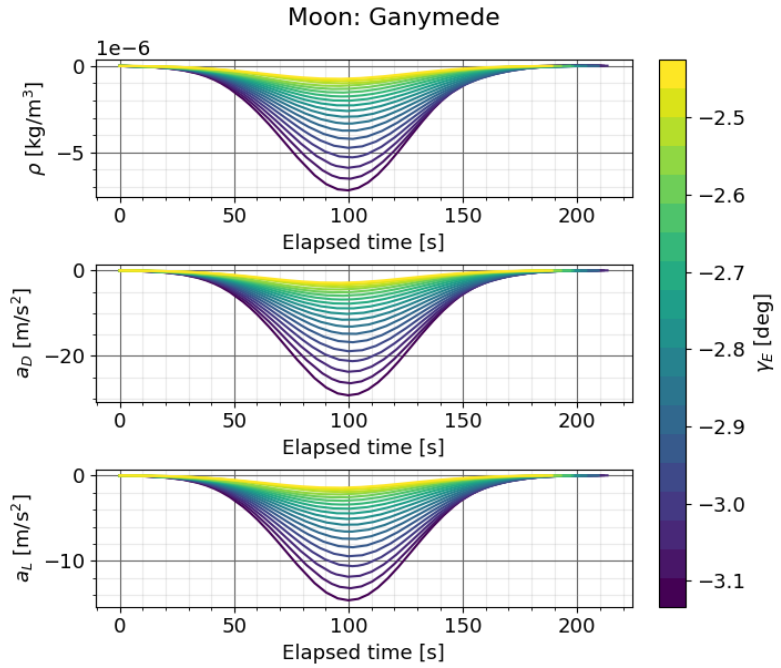

Figure 14.10: Error in atmospheric density, drag and lift accelerations, between the analytical and the numerical model. Here, only the atmospheric entry phase is considered, and the elapsed time is in the order of 100s of seconds. The runs have been performed by varying the atmospheric entry flight path angle γ_E, and the successful runs have been plotted.

Regarding the errors made in computing the atmospheric entry loads, Figure 14.10 shows how the drag acceleration a_D can be off by more than 20 m/s^2, and 10 m/s^2 for the lift acceleration a_L. Considering that the magnitudes of such accelerations computed with the numerical model are 5 m/s^2 for a_D and 2 m/s^2 for a_L, it results that the analytical model over-predicts the intensity of such loads on the vehicle by an order of magnitude, leading to conservative solutions.

A good insight into what might be the cause of the issue is given by the error in atmospheric density computed by the analytical model. Even if its magnitude is rather small, the great impact of other quantities along the entry would make this difference have an important effect on both a_D and a_L, since the mathematical expression of both accelerations depends on ρ. Another contributing factor could be coming from the different velocity vectors used for the computations. While the numerical model considers the spacecraft's velocity w.r.t. Jupiter's atmosphere, the airspeed indeed, the analytical model makes use of the spacecraft's inertial velocity w.r.t. Jupiter. Those two values can differ by more than 10 km/s. The inertial velocity is indeed around 60 km/s, whereas the airspeed for an equatorial entry in Jupiter's rotational direction is around 47 km/s.

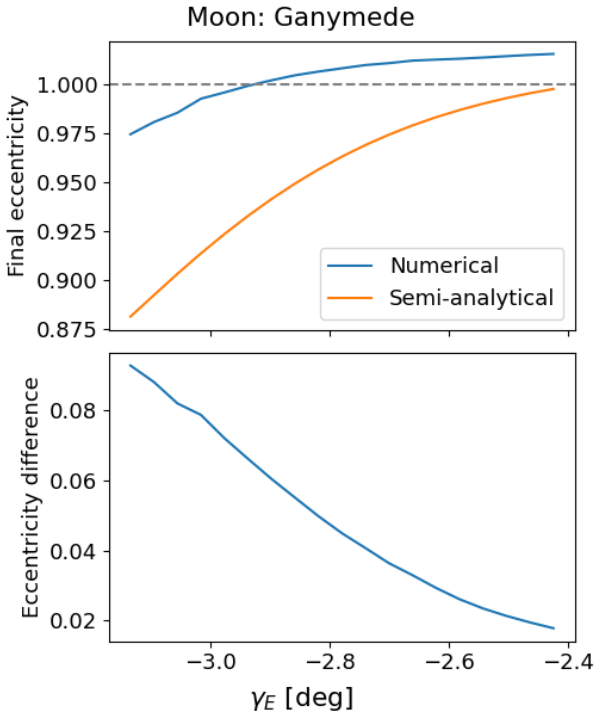

Figure 14.11: The eccentricity of the final orbit computed by the analytical and numerical models is shown in the figure above as it varies for different values of the entry flight path angle γ_E. In the figure below, the error between the two eccentricities is presented.

Finally, a key quantity to investigate in order to assess the reliability of such analytical model is the eccentricity of the final orbit e_{final}. Figure 14.11 shows e_{final} computed by the numerical and semi-analytical models for various values of γ_E, and as presented there it is clear how the analytical equations greatly undershoot the final orbit eccentricity, leading to many theoretically captured states that do not lead to orbital capture when verified numerically. The error in final eccentricity is rather dramatic as well, far too beyond the set accuracy requirement in Chapter 9. It decreases as γ_E decreases, as expected, although it still remains too large for the usable range of γ_E the problem requires.

14.3. Final Observations

In this chapter, a numerical model for aerocapture at Jupiter has been validated using Galileo flight data from the homonymous mission. There is a rather good accordance between the model and the data, making it suitable for the current study. The validation has been performed with a spherical model for the probe, since the actual shape was not yet implemented. Due to the good agreement with the flight data the implementation of a better and more accurate shape, while being truly a valuable addition to the project, has been seen as unnecessary given also the time constraints of the project.

An analytical approximation of the aerocapture at Jupiter has been verified by using this validated numerical model. The results indicate that a refinement of the analytical model is needed, as some of the assumptions made in the analytical expressions are not valid according to the numerical outcomes. The airspeed the numerical model uses differs from the inertial velocity the analytical equations use,

thus this aspect has to be surely tackled to improve the performance of the analytical equations. Then, the atmospheric model could play a big part in the analytical evaluation of the mechanical loads, thus a more accurate model for the atmosphere has to be considered. All these additions to the analytical model, while clearly adding much value to the project, exceed its time constraints, thus they will be left as future recommendations for studies in this matter.

Part IV

Research

15

Optimization

This chapter covers the final formulation of the problem, and its subsequent optimization for the selected objectives. From that, the best solutions are drawn, and observations on their feasibility and robustness are made.

15.1. Jupiter Aerocapture Problem

The final version of the aerocapture problem at Jupiter is here redefined and presented.

15.1.1. Definition

As seen in Chapter 11 and 14, some aspects of the problem have been removed to better focus on the main research question, and the model of choice has resulted to be the numerical model. In fact, the addition of flybys adds value to the problem but either they pose too strict constraints, or their study would exceeds the time constraints of the project. Moreover, the semi-analytical equations for aerocapture have shown to underperform under the range of entry flight path angles γ_E of the problem, thus the numerical model has been preferred.

The definitive problem would then feature an aerocapture trajectory at Jupiter, numerically computed with the numerical model presented in Chapter 12. The trajectory would start at atmospheric entry and would end at the apocenter of the post-aerocapture bound orbit. In case of unbound orbits, the trajectory would end once the spacecraft exits Jupiter's SoI. Therefore, as presented in Chapter 9, the environment of the aerocapture entry consists of Jupiter's point mass gravity, and Jupiter's atmosphere. The atmospheric model consists of Galileo data interpolation, the most accurate model available for Jupiter's atmosphere.

While the gravitational irregularities of Jupiter would be capable of affecting the shape of the trajectory, they are unlikely to be of such magnitude that they would significantly alter the final results and the values of the objective functions. The focus of the optimization is more directed towards finding the mass benefits of an aerocapture trajectory, rather than precisely assessing the trajectory accuracy. The point-mass gravity model has been preferred as it is faster and does not pose the risk of diverging (thus resulting in an unsuccessful simulation) when getting close to the surface of Jupiter.

15.1.2. Description

The final problem hence consists of two decision variables, the interplanetary excess velocity $V_{J\infty}$, and the entry flight path angle γ_E, which would define the shape of the arrival trajectory and the atmospheric entry state. The results of the entry trajectory then lead to a final orbit which has to be bound to the planet (a constraint on eccentricity) and has to respect thresholds on aerothermodynamical loads.

The trajectory is equatorial, since it leads to the most favorable airspeed by taking advantage of the planet's rotation. The entry interface is set at 450 km. By using the vis-viva equation, the value of the entry velocity V_{JE} can be easily retrieved, and by knowing γ_E the velocity vector can be determined. The position vector is arbitrarily set at an altitude of 450 km on the equatorial plane, due to the cylindrical symmetry of the problem.

As a result of this new problem definition, the list of objectives, decision variables, and constraints, has been adapted accordingly.

15.2. Objectives, Decision Variables, Constraints

The new quantities, objectives, decision variables, and constraints, for the optimization of the final problem are presented here.

15.2.1. Objectives

Three objectives have been selected for the optimization.

f_{payload}: Maximum payload mass fraction
This objective aims at maximizing the mass fraction of the spacecraft that does not comprehend the heatshield or the Entry Support System (ESS), thus not only the mass fraction of the science instrumentation. Its calculation has been shown in Chapter 9, when talking about the calculation of the payload mass.

***Radiation Dose*: Minimum total radiation dose**
This objective aims at minimizing the total radiation dose to be absorbed by the spacecraft. It is calculated based on the equatorial radiation intensity profile available in Chapter 3, and the intensity function is integrated based on the time the spacecraft spends at each altitude.

***Aerocapture Benefit*: Maximum benefit over impulsive burns**
Although it might seem similar to the f_{payload} objective, the *Aerocapture Benefit* subtracts the f_{payload} objective with the propellant mass fraction required for a spacecraft to operate a Jupiter insertion burn maneuver at an altitude of 2000 km. The target orbit of the insertion burn maneuver has an eccentricity of 0.98. A positive value for the objective indicates that aerocapture is preferable over a conventional impulsive-burn scenario.

15.2.2. Decision variables

Two decision variables have been selected for the optimization.

Interplanetary arrival velocity $V_{J\infty}$
The excess velocity a spacecraft would arrive with when entering Jupiter's SoI.

Atmosphere entry flight path angle γ_E
The flight path angle a spacecraft would have when entering Jupiter's atmosphere. The entry interface is set at an altitude of 450 km.

15.2.3. Constraints

The following constraints have been set for the optimization.

Maximum peak heat flux
The entry probe would feature a HEEET heatshield, which can resist heat fluxes up to 5000 W/cm^2. This value is set as the maximum allowable peak heat flux.

Maximum aerodynamic loads
The maximum allowable aerodynamic acceleration has been set to 30 g_E. While a spacecraft could be designed to resist loads up to hundreds of g$_E$'s, the requirements on its structure would need a larger mass fraction allocated for that, in order to resist such loads. This is why entry trajectories that exceed this constraint have not been considered.

Minimum and maximum Jupiter distance
The minimum distance is set at Jupiter's radius R_J, and the maximum distance at Jupiter's SoI edge, $R_{J\,SoI}$. This constraint assures that the spacecraft's final trajectory flies within the mission space, that is Jupiter's SoI, and does not crash into Jupiter's atmosphere

Final orbit eccentricity
The maximum allowable eccentricity for the post-aerocapture orbit is set to 0.99. Values beyond 0.99 are considered to pose great risks to the state of the final orbit. Small errors could result in unbound final orbits, with the spacecraft that would fly away from Jupiter without being captured.

15.3. Grid Search

For the optimization of the problem, a grid-search strategy has been implemented. The presence of only two decision variables made this choice possible, as even trying every possible combination of the two still leads to a number of simulations that can be handled and stored by the hardware in use for the project.

15.3.1. Methodology

The grid search has been conducted by taking 100 values for each decision variable, equally spaced within each variable interval range. Each combination of the two decision variables has been run, for a total of 10,000 simulations performed. Each run is referenced with its run index, an index that goes from 0 to 9999. It will be later used when talking about optimal solutions.

Each simulation returned the values for the objective functions, and the quantities relative to each constraint. The set of simulations has been then filtered with the constraint requirements leading to the results shown in the next section.

15.3.2. Results

The resulting values of the objective functions have been plotted, one objective against the other, in Figure 15.1, 15.2, and 15.3. Figure 15.1 shows the relationship between the *Aerocapture Benefit* and the f_{payload} objectives. Two values that are clearly closely correlated, as expected. This strong correlation, while present for the γ_E decision variable, is less pronounced when related to the $V_{J\infty}$ variable. The *Aerocapture Benefit* objective is indeed more sensitive to a change in $V_{J\infty}$ than f_{payload}. This has to do with the fact that *Aerocapture Benefit* is a subtraction of two values: the f_{payload} objective, and the propellant mass fraction for a classical Jupiter insertion maneuver. The atmospheric entry trajectory is not that sensitive to a change in $V_{J\infty}$, whereas the required Δv and propellant mass for a classical Jupiter insertion maneuver is indeed sensitive to changes in $V_{J\infty}$.

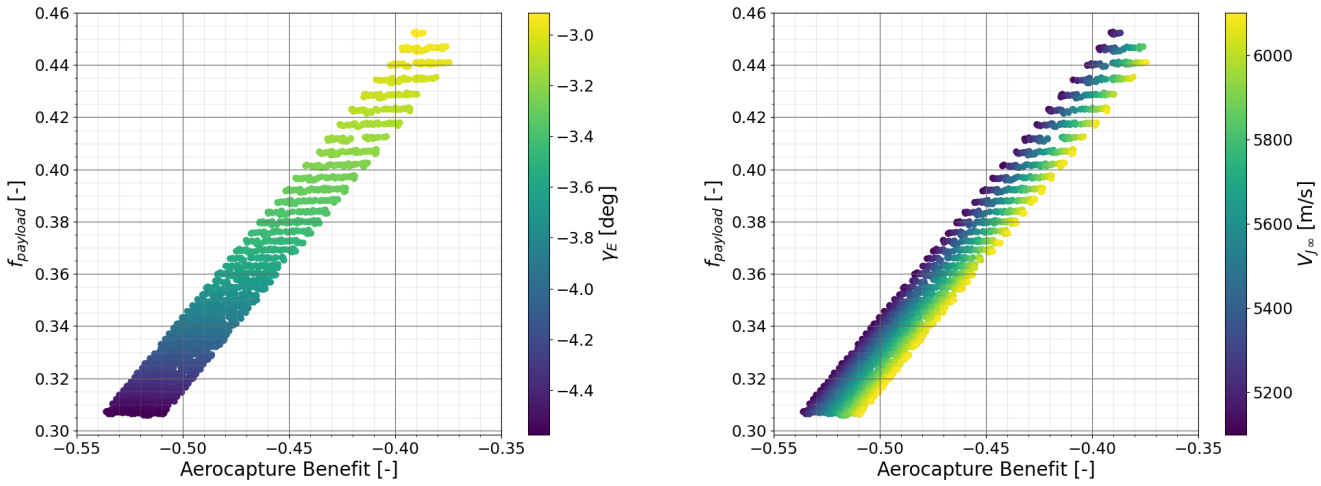

(a) The coloring represents the change in the γ_E decision variable

(b) The coloring represents the change in the $V_{J\infty}$ decision variable

Figure 15.1: The objective *Aerocapture Benefit*, which indicates the savings in payload mass fraction w.r.t. a nominal insertion burn, is plotted against the objective f_{payload}, that is the payload mass fraction of the aerocapture technique. Results are already filtered for constraints.

Such difference in sensitivity can indeed be seen between Figure 15.2 and 15.3. On the first figure the

f_{payload} objective is almost invariant w.r.t. V_{J_∞}, whereas *Aerocapture Benefit* shows a larger variation for the same change in V_{J_∞}. The two objectives compared in Figure 15.1 are hence similar but with some key differences. One, f_{payload}, is more suitable when the focus of the study is towards maximizing the payload mass fraction of the probe (here payload is still considered in a more general sense), whereas the other, the *Aerocapture Benefit*, represents a comparison between two techniques and is indeed more suitable when the focus is on comparing them. The following study is focused on assessing the benefits the aerocapture technique can provide compared to already existing orbital insertion strategies, thus the *Aerocapture Benefit* objective is indeed the best candidate to assess such comparison. The f_{payload} objective has been investigated to make sure it was not competing with the *Aerocapture Benefit*, and since Figure 15.1 clearly shows how the two objectives are strongly and positively correlated, only the *Aerocapture Benefit* objective will be considered for the analysis of optimum points.

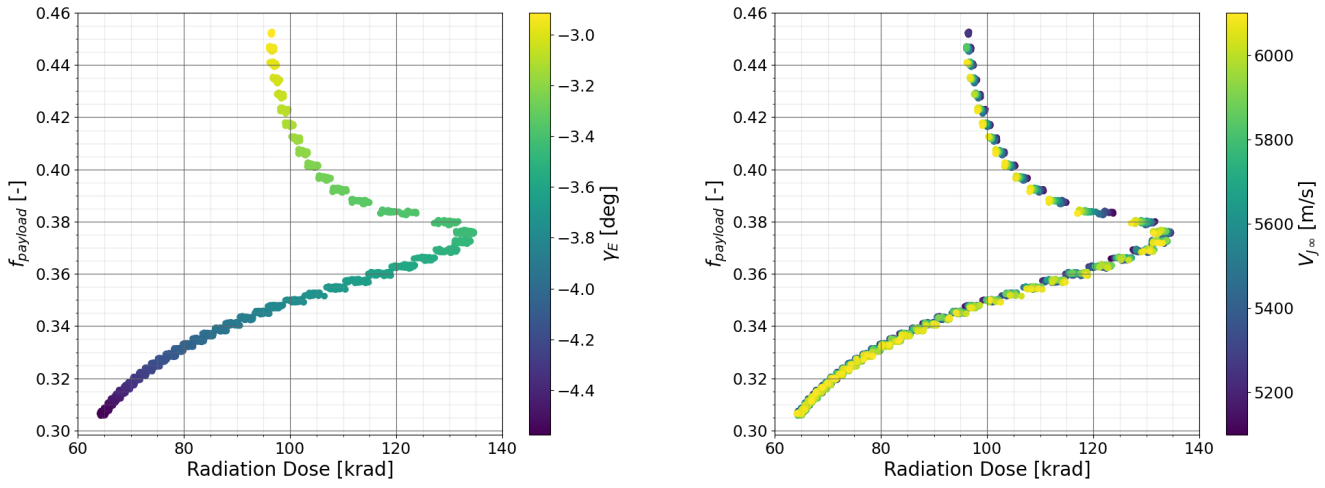

(a) The coloring represents the change in the γ_E decision variable

(b) The coloring represents the change in the V_{J_∞} decision variable

Figure 15.2: The objective *Radiation Dose*, which indicates the total radiation dose absorbed by the spacecraft, is plotted against the objective f_{payload}, that is the payload mass fraction of the aerocapture technique. Results are already filtered for constraints.

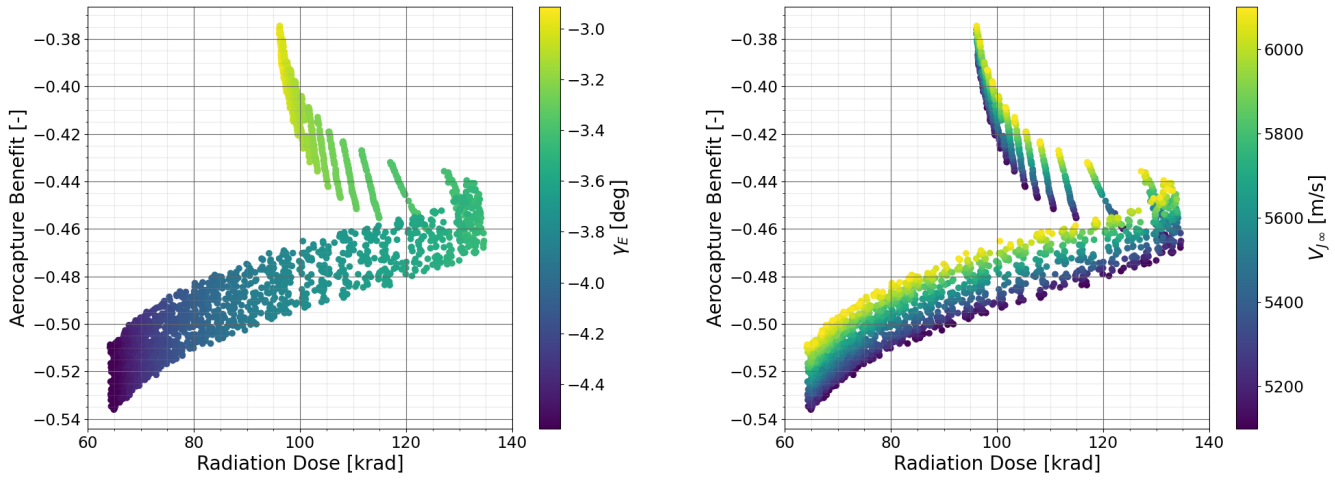

(a) The coloring represents the change in the γ_E decision variable

(b) The coloring represents the change in the V_{J_∞} decision variable

Figure 15.3: The objective *Radiation Dose*, which indicates the total radiation dose absorbed by the spacecraft, is plotted against the objective *Aerocapture Benefit*, which indicates the savings in payload mass fraction w.r.t. a nominal insertion burn. Results are already filtered for constraints.

Lastly, what can be seen from both Figure 15.2 and 15.3 is that the amount of radiation dose a probe absorbs presents two regions of minimum values. The regions featuring steep values of γ_E can rather confidently be considered an area of absolute minimum since low-eccentricity equatorial orbits at Jupiter tend to avoid high-radiation areas (Jupiter's radiation environment is presented in Chapter 3). The lower the eccentricity, the lower the total radiation dose received, with a minimum set for orbits that do not venture further than 1.5 Jupiter radii.

Then, due to the structure of Jupiter's radiation environment, the larger the eccentricity, the more the total radiation dose becomes, peaking at a maximum where the majority of the orbital period is spent in the high-radiation areas (spanning from 1.5 Jupiter radii to Ganymede's orbit). The total radiation dose then is seen to steadily decrease reaching a local minimum where the constraint on maximum final eccentricity acts. Since the interest of the study is on orbits that maximize the *Aerocapture Benefit* objective, and minimize the *Radiation Dose*, the region of minimum radiation dose and minimum aerocapture benefit is considered of little interest for the current project, thus removed from the Pareto front study. As a consequence, the design space on the γ_E decision variable is redefined to contain only values of γ_E greater than -3.4 degrees.

Another final remark can be made, this time on the entry corridor width. The theoretical width presented in Chapter 9 appears to be narrower than that computed with these results. It in fact spans from a γ_E value of -4.5 deg to -2.9 deg, a corridor width of 1.6 degrees. Although more optimistic, it remains a quite narrow entry corridor width for a Jupiter entry, which would still require a robust GNC system to assure the target orbit is properly achieved. As stated by Girija et al. [38], the requirements for a GNC system capable of handling such entry make an aerocapture trajectory at Jupiter a technique unlikely to be used in the near future, since technological advancements are still needed to make sure this approach would be preferable to more classical ones.

15.4. Pareto Front

Based on the results and conclusions of the grid search, a Pareto front has been drawn for the *Radiation Dose* and *Aerocapture Benefit* objectives, with a narrower decision variable space that includes values of γ_E greater than -3.4 degrees. Figure 15.4 shows the location of the points composing the Pareto front of the two objectives, and Figure 15.5 provides a close-up to that same Pareto front.

The optimum points correspond to the runs numbered 7358 and 9857, two candidates whose values for the decision variables, objectives, and constraints can be found in Table 15.1.

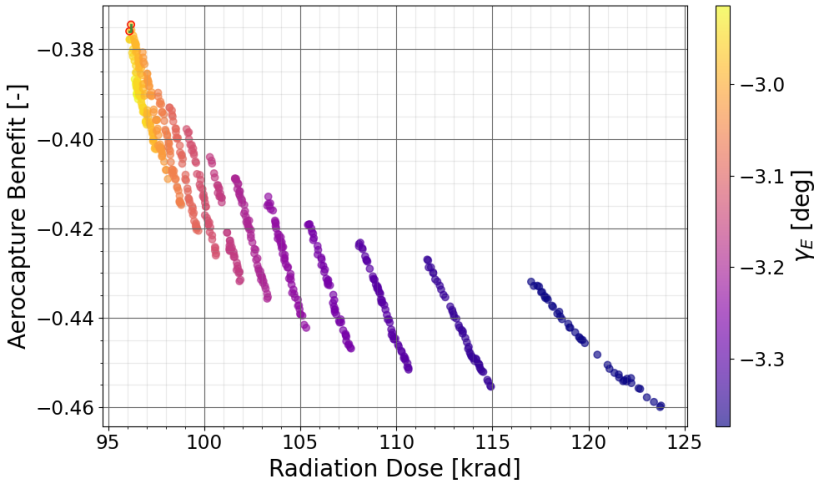

Figure 15.4: The objective *Radiation Dose*, which indicates the total radiation dose absorbed by the spacecraft, is plotted against the objective *Aerocapture Benefit*, which indicates the savings in payload mass fraction w.r.t. a nominal insertion burn. Results are filtered for constraints and values for γ_E are capped at $\gamma_E > -3.4$ deg. The points belonging to the Pareto front are circled in red and are on the top-left corner of the image.

Regarding the two candidate solutions shown in Figure 15.5 and Table 15.1, some remarks can be made.

First, both solutions have the interplanetary excess velocity $V_{J\infty}$ on the higher end of the variable space, with values up to 6 km/s. Since for a classical Hohmann transfer the resulting $V_{J\infty}$ is about 5.6 km/s, it follows that transfer trajectories faster that the Hohmann transfer possess favourable characteristics for the arrival and aerocapture at Jupiter. The favourable effect, however, is not large enough to be considered a driving parameter when designing an Earth-Jupiter transfer, but its presence is still noteworthy, as Figure 15.3b shows.

Both solutions feature a γ_E that is among the shallowest values achievable while also meeting the requirement on final eccentricity. Both their eccentricities in fact show values that are close to the boundary value set to 0.99 (see Table 15.1), thus the neighbourhood of such solutions should be investigated to better assess how close to the boundary those solutions are and their robustness.

Regarding the other constraints, each solution is well within the space of feasible solutions. Regarding the objectives, instead, clear is the end result from the values of the *Aerocapture Benefit* objective. Even for the best solutions, the benefit achievable from aerocapture is negative, meaning that a classical insertion burn by means of a bi-propellant engine still requires less mass for the propellant and tanks than an atmospheric entry subsystem with its heatshield and entry support system.

Another observation can be made about the *Radiation Dose* absorbed by the spacecraft during aerocapture and the first half-orbit. Since aerocapture trajectories that end up in the most favorable airspeed direction during entry are equatorial, this means they have to pass through Jupiter's high radiation areas, which are toroidal regions that peak in intensity along the equator. As a result, the total radiation dose resulting only from the aerocapture and the first orbit is already around values of 96 krad, which can get lower only when considering low-eccentricity captured orbits that stay in the low-radiation vicinity of the planet. On the other hand, classical insertion burns can be performed also in polar orbits, which would totally avoid Jupiter's high radiation areas. This is another key benefit of a classical insertion trajectory.

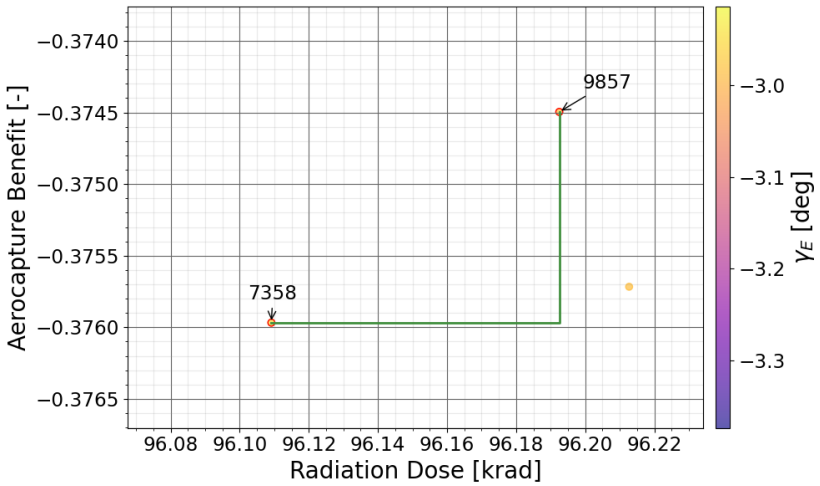

Figure 15.5: Close-up representation of the Pareto front for the objectives *Radiation Dose* and *Aerocapture Benefit*. Annotations on the image indicate the run number associated with the optimum solution and are used for reference.

Values	Solution 7358	Solution 9857
Interplanetary Velocity $V_{J\infty}$ [m/s]	5.837374×10^3	6.089899×10^3
Entry Fpa γ_E [deg]	-2.949495	-2.984848
Payload Mass Fraction f_{payload} [-]	0.4470431	0.4409519
Radiation Dose [krad]	96.10917	96.1925
Aerocapture Benefit [-]	-0.3759677	-0.3744960
Maximum Aerodynamic Load [m/s^2]	6.041796	7.060132
Peak Heat Flux [W/m^2]	5.797463×10^6	6.026576×10^6
Minimum Jupiter Distance [m]	7.021207×10^7	7.020820×10^7
Maximum Jupiter Distance [m]	4.82×10^{10}	4.82×10^{10}
Final Eccentricity [-]	0.9897191	0.9869964

Table 15.1: Values of the decision variables, objectives, and constraints for the optimal solutions numbered 7358 and 9857.

15.5. Best candidates analysis

Refined solutions presented in Figure 15.6 show how there is still some room for improvement, albeit small. It can be seen in Figure 15.6 how solutions closer to the optimum can be found, increasing the *Aerocapture Benefit* by 0.004, however, that means they are also closer to the eccentricity threshold, resulting in risky geometries. A small error for such configurations could result in an escape trajectory with consequent mission failure.

Solution number 9857 presents an eccentricity relatively distant from the constraint (see also Table 15.1), whereas solution number 7358 is already fairly close, to the point it can be considered too risky and unfeasible.

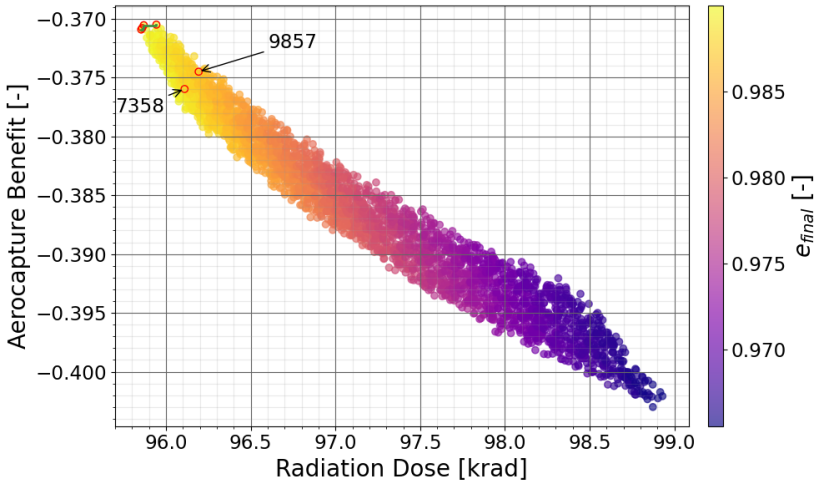

Figure 15.6: The two solutions are now plotted with a color mapping that indicates how close they are to the constraint threshold.

A depiction of the orbital geometry of solution 9857 can be seen in Figure 15.7, whereas its aerocapture altitude-velocity profile is present in Figure 15.8, and other quantities relative to the aerocapture phase are presented in Figure A.5, A.6, A.7.

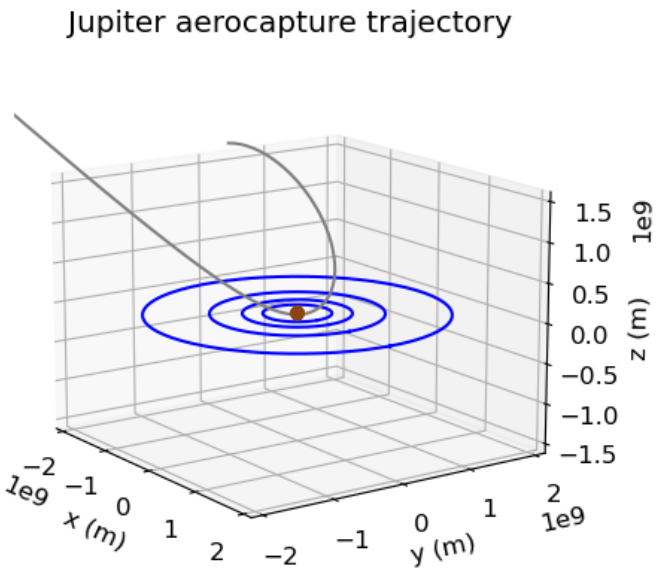

Figure 15.7: Shape of the optimal solution for the aerocapture trajectory.

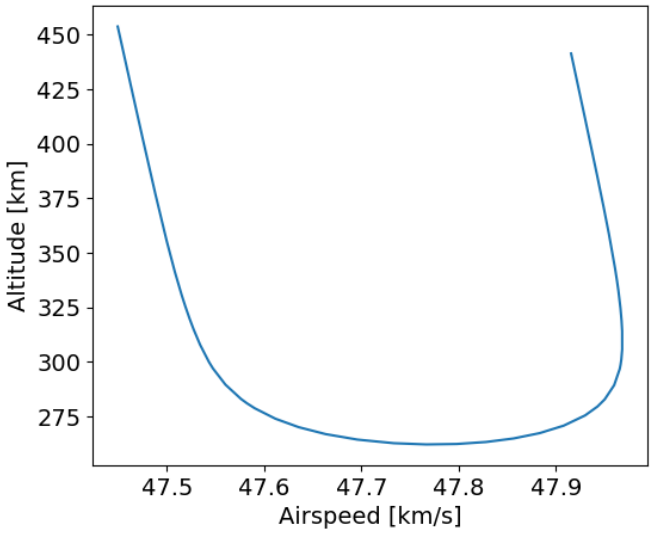

Figure 15.8: Altitude-Velocity profile of the aerocapture phase.

15.6. Observations

A new definition of the problem has been made, which comprehends only aerocapture at Jupiter, with three objectives: f_{payload}, *Aerocapture Benefit*, and *Radiation Dose*.

For the optimization process, f_{payload} has not been used, only *Aerocapture Benefit* and *Radiation Dose*. They have been shown to be the key parameters in comparing the two orbital insertion techniques.

Radiation has an absolute minimum for low Jupiter equatorial orbits, and a local minimum for orbits that spend little time in the high-radiation area. The design space has been limited to γ_E greater than

-3.4 degrees to remove the global minimum of *Radiation Dose*, which is of little interest to the study.

The corridor width remains narrow, 1.6 degrees. A strong and robust GNC system would be needed. For this reason, according to Girija et al. [38], aerocapture at Jupiter isn't preferable to classical methods for the near future.

Aerocapture Benefit is negative even for the best solutions, making this technique a niche application for Jupiter, that could be used only for specific types of missions. The classical orbital insertion maneuver is still to be preferred.

Lastly, radiation doses up to 90 krad are the minimums achievable by the aerocapture technique, whereas a classical Jupiter insertion burn could be performed in a polar orbit, thus totally avoiding Jupiter's high radiation areas and resulting in far lower radiation doses.

16

Aerocapture: Overall Assessment

Aerocapture, the technique of using a planet's atmosphere to decelerate a spacecraft for orbital insertion, has been seen to present both a set of unique challenges and intriguing opportunities.

16.1. Challenges

The first challenge involves mass fractions. Contrary to what might be intuitive, aerocapture requires a greater mass fraction than a traditional propulsive burn. This is primarily due to the need for an aeroshell or heat shield to withstand the high temperatures associated with atmospheric entry. As such, the spacecraft design must incorporate a significant increase in mass, taking into consideration both the protective structure and the associated support systems.

The second challenge pertains to the precision of GNC systems. Aerocapture is a difficult operation that demands exceptionally high precision from these systems. If a spacecraft enters the atmosphere at an incorrect angle or velocity, it could either burn up or bounce back into space. Therefore, ensuring the spacecraft is on the right trajectory and speed is absolutely vital, and demands rigorous and accurate GNC protocols.

The method also imposes constraints on spacecraft design, specifically relating to probe dimensions and folding. To survive the intense heat and pressure during aerocapture, the spacecraft must be designed to withstand these harsh conditions. Additionally, the probe should be designed in a way that allows it to fold effectively to ensure an optimal aerodynamic shape and to safeguard any delicate instruments during this high-stress period.

Lastly, an important operational requirement of aerocapture is performing a pericenter raise maneuver after the initial atmospheric pass. This is necessary to ensure that the spacecraft doesn't reenter the atmosphere, which could potentially lead to a catastrophic mission failure. This maneuver can be accomplished using a thruster, expending a part of the spacecraft's propellant reserve, or via a gravity assist by performing a close flyby of one of the planet's moons. This choice largely depends on the specific mission requirements and the resources available.

16.2. Opportunities

Despite these challenges, aerocapture also provides unique opportunities. One such opportunity is the ability to gather distinctive data about Jupiter's atmosphere. The probe can capture invaluable data about the gas giant's thick atmosphere, providing insights into its composition, temperature, pressure, and more. This is a unique form of data collection that is difficult to achieve with traditional flyby or orbiting missions.

Aerocapture also offers a unique solution for achieving low-eccentricity orbits around Jupiter, a feat difficult with traditional chemical propulsion due to its high propellant requirements. By leveraging Jupiter's own atmosphere to decelerate the spacecraft, aerocapture can efficiently transition the spacecraft into a low-eccentricity orbit. This innovative technique opens new opportunities for close-range, sustained study of Jupiter, enhancing our understanding of its atmospheric composition, magnetosphere, gravitational field, and numerous moons.

16.3. Observations

In conclusion, while aerocapture presents considerable challenges in terms of spacecraft design and operation, it also offers unique data collection opportunities, making it an appealing technique for specific mission profiles. Its applicability for a Jupiter mission remains however still limited to some niche applications.

Part V

Conclusions & Recommendations

17

Conclusions and Recommendations

17.1. Conclusions

The project started with the following research questions:

How can a Jupiter insertion trajectory be performed with the sole use of gravity assists and atmospheric drag?
How, if so, can an unpropelled trajectory to Jupiter deliver more payload than a traditional trajectory featuring impulsive insertion maneuvers?

Answering the first question. Performing a Jupiter insertion trajectory with the sole use of gravity assists and atmospheric drag cannot be done at the current technological level. Further research aimed at improving the knowledge of the spacecraft's position and velocity states is needed. This, or research directed towards combining the magnitude of different forces are some steps towards a reduced need for a GNC system. In fact, currently, a spacecraft needs a GNC system to guide itself to the right atmospheric entry conditions, and to maintain the correct attitude while diving into Jupiter's atmosphere.

Regarding the second question, an unpropelled aerocapture trajectory cannot deliver more spacecraft payload than a conventional insertion burn. This has to do with the mass required for the heatshield and for the entry support system, a suite of instruments necessary to guide the probe through the entry phase. It has only been found in the literature that aerocapture is preferable only for low-eccentricity target orbits, which are not feasible to reach with chemical engines.

In conclusion, while aerocapture presents considerable challenges in terms of spacecraft design and operation, it also offers unique data collection opportunities, making it an appealing technique for specific mission profiles. Its applicability for a Jupiter mission remains however still limited to some niche applications, as the benefit of the aerocapture technique is not positive for all the investigated scenarios.

17.2. Recommendations

Aerocapture, although challenging in terms of spacecraft design and operation, offers a unique data collection opportunity, making it an appealing technique for specific mission profiles. To further enhance the effectiveness and versatility of aerocapture for future missions, the following recommendations are proposed:

1. **GNC:** Given the high precision required for the aerocapture trajectory, there is a need for further research and development of advanced GNC systems. Accuracies in entry position and velocity of respectively 10 km and 0.1 m/s should be satisfied.
2. **Refine Aerocapture Equations:** To improve accuracy and reliability, the mathematical equations that model the aerocapture process should be refined. The actual airspeed, instead of the spacecraft's inertial velocity, and more accurate analytical models for the atmosphere should be considered.

3. **Post-Aerocapture Flyby Targeting Algorithm:** Refinement of the post-aerocapture flyby targeting algorithm is necessary to improve accuracy during mission-critical maneuvers.
4. **Inclination Change Capability:** Feasibility of changing the spacecraft's orbital inclination using aerocapture should be investigated, which could provide a mechanism to avoid hazardous radiation belts in the proposed trajectories.

References

[1] NASA's Cosmos. *Grand tour of Voyager 1 and 2*. 2010. URL: https://ase.tufts.edu/cosmos/view_picture.asp?id=310.

[2] Karel Wakker. *Fundamentals of Astrodynamics*. Jan. 2015. ISBN: 978-94-6186-419-2.

[3] S.J. Saikia et al. "Aerocapture assessment for NASA ice giants pre-decadal survey mission study". In: *Journal of Spacecraft and Rockets* 58.2 (2021), pp. 505–515. DOI: 10.2514/1.A34703. URL: https://www.scopus.com/inward/record.uri?eid=2-s2.0-85102816231&doi=10.2514%2f1.A34703&partnerID=40&md5=84fcc93a8ffc7aa4f03dff08bc14eaaa.

[4] Ashley Morrow. *Hubble Captures Vivid Auroras in Jupiter's Atmosphere*. 2017. URL: https://www.nasa.gov/feature/goddard/2016/hubble-captures-vivid-auroras-in-jupiter-s-atmosphere.

[5] Alvin Seiff et al. "Thermal structure of Jupiter's atmosphere near the edge of a 5-μm hot spot in the north equatorial belt". In: *Journal of Geophysical Research: Planets* 103.E10 (1998), pp. 22857–22889. DOI: https://doi.org/10.1029/98JE01766. eprint: https://agupubs.onlinelibrary.wiley.com/doi/pdf/10.1029/98JE01766. URL: https://agupubs.onlinelibrary.wiley.com/doi/abs/10.1029/98JE01766.

[6] E. Mooij. *Re-Entry Systems*. Delft University of Technology, lecture notes, 2019.

[7] David R. Williams. *Jupiter fact sheet*. 2021. URL: https://nssdc.gsfc.nasa.gov/planetary/factsheet/jupiterfact.html.

[8] M. V. Podzolko et al. "Radiation conditions of a mission to Jupiter and Europa". In: *Solar System Research* 43.2 (Apr. 2009), pp. 116–120. ISSN: 1608-3423. DOI: 10.1134/S0038094609020038. URL: https://doi.org/10.1134/S0038094609020038.

[9] Imke De Pater and Jack J Lissauer. *Planetary sciences*. Cambridge University Press, 2015.

[10] NASA JPL Photojournal. *Jupiter's Gossamer Ring Structure*. 1998. URL: https://photojournal.jpl.nasa.gov/catalog/PIA01623 (visited on 07/19/2022).

[11] Maureen E. Ockert-Bell et al. "The Structure of Jupiter's Ring System as Revealed by the Galileo Imaging Experiment". In: *Icarus* 138.2 (1999), pp. 188–213. ISSN: 0019-1035. DOI: https://doi.org/10.1006/icar.1998.6072. URL: https://www.sciencedirect.com/science/article/pii/S0019103598960729.

[12] Philippe Reynier, Giuliano D'Ammando, and Domenico Bruno. "Review: Modelling chemical kinetics and convective heating in giant planet entries". In: *Progress in Aerospace Sciences* 96 (2018), pp. 1–22. ISSN: 0376-0421. DOI: https://doi.org/10.1016/j.paerosci.2017.11.002. URL: https://www.sciencedirect.com/science/article/pii/S0376042117300507.

[13] Alvin Seiff et al. "Thermal structure of Jupiter's atmosphere near the edge of a 5-μm hot spot in the north equatorial belt". In: *Journal of Geophysical Research* 103.E10 (Sept. 1998), pp. 22857–22890. DOI: 10.1029/98JE01766.

[14] F. S. Milos et al. "Analysis of Galileo Probe Heatshield Ablation and Temperature Data". In: *Journal of Spacecraft and Rockets* 36.3 (1999), pp. 298–306. DOI: 10.2514/2.3465. eprint: https://doi.org/10.2514/2.3465. URL: https://doi.org/10.2514/2.3465.

[15] Michael E Tauber et al. *A Fast Code for Jupiter Atmospheric Entry Analysis*. Tech. rep. 1999. URL: https://ntrs.nasa.gov/api/citations/20040081035/downloads/20040081035.pdf.

[16] S. J. Bolton et al. "The Juno Mission". In: *Space Science Reviews* 213.1 (Nov. 2017), pp. 5–37. ISSN: 1572-9672. DOI: 10.1007/s11214-017-0429-6. URL: https://doi.org/10.1007/s11214-017-0429-6.

[17] Spaceflight101. *Juno's Capture Orbits around Jupiter*. 2016. URL: https://spaceflight101.com/juno/outline-junos-capture-orbits-around-jupiter/ (visited on 04/06/2023).

[18] Nicholas Bradley et al. *Navigation accuracy at Jupiter and Saturn using optical observations of planetary satellites*. Version V1. 2019. DOI: 2014/49249. URL: https://hdl.handle.net/2014/49249.

[19] NASA. *JUNO SPICE KERNELS V1.0*. 2022. DOI: 10.17189/1520117. URL: https://doi.org/10.17189/1520117.

[20] Mohinder Grewal, Lawrence Weill, and Angus Andrews. *Global Positioning Systems, Inertial Navigation, and Integration, Second Edition*. Feb. 2007. ISBN: 0470041900, 978-0470041901. DOI: 10.1002/9780470099728.ch3.

[21] Kevin Cowan Dominic Dirkx. "Numerical astrodynamics". In: *Delft University of Technology* (2021).

[22] Vivek Vittaldev, Erwin Mooij, and Marc Naeije. "Unified State Model theory and application in Astrodynamics". In: *Celestial Mechanics and Dynamical Astronomy* 112 (Mar. 2012). DOI: 10.1007/s10569-011-9396-5.

[23] NASA. *NASA SPICE Kernels*. 2022. URL: https://naif.jpl.nasa.gov/naif/data.html (visited on 06/24/2022).

[24] K. Kumar et al. "Tudat: a modular and robust astrodynamics toolbox". In: *5th ICATT Conference*. ESA. 2012, pp. 1–8.

[25] Greg Kopp and Judith L. Lean. "A new, lower value of total solar irradiance: Evidence and climate significance". In: *Geophysical Research Letters* 38.1 (2011). DOI: https://doi.org/10.1029/2010GL045777. eprint: https://agupubs.onlinelibrary.wiley.com/doi/pdf/10.1029/2010GL045777. URL: https://agupubs.onlinelibrary.wiley.com/doi/abs/10.1029/2010GL045777.

[26] J.L. Hall, M.A. Noca, and R.W. Bailey. "Cost-benefit analysis of the aerocapture mission set". In: *Journal of Spacecraft and Rockets* 42.2 (2005), pp. 309–320. DOI: 10.2514/1.4118. URL: https://www.scopus.com/inward/record.uri?eid=2-s2.0-18144381062&doi=10.2514%5C%2f1.4118&partnerID=40&md5=6f9d5727c4d7b85b839d8ec018e6c0ec.

[27] Norman Ness. "Space Exploration of Planetary Magnetism". In: *Space Science Reviews* 152 (May 2010), pp. 5–22. DOI: 10.1007/s11214-009-9567-9.

[28] H.B. Garrett and A.R. Hoffman. "Comparison of spacecraft charging environments at the Earth, Jupiter, and Saturn". In: *IEEE Transactions on Plasma Science* 28.6 (2000), pp. 2048–2057. DOI: 10.1109/27.902232.

[29] Oliver Montenbruck, Eberhard Gill, and Fh. Lutze. "Satellite orbits: models, methods, and applications". In: *Appl. Mech. Rev.* 55.2 (2002), B27–B28.

[30] Tudat Space. *TUDAT-Space*. 2022. URL: https://docs.tudat.space/en/latest/ (visited on 07/05/2022).

[31] Francesco Biscani and Dario Izzo. "A parallel global multiobjective framework for optimization: pagmo". In: *Journal of Open Source Software* 5.53 (2020), p. 2338. DOI: 10.21105/joss.02338. URL: https://doi.org/10.21105/joss.02338.

[32] Hilber Traum. *Runge–Kutta methods*. 2023. URL: https://en.wikipedia.org/wiki/Runge%5C%E2%5C%80%5C%93Kutta_methods.

[33] Martin Schlueter et al. "GTOPX space mission benchmarks". In: *SoftwareX* 14 (2021), p. 100666. ISSN: 2352-7110. DOI: https://doi.org/10.1016/j.softx.2021.100666. URL: https://www.sciencedirect.com/science/article/pii/S235271102100011X.

[34] MIDACO-SOLVER. *GTOPX - Space Mission Benchmarks*. 2022. URL: http://www.midaco-solver.com/index.php/about/benchmarks/gtopx (visited on 07/05/2022).

[35] NASA. *GALILEO SPICE KERNELS*. 2022. URL: https://naif.jpl.nasa.gov/pub/naif/GLL/kernels/.

[36] Susan K. McMahon. "Overview of the Planetary Data System". In: *Planetary and Space Science* 44.1 (1996). Planetary data system, pp. 3–12. ISSN: 0032-0633. DOI: https://doi.org/10.1016/0032-0633(95)00101-8. URL: https://www.sciencedirect.com/science/article/pii/0032063395001018.

[37] Chul Park. “Stagnation-Region Heating Environment of the Galileo Probe”. In: *Journal of Thermophysics and Heat Transfer* 23.3 (2009), pp. 417–424. DOI: 10.2514/1.38712. eprint: https://doi.org/10.2514/1.38712. URL: https://doi.org/10.2514/1.38712.

[38] Athul Pradeepkumar Girija et al. “Quantitative Assessment of Aerocapture and Applications to Future Solar System Exploration”. In: *Journal of Spacecraft and Rockets* 59.4 (2022), pp. 1074–1095. DOI: 10.2514/1.A35214. eprint: https://doi.org/10.2514/1.A35214. URL: https://doi.org/10.2514/1.A35214.

[39] Athul Pradeepkumar Girija, Ye Lu, and Sarag J. Saikia. “Feasibility and Mass-Benefit Analysis of Aerocapture for Missions to Venus”. In: *Journal of Spacecraft and Rockets* 57.1 (2020), pp. 58–73. DOI: 10.2514/1.A34529. eprint: https://doi.org/10.2514/1.A34529. URL: https://doi.org/10.2514/1.A34529.

[40] E. Venkatapathy et al. “Entry System Technology Readiness for Ice-Giant Probe Missions”. In: *Space Science Reviews* 216.2 (2020). cited By 9. DOI: 10.1007/s11214-020-0638-2. URL: https://www.scopus.com/inward/record.uri?eid=2-s2.0-85079378659&doi=10.1007%2fs11214-020-0638-2&partnerID=40&md5=e035f034dd7e2f88eb182dc966bf1fcd.

[41] Brent Buffington. “Trajectory Design Concept for the Proposed Europa Clipper Mission (Invited)”. In: *AIAA/AAS Astrodynamics Specialist Conference*. DOI: 10.2514/6.2014-4105. eprint: https://arc.aiaa.org/doi/pdf/10.2514/6.2014-4105. URL: https://arc.aiaa.org/doi/abs/10.2514/6.2014-4105.

[42] Diane Vaughan et al. “A comparative study of aerocapture missions with a Mars destination”. In: *41st AIAA/ASME/SAE/ASEE Joint Propulsion Conference & Exhibit*. 2005, p. 4110.

[43] Makoto Matsumoto and Takuji Nishimura. “Mersenne Twister: A 623-Dimensionally Equidistributed Uniform Pseudo-Random Number Generator”. In: *ACM Trans. Model. Comput. Simul.* 8.1 (Jan. 1998), pp. 3–30. ISSN: 1049-3301. DOI: 10.1145/272991.272995. URL: https://doi.org/10.1145/272991.272995.

[44] Kenneth Sutton and Randolph A Graves Jr. *A general stagnation-point convective heating equation for arbitrary gas mixtures*. Tech. rep. 1971.

[45] E. Zoby et al. “An approximate inviscid radiating flow field analysis for outer planet entry probes”. In: *16th Aerospace Sciences Meeting*. DOI: 10.2514/6.1978-189. eprint: https://arc.aiaa.org/doi/pdf/10.2514/6.1978-189. URL: https://arc.aiaa.org/doi/abs/10.2514/6.1978-189.

[46] J Moss and A Simmonds. “Galileo probe forebody flowfield predictions during Jupiter entry”. In: *3rd joint thermophysics, fluids, plasma and heat transfer conference*. 1982, p. 874.

[47] Simmonds A. L. Moss J. N. Jones J. J. “Radiative Flux Penetration through a Blown Shock Layer for Jupiter Entry Conditions”. In: *Outer Planet Entry Heating and Thermal Protection*, pp. 22–41. DOI: 10.2514/5.9781600865381.0022.0041. eprint: https://arc.aiaa.org/doi/pdf/10.2514/5.9781600865381.0022.0041. URL: https://arc.aiaa.org/doi/abs/10.2514/5.9781600865381.0022.0041.

[48] J. Moss and JR. C. Bolz. “Aerothermal environment for Jovian entry probes”. In: *11th Thermophysics Conference*. DOI: 10.2514/6.1976-469. eprint: https://arc.aiaa.org/doi/pdf/10.2514/6.1976-469. URL: https://arc.aiaa.org/doi/abs/10.2514/6.1976-469.

[49] B.L. Haas and F.S. Milos. “Simulated rarefied entry of the Galileo probe into the Jovian atmosphere”. In: *Journal of Spacecraft and Rockets* 32.3 (1995). cited By 10, pp. 398–403. DOI: 10.2514/3.26628. URL: https://www.scopus.com/inward/record.uri?eid=2-s2.0-0029310284&doi=10.2514%2f3.26628&partnerID=40&md5=fc47e9bc7c7cbaecaa218b6e2f7f2397.

[50] Shingo Matsuyama et al. “Numerical Simulation of Galileo Probe Entry Flowfield with Radiation”. In: *8th AIAA/ASME Joint Thermophysics and Heat Transfer Conference*. DOI: 10.2514/6.2002-2994. eprint: https://arc.aiaa.org/doi/pdf/10.2514/6.2002-2994. URL: https://arc.aiaa.org/doi/abs/10.2514/6.2002-2994.

[51] Shingo Matsuyama et al. “Numerical simulation of Galileo probe entry flowfield with radiation and ablation”. In: *Journal of Thermophysics and Heat Transfer* 19.1 (2005), pp. 28–35.

[52] L. Santos Fernandes, B. Lopez, and M. Lino Da Silva. “Computational fluid radiative dynamics of the Galileo Jupiter entry”. In: *Physics of Fluids* 31.10 (2019). cited By 6. DOI: 10.1063/1.5115264. URL: https://www.scopus.com/inward/record.uri?eid=2-s2.0-85073600228&doi=10.1063%2f1.5115264&partnerID=40&md5=ea3a71151ba81621da40ae8b787a814b.

[53] Alvin Seiff et al. “Galileo probe aerodynamics”. In: *14th Applied Aerodynamics Conference*. DOI: 10.2514/6.1996-2451. eprint: https://arc.aiaa.org/doi/pdf/10.2514/6.1996-2451. URL: https://arc.aiaa.org/doi/abs/10.2514/6.1996-2451.

[54] M. E. Tauber and K. Sutton. “Stagnation-point radiative heating relations for earth and Mars entries”. In: *Journal of Spacecraft and Rockets* 28.1 (1991), pp. 40–42. DOI: 10.2514/3.26206. eprint: https://doi.org/10.2514/3.26206. URL: https://doi.org/10.2514/3.26206.

[55] Michael Wright and John Dec. *Aerothermodynamic and Thermal Protection System Aspects of Entry System Design Course*. 2012. URL: https://tfaws.nasa.gov/TFAWS12/Proceedings/Aerothermodynamics%20Course.pdf (visited on 02/14/2023).

[56] Heiko Ritter et al. “Jupiter Entry Probe Feasibility Study from the ESTEC CDF Team: Heat Flux Evaluation & TPS Definition”. In: *Thermal Protection Systems and Hot Structures*. Vol. 631. 2006.

[57] Chul Park and Michael Tauber. “Heatshielding problems of planetary entry - A review”. In: *30th Fluid Dynamics Conference*. DOI: 10.2514/6.1999-3415. eprint: https://arc.aiaa.org/doi/pdf/10.2514/6.1999-3415. URL: https://arc.aiaa.org/doi/abs/10.2514/6.1999-3415.

[58] Philippe Reynier. “Survey of convective blockage for planetary entries”. In: *Acta Astronautica* 83 (2013), pp. 175–195. ISSN: 0094-5765. DOI: https://doi.org/10.1016/j.actaastro.2012.06.016. URL: https://www.sciencedirect.com/science/article/pii/S0094576512002548.

[59] Michael E. Tauber and Roy M. Wakefield. “Heating Environment and Protection during Jupiter Entry”. In: *Journal of Spacecraft and Rockets* 8.6 (1971), pp. 630–636. DOI: 10.2514/3.59703. eprint: https://doi.org/10.2514/3.59703. URL: https://doi.org/10.2514/3.59703.

[60] Shigeru Aso et al. “Preliminary studies on the planetary entry to Jupiter by aerocapture technique”. In: *Acta Astronautica* 59.8 (2006). Selected Proceedings of the Fifth IAA International Conference on Low Cost Planetary Missions, pp. 651–660. ISSN: 0094-5765. DOI: https://doi.org/10.1016/j.actaastro.2005.07.034. URL: https://www.sciencedirect.com/science/article/pii/S0094576505002171.

[61] R.A. Brewer and D. N. Brant. “Thermal Protection System for the Galileo Mission Atmospheric Entry Probe”. In: *Aerothermodynamics and Planetary Entry*. 1980, pp. 309–334. DOI: 10.2514/5.9781600865510.0309.0334. eprint: https://arc.aiaa.org/doi/pdf/10.2514/5.9781600865510.0309.0334. URL: https://arc.aiaa.org/doi/abs/10.2514/5.9781600865510.0309.0334.

[62] A. Balakrishnan and W. Nicolet. “Galileo probe forebody thermal protection - Benchmark heating environment calculations”. In: *16th Thermophysics Conference*. DOI: 10.2514/6.1981-1072. eprint: https://arc.aiaa.org/doi/pdf/10.2514/6.1981-1072. URL: https://arc.aiaa.org/doi/abs/10.2514/6.1981-1072.

[63] Michael Wright et al. “Defining Ablative Thermal Protection System Margins for Planetary Entry Vehicles”. In: June 2011. ISBN: 978-1-62410-146-5. DOI: 10.2514/6.2011-3757.

[64] Jorrik Engelsma and Erwin Mooij. “Aerocapture Mission Analysis”. In: *TU Delft Repository* (Mar. 2019). DOI: http://resolver.tudelft.nl/uuid:aea0c8ab-d43a-4988-bee6-d7cb3fbf37e0.

[65] Dario Izzo. “Revisiting Lambert’s Problem”. In: *Celestial Mechanics and Dynamical Astronomy* (Mar. 2014). DOI: 10.1007/s10569-014-9587-y.

[66] Nitin Arora et al. “Partial Derivatives of the Solution to the Lambert Boundary Value Problem”. In: *Journal of Guidance, Control, and Dynamics* 38.9 (2015), pp. 1563–1572. DOI: 10.2514/1.G001030. eprint: https://doi.org/10.2514/1.G001030. URL: https://doi.org/10.2514/1.G001030.

A

Figures

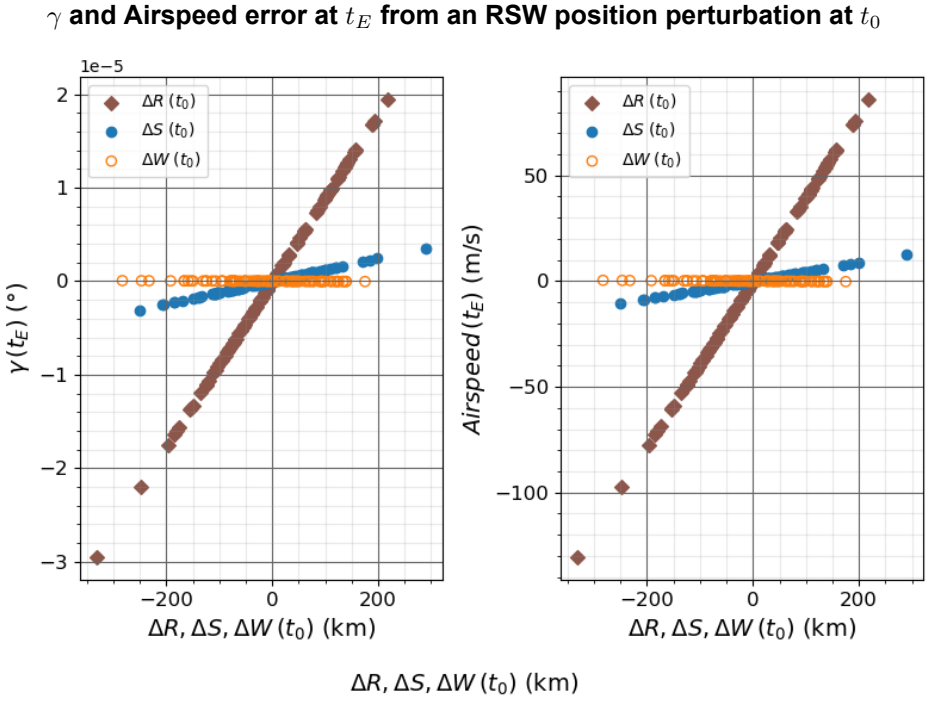

Figure A.1: Error introduced on the entry Flight Path Angle (γ) and Airspeed by an RSW perturbation of the initial position at the beginning of the trajectory. The perturbations are independently introduced on each RSW axis, thus their effect shown here is uncoupled.

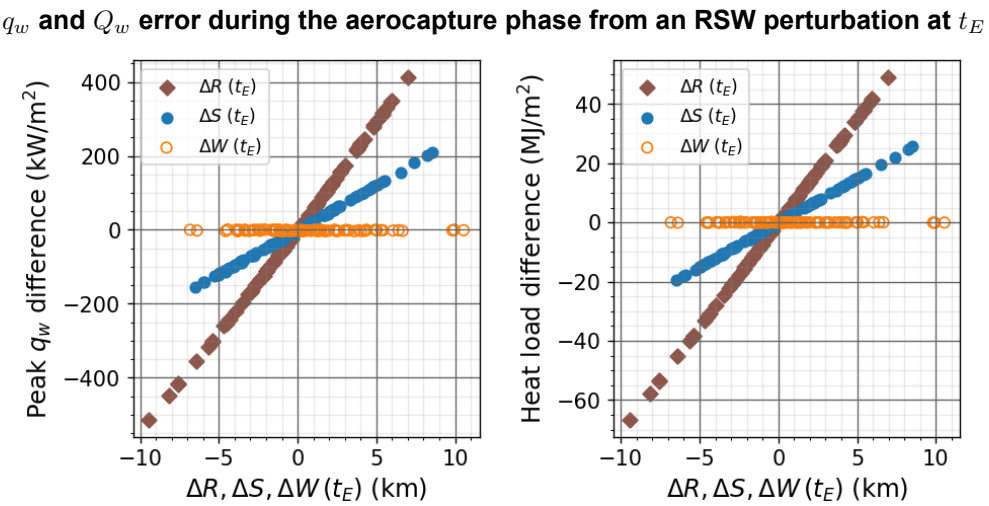

Figure A.2: Peak heat flux (q_w) and total heat load (Q_w) error from a position perturbation on the R, S, or W axis at atmospheric entry (t_E). The perturbations on each axis are uncoupled.

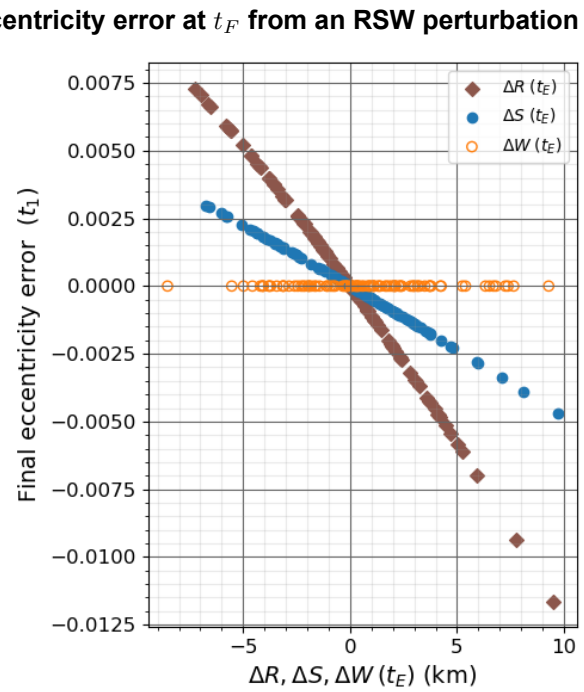

Figure A.3: Variation in the eccentricity of the final orbit (t_1) for a position perturbation in the R, S, or W axes at atmospheric entry (t_E). The perturbations have been individually assessed for each axis, thus their effect shown here is not coupled.

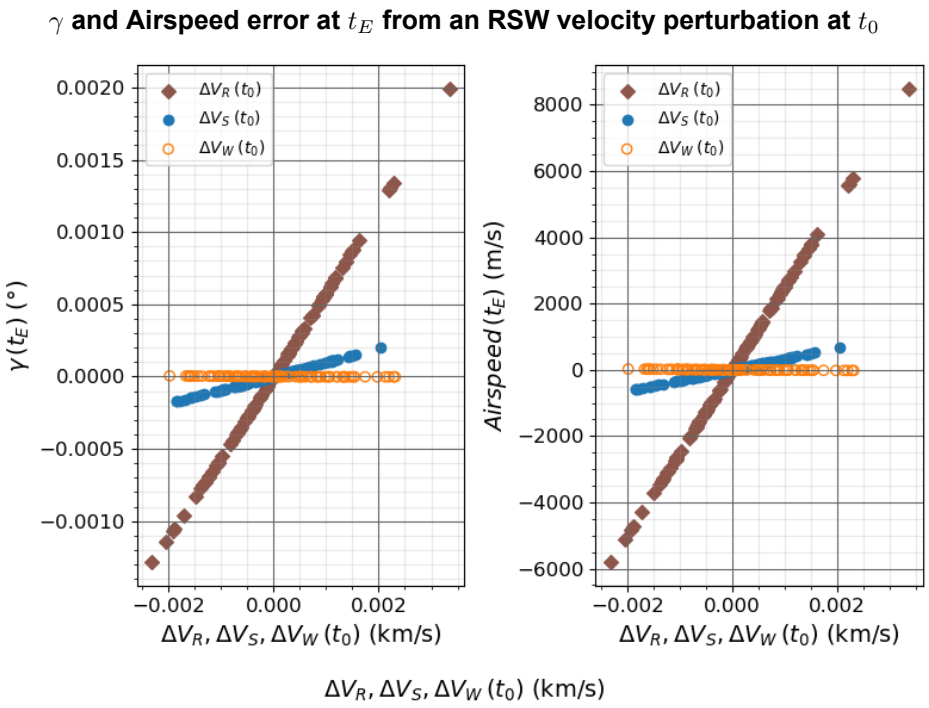

Figure A.4: Error introduced on the entry Flight Path Angle (γ) and Airspeed by an RSW perturbation of the initial position at the beginning of the trajectory. The perturbations are independently introduced on each RSW axis, thus their effect shown here is uncoupled.

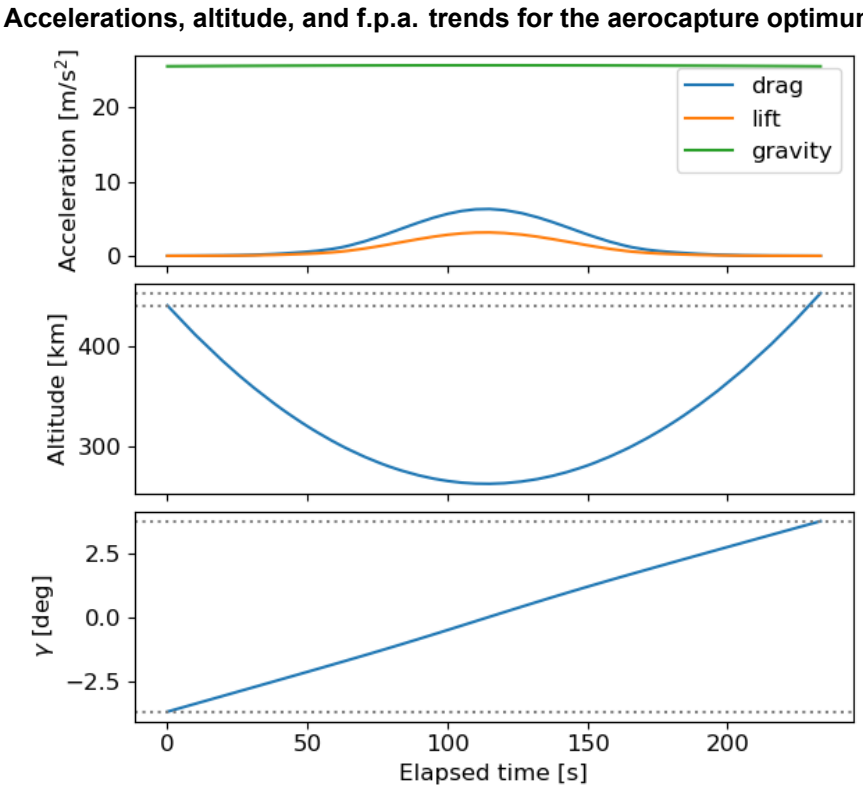

Figure A.5: Aerodynamic and gravitational forces, altitude profile, and γ profile are shown for the aerocapture phase.

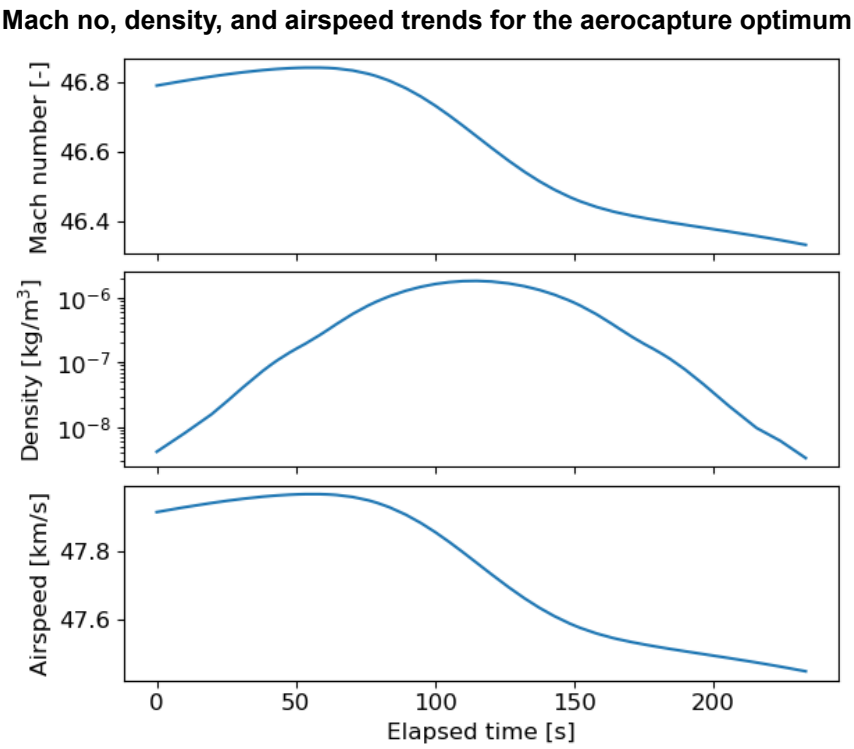

Figure A.6: Mach number, atmospheric density, and airspeed profiles are shown for the aerocapture phase.

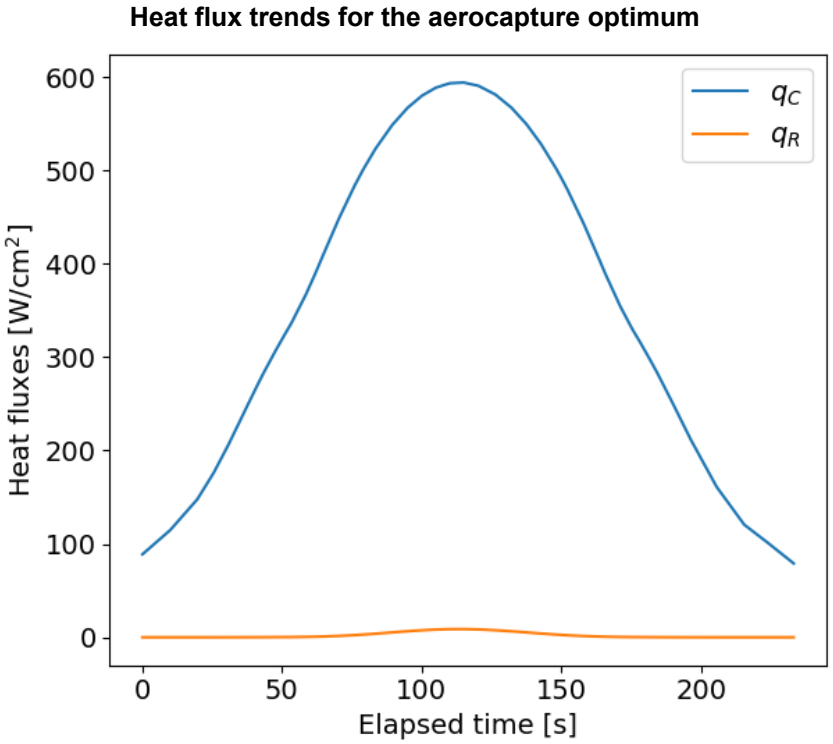

Figure A.7: Convective (q_C) and radiative (q_R) heat fluxes are shown for the aerocapture phase.

B

Tabulated Data

z, km	p, mbar	T, K	ρ, kg/m^3	μ, amu	R, J/ (kg K)	g, m/s^2	c$_p$/c$_v$
1029.2	9.633e-07	899.9	2.575e-11	1.999	4159.0	22.526	1.400
1020.0	1.018e-06	903.4	2.711e-11	2.000	4157.8	22.533	1.400
1000.0	1.148e-06	897.0	3.082e-11	2.001	4155.4	22.547	1.400
980.0	1.297e-06	883.9	3.535e-11	2.002	4152.9	22.562	1.400
960.0	1.468e-06	872.2	4.057e-11	2.003	4150.5	22.576	1.400
940.0	1.664e-06	866.0	4.635e-11	2.004	4148.1	22.590	1.400
920.0	1.888e-06	865.4	5.264e-11	2.006	4145.6	22.605	1.400
900.0	2.141e-06	869.1	5.948e-11	2.007	4143.2	22.619	1.400
880.0	2.427e-06	875.2	6.700e-11	2.008	4140.9	22.633	1.400
860.0	2.749e-06	881.4	7.539e-11	2.009	4138.5	22.648	1.400
840.0	3.112e-06	885.2	8.502e-11	2.010	4136.2	22.662	1.400
820.0	3.522e-06	884.4	9.638e-11	2.011	4133.9	22.677	1.400
800.0	3.990e-06	877.2	1.101e-10	2.012	4131.6	22.691	1.400
780.0	4.527e-06	862.2	1.272e-10	2.014	4128.5	22.706	1.401
760.0	5.152e-06	840.0	1.487e-10	2.015	4125.5	22.720	1.401
740.0	5.887e-06	812.0	1.759e-10	2.017	4122.4	22.735	1.401
720.0	6.765e-06	776.1	2.117e-10	2.018	4119.3	22.749	1.401
700.0	7.827e-06	741.0	2.567e-10	2.020	4116.2	22.763	1.401
680.0	9.117e-06	712.8	3.113e-10	2.023	4110.6	22.778	1.401
660.0	1.068e-05	692.7	3.757e-10	2.026	4104.8	22,792	1.401
640.0	1.256e-05	680.2	4.506e-10	2.028	4099.1	22.807	1.402
620.0	1.481e-05	674.6	5.364e-10	2.031	4093.4	22.822	1.402
600.0	1.749e-05	669.8	6.390e-10	2.034	4087.6	22.836	1.402
580.0	2.067e-05	670.3	7.562e-10	2.039	4078.2	22.851	1.402
560.0	2.445e-05	664.0	9.053e-10	2.043	4068.8	22.865	1.403
540.0	2.903e-05	642.4	1.114e-09	2.049	4056.9	22.880	1.404
520.0	3.484e-05	594.3	1.451e-09	2.057	4042.2	22.894	1.404
500.0	4.256e-05	545.9	1.937e-09	2.064	4027.4	22.909	1.405
480.0	5.265e-05	535.8	2.455e-09	2.077	4003.9	22.924	1.406
460.0	6.518e-05	535.7	3.058e-09	2.089	3980.4	22.938	1.408
440.0	8.149e-05	483.1	4.276e-09	2,107	3946.1	22.953	1.411
420.0	0.0001072	392.9	6.989e-09	2.129	3904.6	22.968	1.413
400.0	0.0001463	370.2	1.023e-08	2.152	3863.2	22.982	1.414
380.0	0.0002107	289.2	1.917e-08	2.187	3802.5	22.997	1.429
360.0	0.0003367	231.7	3.892e-08	2.224	3738.7	23.012	1.445
340.0	0.0006036	198.6	8.251e-08	2,257	3684.5	23.026	1.461
320.0	0.001152	194.2	1.629e-07	2,281	3645.4	23.041	1.472
300.0	0.002177	177.6	3.417e-07	2,296	3621.3	23.056	1.483
280.0	0.004800	152.8	8.713e-07	2.303	3610.5	23.070	1.488
260.0	0.01094	151.0	2.012e-06	2.306	3604.8	23.085	1.489
240.0	0.02475	155.7	4.416e-06	2.308	3602.5	23.100	1.489
220.0	0.05593	157.2	9.878e-06	2.309	3601.6	23.115	1.490
200.0	0.1257	158.2	2.206e-05	2.309	3600.7	23.130	1.490
180.0	0.2824	157.4	4.984e-05	2.309	3600.6	23.144	1.490
160.0	0.6192	168.6	0.0001020	2.309	3600.6	23.159	1.490
140.0	1.342	160.5	0.0002325	2.309	3600.5	23.174	1.491
120.0	3.079	149.8	0.0005710	2.309	3600.4	23.189	1.491
100.0	7.177	158.1	0.001261	2.309	3600.4	23.204	1.493
80.0	16.40	143.8	0.003168	2.309	3600.4	23.218	1.511
60.0	43.74	122.6	0.009915	2.309	3600.4	23.233	1.534
40.0	135.8	113.2	0.03335	2.309	3600.4	23.248	1.547
23.3	351.5	122.9	0.07945	2.309	3600.4	23.261	1.528

Table B.1: Jupiter's upper atmospheric state properties [5, Table 8].

t, s	z, km	V, km/s	γ, deg	m, kg	d, m	M	Re	Kn	C_D
-240.0	1027.1	47.130	-10.61	338.93	1.265	20.58	0.0692	443.	2.060
-235.0	983.96	47.151	-10.46	338.93	1.265	20.77	0.0924	335.	2.060
-230.0	941.44	47.171	-10.31	338.93	1.265	21.03	0.125	250.	2.060
-225.0	899.49	47.191	-10.16	338.93	1.265	21.02	0.163	192.	2.060
-220.0	858.13	47.211	-10.02	338.93	1.265	20.89	0.206	151.	2.060
-215.0	817.36	47.230	-9.87	338.93	1.265	20.88	0.265	118.	2.060
-210.0	777.17	47.249	-9.72	338.93	1.265	21.19	0.358	88.3	2.058
-205.0	737.57	47.268	-9.57	338.93	1.265	21.87	0.515	63.2	2.054
-200.0	698.56	47.287	-9.42	338.93	1.265	22.90	0.793	43.0	2.051
-195.0	660.15	47.305	-9.27	338.93	1.265	23.69	1.19	29.6	2.047
-190.0	622.32	47.323	-9.12	338.93	1.265	24.04	1.70	21.1	2.045
-185.0	585.09	47.341	-8.97	338.93	1.265	24.17	2.35	15.3	2.043
-180.0	548.45	47.358	-8.82	338.93	1.265	24.51	3.35	10.9	2.040
-175.0	512.41	47.376	-8.68	338.93	1.265	26.27	5.81	6.74	2.026
-170.0	476.96	47.393	-8.53	338.93	1.265	27.27	9.43	4.31	2.010
-165.0	442.11	47.409	-8.38	338.93	1.265	28.48	15.90	2.67	1.991
-160.0	407.87	47.425	-8.23	338.93	1.265	32.93	40.70	1.21	1.953
-155.0	374.22	47.441	-8.08	338.93	1.265	38.89	1.30e+02	0.446	1.875
-150.0	341.18	47.455	-7.93	338.93	1.265	45.77	5.46e+02	0.125	1.726
-145.0	308.74	47.466	-7.78	338.93	1.265	45.07	1.47e+03	0.0453	1.526
-140.0	276.91	47.468	-7.63	338.93	1.265	51.81	7.85e+03	0.00981	1.153
-135.0	245.70	47.437	-7.48	338.93	1.265	51.33	2.76e+04	0.00278	1.087
-130.0	215.15	47.300	-7.33	338.87	1.265	51.26	9.60e+04	0.000798	1.049
-125.0	185.39	46.822	-7.18	338.51	1.265	50.78	3.17e+05	0.000238	1.030
-120.0	156.76	45.377	-7.04	336.39	1.264	47.68	8.55e+05	8.31e-05	1.026
-115.0	130.16	41.495	-6.92	324.53	1.261	45.00	2.55e+06	2.65e-05	1.019
-110.0	107.67	32.770	-6.85	287.72	1.246	36.10	5.43e+06	9.98e-06	1.009
-105.0	91.391	21.965	-6.89	254.15	1.223	23.69	6.62e+06	5.33e-06	1.004
-100.0	80.749	13.669	-7.10	244.19	1.213	15.33	7.45e+06	3.07e-06	1.001
-95.0	73.873	8.444	-7.58	242.09	1.211	9.91	7.53e+06	1.96e-06	1.010
-90.0	69.146	5.535	-8.43	241.39	1.210	6.49	6.20e+06	1.56e-06	1.033
-85.0	65.533	3.828	-9.75	241.34	1.210	4.60	5.64e+06	1.22e-06	1.066
-80.0	62.535	2.767	-11.67	241.33	1.209	3.31	4.59e+06	1.08e-06	1.146
-75.0	59.878	2.051	-14.30	241.33	1.207	2.50	4.07e+06	9.12e-07	1.254
-70.0	57.438	1.543	-17.80	241.33	1.207	1.93	3.92e+06	7.35e-07	1.345
-65.0	55.135	1.188	-22.35	241.33	1.207	1.50	3.58e+06	6.25e-07	1.384
-60.0	52.892	0.956	-27.93	241.33	1.207	1.20	3.17e+06	5.63e-07	1.378
-55.0	50.635	0.808	-34.35	241.33	1.207	1.01	3.05e+06	4.94e-07	1.306
-50.0	48.323	0.712	-41.21	241.33	1.207	0.90	3.11e+06	4.30e-07	1.000
-45.0	45.909	0.670	-47.99	241.33	1.207	0.85	3.39e+06	3.72e-07	0.926
-40.0	43.356	0.642	-54.26	241.33	1.207	0.82	3.88e+06	3.14e-07	0.897
-35.0	40.714	0.617	-59.90	241.33	1.207	0.78	4.25e+06	2.74e-07	0.872
-30.0	38.037	0.591	-64.90	241.33	1.207	0.74	4.58e+06	2.41e-07	0.846
-25.0	35.377	0.563	-69.28	241.33	1.207	0.73	5.68e+06	1.91e-07	0.819
-20.0	32.784	0.534	-73.09	241.33	1.207	0.67	5.81e+06	1.73e-07	0.796
-15.0	30.272	0.507	-76.35	241.33	1.207	0.65	6.60e+06	1.46e-07	0.776
-10.0	27.863	0.479	-79.12	241.33	1.207	0.60	6.83e+06	1.32e-07	0.761
-5.0	25.558	0.457	-81.42	241.33	1.207	0.56	6.68e+06	1.25e-07	0.749
0.0	23.339	0.438	-83.29	241.33	1.207	0.53	6.90e+06	1.15e-07	0.739

Table B.2: Galileo's entry trajectory [5, Table 6].

C

Thesis work planning

The detailed work planning for the thesis is shown in Table C.1. Each task has been labeled with an alphabetical letter, according to the legend shown in Table C.2, and there the corresponding calendar weeks are also pointed for better readability.

Sep 2022	**W1 D 5-11**	**W2 D 12-18**	**W3 D 19-25**	**W4 D 26-30**
	/	A(5)	A(2), B(3)	C(2), bns(3)
Oct 2022	**W5 D 1-9**	**W6 D 10-16**	**W7 D 17-23**	**W8 D 24-30**
	D(5)	D(5)	D(5)	E(5)
Nov 2022	**W9 D 1-7**	**W10 D 8-14**	**W11 D 15-21**	**W12 D 22-30**
	F(3), bns(2)	F(2), bns(3)	F(5)	G(5)
Dec 2022	**W13 D 1-7**	**W14 D 8-14**	**W15 D 15-21**	**W16 D 22-31**
	H(4), bns(1)	bns(5)	bns(5)	/
Jan 2023	**W17 D 1-8**	**W18 D 9-15**	**W19 D 16-22**	**W20 D 23-31**
	/	I(5)	I(5)	J(5)
Feb 2023	**W21 D 1-7**	**W22 D 8-14**	**W23 D 15-21**	**W24 D 22-28**
	J(5)	K(5)	K(5)	K(5)
Mar 2023	**W25 D 1-7**	**W26 D 8-14**	**W27 D 15-21**	**W28 D 22-31**
	K(5)	L(5)	M(3), bns(2)	N(5)
Apr 2023	**W29 D 1-7**	**W30 D 8-14**	**W31 D 15-21**	**W32 D 22-30**
	O(5)	P(5)	Q(4), bns(1)	/

Table C.1: Weekly work planning for the Thesis. Each letter here represents a task that is part of the Thesis, and the legend is shown at Table C.2. The numbers in brackets beside each letter are the number of days that will be spent on that task. 'bns' stands for Bonus, as there is a total of 22 planned bonus days. 'W' and 'D' stand for Week and Days.

Task Letter	Task	Days required	Dates 2022-23
A	Organize the Python workspace, import the TUDAT and PyGMO libraries, define the problem requirements, create a raw physical model	7	Sep W2-3
B	Find good benchmark trajectories to use for refining the physical model, find a shape and aerodynamic properties for the spacecraft	3	Sep W3
C	Tune the parameters of the integrator	2	Sep W4
D	Code spherical harmonics magnetic field, lorentz force, jupiter radiation areas	15	Oct W1-3
E	Refine the physical model to make it comply with the requirements	5	Oct W4
F	Validate the Physical model with the Juno and Galileo mission data	10	Nov W1-3
G	Set up the optimization problem: define the objective functions, the constraints	5	Nov W4
H	Choose pygmo optimizer with MINLP solving capabilities	4	Dec W1
I	Set up the optimization algorithm and tune it	10	Jan W2-3
J	Verify optimizer with GTOX problems	10	Jan W4 Feb W1
K	Run optimization algorithm, adjust parameters if necessary	20	Feb W2-4 Mar W1
L	Perform local refinement of pareto front	5	Mar W2
M	Plot and analyze best candidates	3	Mar W3
N	Analyze sensitivity to initial conditions of such candidates	5	Mar W3-4
O	Compare best solutions to analogue trajectories performed with impulsive maneuvers at Jupiter insertion	5	Apr W1
P	If aerocapture is worse, try aerocapture with no previous flybys; if aerocapture is better, do sensitivity analysis of physical model	5	Apr W2
Q	Draw conclusions, review the work, write introduction and abstract	4	Apr W3
Addition	Add some other parameters to be varied in the trajectory (e.g. simulate attitude change maneuver by guidance) to allow for a more flexible optimization		
	Bonus Days:	22	
	Total:	**140**	

Table C.2: Legend of the tasks that need to be done for the thesis. The number of days per task, as well as the total number of days, have been reported. Moreover, a small addition to the study has been mentioned as well. Such addition can be done if there is enough spare time at the end of the study.